Design optimisation of 3D woven reinforcements with geometric features

Shibo Yan

Thesis submitted to The University of Nottingham for the degree of Doctor of Philosophy

March 2017

Abstract

3D weaving technology enables the manufacturing of advanced near net-shape profiles, through incorporating geometric features such as bifurcations, and varying cross-sections into the preform, for use as reinforcements in composite materials. Their design space is very large due to a wide range of weave patterns in their 3D fibre architectures, and currently the lack of analysis techniques that relate weave architectures with the resulting processing and structural performance restricts the application of such advanced 3D woven composites.

In this thesis, the effect of fibre architecture on mechanical properties was shown to be significant for 3D woven composite T-joints, which further illustrates the challenges for designing an optimum 3D woven reinforcement. This work is an attempt to develop modelling techniques that are able to accurately predict the resulting structural performance for composites based on 3D woven architectures.

Geometric models were developed to account for the deformation in the fibre architecture caused by the bifurcation process in manufacturing of 3D near net-shape T-joint preforms, in order to improve the accuracy of the reinforcement geometry in finite element models. A methodology based on voxels was proposed to overcome the current meshing problems whilst allowing delamination modelling for composites with complex fibre architecture.

Consequently, a meso-scale modelling framework for predicting weave architectures of 3D woven composite T-joints and the resulting mechanical behaviour under quasi-static pull-off loading was proposed, in which damage modelling incorporates both interface and constituent material damage, in

conjunction with a continuum damage mechanics approach to account for the progressive failure behaviour. Results were shown to agree well with experimental data beyond initial failure.

Based on the proposed predictive modelling method, the effect of fibre architecture, in which the design space was simplified by three design variables, i.e. weft yarn path straightness, weft yarn path entanglement and weft yarn path cross-over, on mechanical performance was investigated. Varying yarn path cross-over was found to improve both stiffness and failure load. Increasing the proportion of yarn path entanglement also improved the damage resistance capability, but a high level of yarn path entanglement caused a reduction in yarn path straightness and therefore the structural stiffness would be compromised. Based on the above findings, a design optimisation philosophy for 3D woven T-joint reinforcements under tensile pull-off loading was proposed.

Acknowledgements

I would like to thank my academic supervisors, Professor Andrew Long and Dr Xuesen Zeng for their excellent support and continuing encouragement during the course of this work. It has been an unforgettable experience for me to study in Nottingham.

I would like to thank my friends and colleagues in the Composites Research Group at the University of Nottingham, for their friendship, support, and knowledge. Support from the technical staff in specimen moulding and mechanical testing is greatly appreciated.

Thanks go to The EPSRC Centre for Innovative Manufacturing in Composites (CIMComp) for sponsoring these academic and social events which I thoroughly enjoyed.

Most importantly, I would like to my family for their unconditional love and support during my studies.

Glossary

Areal density	The weight of fibre per unit area of fabric
Crimp	The waviness of a fibre or yarn
Cohesive zone model (CZM)	A modelling method for delamination/crack growth
Digital image correlation (DIC)	An optical method for measurements of changes in images
MacAulay operator	A notation used to describe a ramp function
Non-crimp fabric (NCF)	A fabric constructed from unidirectional crimp-free fibre layers, assembled together using a light stitching yarn.
Noodle	A resin-rich region in a composite T-piece
Preform	An arrangement of dry fibres in the three-dimensional (3D) component shape
Resin transfer moulding (RTM)	A moulding process that saturates a fibre preform placed in a closed mould with resin
Unit cell	A representative unit of a composite used in analysis (equivalent to a representative volume element)
Unidirectional (UD) composite	A composite reinforced by fibres aligned in the same direction
X-ray micro computed tomography (µCT)	X-ray imaging in 3D

Nomenclature

Roman letters

$\overline{AB}$	Length of line AB (mm)
$\widehat{AB}$	Length of arc AB (mm)
A_f^{yarn}	The total fibre area for a weft yarn cross-section (mm^2)
$A_{section}$	The area of the cross-section (perpendicular to the weft direction) of the flange (mm^2)
$Area_{ext}$	Total fibre area in yarn extension (mm^2)
c_i	i=1,2, empirical constants in damage model
D_{weft}	Spacing of weft yarns between through-thickness layers (mm)
D_{warp}	Spacing of warp yarn in the same layer (mm)
d	Distance from a specific fibre layer within the yarn to the reference fibre layer (mm)
d_{max}	The maximum value of d (mm)
d_o	Offset distance from the centre of nearest unbent weft yarn (mm)
d_f	Fibre diameter (mm)
d_i	i=1,2,3,4; damage parameter in Hashin's criteria
E	Young's modulus (MPa)
e	Element length (mm)
F	Material strength (MPa)
FL	Failure load (N)
G	Shear modulus (may have numbers *1*, *2*, *3* as subscript for material directions) (MPa); or energy release rate with letters *n*, *s*, *t* as subscript for normal, first shear, and second shear directions (mJ/mm^2)
G_d	Maximum width of the cross-sectional gap in a flattened weft yarn (mm)
H_{warp}	Height of warp yarn (mm)

H_{weft}	Height of weft yarn (mm)
H_{weft}^{fla}	Flattened height of weft yarn (mm)
I	Stress invariant
k	Interface stiffness (MPa/mm)
L_{ABCD}	The arc length of fibre ABCD (mm)
L_d	Arc length difference between fibre on a specific fibre layer, distance *d* away from reference fibre layer, and fibre on reference layer (mm)
l_0	Length of yarn width transition (mm)
n_{weft}	The total number of weft yarns in the flange
p	Power in equation for interface damage evaluation
P	Stiffness penalty factor in material damage modelling
R_0	Radius of curvature of the reference fibre within a bent yarn (mm)
R_d	Radius of curvature of the fibre that is distance *d* away from the reference fibre within a bent yarn (mm)
R_m	Radius of compaction mould fillet (mm)
$\overline{R_n^{warp}}$	Radius of curvature of centreline of warp yarn cross-section on yarn layer *n* (µCT measurement) (mm)
$\overline{R_n^{weft}}$	Radius of curvature of centreline of weft yarn layer *n* (µCT measurement) (mm)
R_n^{warp}	Radius of curvature of centreline of warp yarn cross-section on yarn layer *n* (calculated) (mm)
R_n^{weft}	Radius of curvature of centreline of weft yarn layer *n* (calculated) (mm)
S_θ	Warp yarn shift angle (radian)
S_d	Warp yarn shift displacement (mm)
ST	Structural stiffness (N/mm)
t	Thickness (mm)
V_f	Fibre volume fraction
V_f^{weft}	Fibre volume fraction in the weft direction
W_{warp}	Width of warp yarn (mm)

W_{weft}	Width of weft yarn (mm)
w	Displacement of out-of-plane fibre migration (mm)
w_i	Displacement of out-of-plane migration for fibre on fibre layer *i* within a yarn (mm)
W_{weft}^{ext}	Weft yarn width extension (mm)
W_{weft}^{fla}	Flattened width of weft yarn (mm)

Greek letters

α	A proportion of arc length difference L_d
$\bar{\alpha}$	The values of α for the ideally migrated fibres
A	A scalar for estimating interface stiffness in CZM method
β	A scalar for interface stiffness scaling in CZM method
δ	Separation in cohesive zone model (mm)
ε_{eff}	Effective strain for a composite with cohesive surface
ε'_{eff}	Effective strain for a perfectly bonded composite
τ	Traction in cohesive zone model with letters as subscript for normal, first shear, and second shear directions (MPa); or shear stress with numbers as subscript for material directions (MPa)
σ	Stress (MPa)
v	Poisson ratio

Subscripts

1	Fibre direction in the local coordinate system of the yarn
2	Transverse direction in the local coordinate system of the yarn
3	Through-thickness direction in the local coordinate system of the yarn
n	Normal direction
s	First shear direction

t	Section shear direction
m	Matrix
f	Fibre

Superscripts

t	Tension
c	Compression
C	Critical value for interface properties
y	Yarn
m	Matrix
v	Voxel model
d	The damaged state for yarn material
0	Initial failure stress for interface

Contents

Abstract I
Acknowledgements III
Glossary IV
Nomenclature V
Chapter 1 Introduction 1
1.1 3D woven composites and their applications 1
1.2 3D woven profiles 5
1.3 Motivation 9
1.4 Thesis overview 10
Chapter 2 Experimental testing of composite T-joints 12
2.1 Introduction 12
2.2 Literature review 12
2.3 Materials 17
2.4 Fabrication of T-joint specimens 18
2.5 Mechanical testing methodology 19
2.6 Test results 20
2.6.1 Load-displacement responses 20
2.6.2 Stiffness and damage initiation 21
2.6.3 Ultimate strength and damage progression 22
2.6.4 Characterisation of failure modes 23
2.7 Conclusions 26
Chapter 3 Geometric modelling of 3D woven preforms in composite T-Joints 28
3.1 Introduction 28
3.2 Literature review 28
3.3 Material characterisation 31
3.3.1 Warp yarn shift 33
3.3.2 Warp yarn cross-section bending 34

3.3.3 Weft yarn cross-section flattening 35
3.4 Geometric modelling 36
3.4.1 Warp yarn shifting 36
3.4.2 Warp yarn cross-section bending 38
3.4.3 Weft yarn cross-section flattening 39
3.4.3.1 In-plane fibre migration 41
3.4.3.2 Out-of-plane fibre migration 42
3.4.3.3 Yarn cross-section 44
3.5 Validation 48
3.5.1 Warp yarn shifting 48
3.5.2 Warp yarn cross-section bending 49
3.5.3 Weft yarn cross-section flattening 50
3.6 Conclusions 52
Chapter 4 Modelling approach for composite delamination based on meso-scale voxel method 54
4.1 Introduction 54
4.2 Literature review 55
4.3 Geometry, material properties and boundary conditions 58
4.3.1 Geometry and meshing 58
4.3.2 Constituent material properties 61
4.3.3 Boundary conditions 61
4.4 Cohesive zone model 64
4.4.1 Interface formulation 64
4.4.2 Interface stiffness 66
4.4.2.1 Conformal model interface 66
4.4.2.2 Voxel model interface 68
4.4.2.3 Effects of interface damage on the stiffness 71
4.5 Results and discussion 72
4.5.1 Baseline predictions 72
4.5.2 Effects of interface strength 75
4.5.3 Effects of interface stiffness 77

4.6 Conclusions 79
Chapter 5 Finite element modelling of 3D woven composite T-joints under quasi-static tensile pull-off loading 81
5.1 Introduction..... 81
5.2 Literature review..... 82
5.3 Construction of meso-scale 3D woven T-joint models..... 91
5.4 Boundary conditions..... 95
5.5 Constituent material properties..... 97
5.5.1 Determination of intra-yarn fibre volume fraction 97
5.5.2 Homogenized yarn properties..... 99
5.6 Damage modelling..... 101
5.7 Results 104
5.8 Conclusions 112
Chapter 6 Exploration of optimum weave pattern for 3D woven T-joint reinforcements 115
6.1 Introduction.....115
6.2 Weave pattern exploration 116
6.2.1 Basic design variables.....117
6.2.1.1 Yarn path straightness 117
6.2.1.2 Yarn path entanglement 117
6.2.1.3 Yarn path cross-over 117
6.2.2 Quantification of weft yarn path variations 118
6.2.3 New weave patterns.....118
6.3 Results 122
6.3.1 Damage resistance capability of the 3D woven T-joint models ... 124
6.3.2 Effects of yarn path crossover on stiffness and failure load..... 127
6.3.3 Effects of yarn path entanglement on stiffness and failure load... 129
6.4 Design philosophy for 3D woven T-joint reinforcement under tensile pull-off loading..... 131
6.5 Conclusions 133

Chapter 7 Discussion and conclusions 135
7.1 Introduction..... 135
7.2 Discussion..... 136
7.3 Conclusions 141
7.4 Recommendations for future work 142
References..... 145
Appendix A. The design of RTM mould for the T-joint specimens 157
Appendix B. Results of mechanical testing for T-joint specimens..... 162
Appendix C. Formulation for estimating the minimum interface stiffness in laminates..... 166
Appendix D. Generation of geometric models in TexGen 168
Appendix E. Load-displacement responses for 3D woven T-joints based on newly designed weave patterns 173

Chapter 1 Introduction

1.1 3D woven composites and their applications

Composite materials have long been used to meet the growing need for lightweight materials, primarily in the aerospace, wind energy, automotive and construction sectors, due to their high ratios of stiffness/strength to density along with advantages in energy absorption and fatigue performance. The recent large-volume usage of fibre reinforced composites in the Airbus A350 and Boeing B787 have demonstrated the maturity and recognition of these advanced materials. Due to the absence of through-thickness reinforcement, conventional laminated composite materials are prone to delamination under interlaminar stresses, which subsequently reduces the material properties and is considered as the most catastrophic failure mechanism for composite structures.

The desire to meet these challenges, alongside promoting adoption of out of autoclave composite manufacturing technology, has driven the development of 3D fibre reinforced composites. Fibres can be placed in the through-thickness direction after lay-up by processes such as stitching, tufting, Z-pinning, or alternatively, using 3D integrally braided, knitted or woven textiles to reinforce the composites. However, the in-plane properties might be sacrificed due to fibre damage caused by the stitching, tufting or Z-pinning steps, along with an increased manufacturing cost from these additional processes. 3D braided and knitted materials are highly interlaced textile structures exhibiting a high level of yarn path waviness (crimp), and it is well understood that crimp reduces the in-plane mechanical properties.

3D woven reinforcements are woven integrally in the form of multi-layered weaves. Benefiting from Jacquard weaving technology, straight warp and weft yarns can be placed at right angles to each other, and interlocked together by through-thickness yarns, leading to a minimal level of crimp and damage to the in-plane yarns. For composite applications, 3D woven preforms are generally classified into orthogonal, through-thickness angle interlock and layer-to-layer angle interlock patterns [1], according to the path of the through-thickness yarns (yarns shown in white in Figure 1-1). Restricted by the capability of conventional weaving looms, these patterns all have orthogonal warp and weft yarns, which might be less competitive under in-plane shear loading due to the absence of bias yarn layers. Design and manufacturing of emerging multi-axis 3D woven preforms incorporating bias yarn layers has also been proposed [2], through specifically developed weaving machines, but the development is still at an early stage for applications and will not be further discussed in this work.

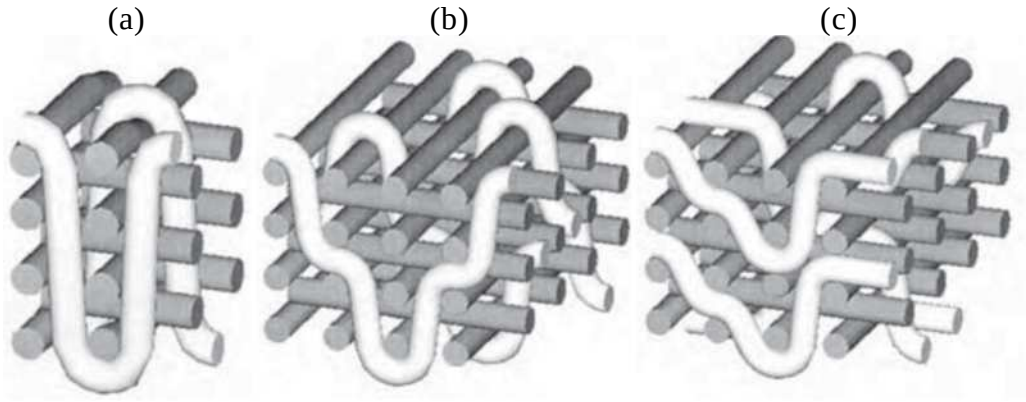


Figure 1-1 A general classification of 3D weave patterns for composites [1]: (a) orthogonal; (b) through-thickness angle interlock; (c) layer-to-layer angle interlock

As the preforms are woven directly into the 3D integral structures, the current manufacturing processes for 3D woven composites are liquid moulding processes such as vacuum infusion (VI) and resin transfer moulding (RTM) or its variants. Compared to conventional laminated composites, using 3D woven composites offers a number of advantages: (a) Enhanced mechanical properties in the through-thickness direction

delivered by the presence of through-thickness yarns, reducing the risk of delamination; (b) Improved cost efficiency resulting from the out-of-autoclave and lay-up free manufacturing processes. Additionally, assembly is not necessary for certain structures due to the ability to produce near net-shape preforms including geometric features; (c) Optimum mechanical behaviour towards specific loading conditions due to tailorable fibre architectures.

However, the interlacing feature of woven preforms still introduces some crimp at yarn cross-overs due to preform compaction in manufacturing, which potentially compromises the in-plane properties when compared with equivalent laminated composites [3]. More importantly, a major drawback for wide applications of 3D woven composites is the lack of mature design tools, to understand the relation between the varying fibre architectures and the resulting mechanical performance. This is still the subject of significant research [4, 5]. In addition, the width of the loom restricts the production of preforms for large composite parts.

Research and development activities on 3D woven composites started as early as the 1980s, but these materials have only been in production for engineering structures at a fraction of the volumes for laminated composites. Considered as one of the most advanced materials, 3D woven composites are generally selected to meet the increasingly tough needs of the aerospace industry for both structural performance and weight reduction, resulting from the pursuit of higher product performance, when other lightweight materials, including laminated composites, cannot meet these requirements.

One of the enabling technologies in the CFM International LEAP aircraft engine is the application of 3D woven composite fan blades (Figure 1-2). The composite fan blade is reinforced by a near net-shape 3D woven preform designed and manufactured by Albany Engineered Composites [6].

Along with other 3D woven composite components including the fan case, platform and spacers, the 3D fan module managed to reduce the engine weight by approximately 300 pounds (136 kg), compared to alternative metallic parts. In addition, the 3D woven composite fan blade offers higher damage tolerance and cost-effectiveness, as well as being lighter than the laminated composite alternative.

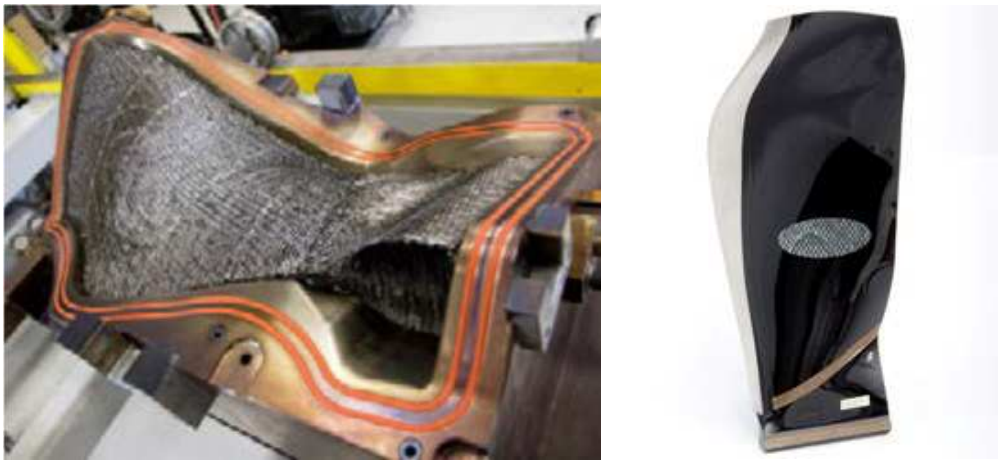


Figure 1-2 Left, near net-shape 3D woven preform for the fan blade in the RTM mould; right, a finished 3D woven composite fan blade [6]

A new 3D orthogonal woven composite material, named 3-Dimensional Multifunctional Ablative Thermal Protection System (3DMAT), has been developed by NASA, and will be used for the compression pads of the Orion Multi-Purpose Crew Vehicle in the upcoming lunar return mission and beyond, to replace the original 2D laminated material used in the first flight test limited to an Earth orbit return mission [5, 7]. The compression pad is the structural interface between the crew module and service module (Figure 1-3), serving as part of the thermal protection system during re-entry as well as to support the structural forces throughout the missions. 3DMAT, in which the 3D orthogonal quartz fibre preform is manufactured by Bally Ribbon Mills and then infused with cyanate ester resin through an RTM process, is shown to have significantly enhanced strength in the through-thickness direction and is able to withstand tougher aerothermal

heating environments, aiming to meet both the structural and thermal performance requirements for future deep space expeditions by Orion.

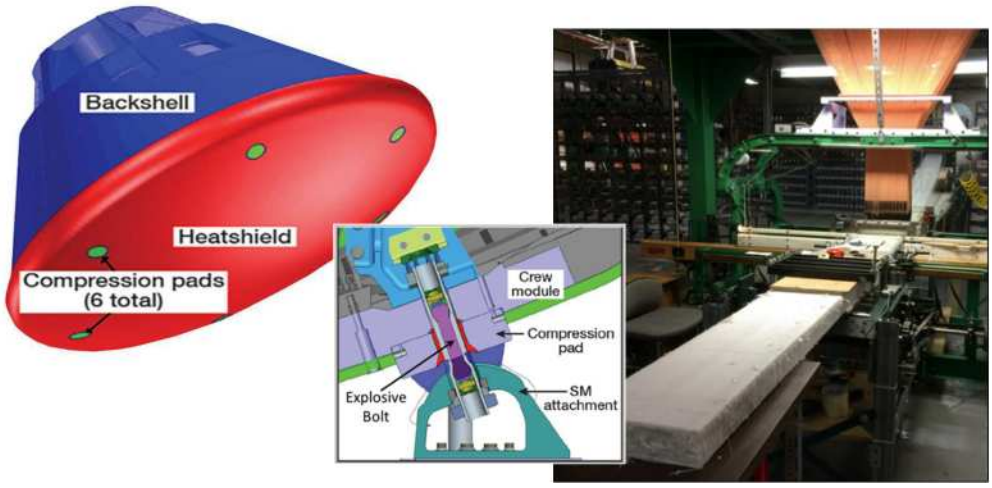


Figure 1-3 Left, Orion crew module highlighting the compression pads in the heatshield; right, 3D orthogonal quartz fibre preform being woven on a Jacquard loom [5, 7]

It is reported that 3D woven composites have also been innovatively used in the main landing gear brace for Boeing B787 [8] and Rolls-Royce LiftFan for the F-35B aircraft [9]. It is believed that if the current challenges in modelling techniques are addressed, 3D woven composite materials will be even more competitive for aerospace applications.

1.2 3D woven profiles

3D weaving technology gives independent control of individual warp yarns. In addition to producing flat and thick cross-section 3D preforms, it further enables the manufacturing of advanced near net-shape profiles, through incorporating geometric features such as bifurcations, curvatures, and changes in cross-sections, into the flat-woven preforms.

Introducing bifurcations is commonly used to manufacture near net-shape preforms for T, Pi, I, X shaped structures (Figure 1-4). Instead of using the

through-thickness reinforcements to interlock the whole preform, when an area of a preform is separately reinforced in the thickness direction by different yarns to form a locally unreinforced plane between the yarn layers, the preform can be separated at that plane to form a bifurcation.

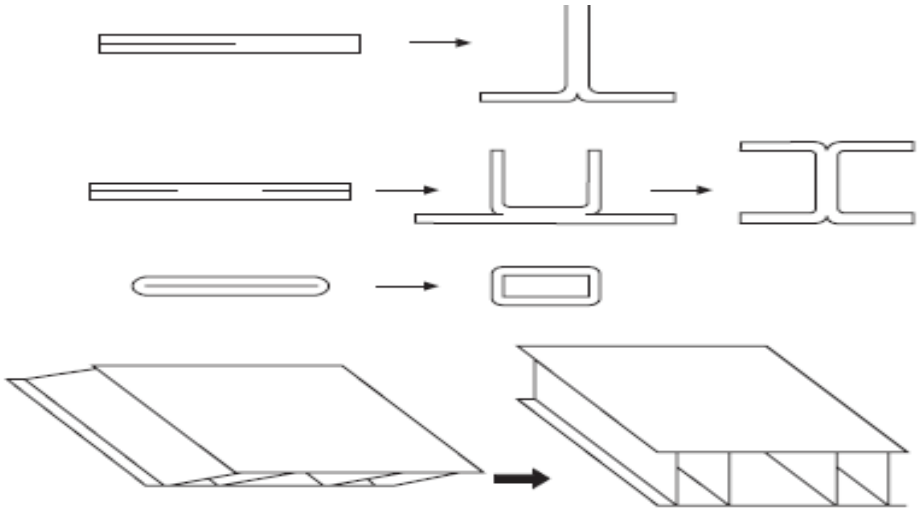


Figure 1-4 Example structures that can be made from the bifurcation method [10]

Profile shapes made in this way are often seen in structures such as stiffeners and joints. As the 3D profiles have continuous fibres running through the structures and eliminate the need for assembly, ongoing research aims to determine whether composites made from these 3D woven profiles can replace the current metallic or laminated structures widely used in the aerospace industry. For wind energy applications, Sharps from 3TEX Inc. and colleagues [11] have found that significant advantage can be gained in the load-bearing capacity of wind blade joints after replacing the laminated design with 3D orthogonal woven Pi preforms, which also deliver reduced manufacturing costs. Figure 1-5 shows Pi shaped profiles fabricated by several leading companies using 3D weaving technology.

In addition, as shown in Figure 1-6, hollow structures can also be manufactured if the bifurcations are positioned in the middle of the preform, which can potentially be used in sandwich materials.

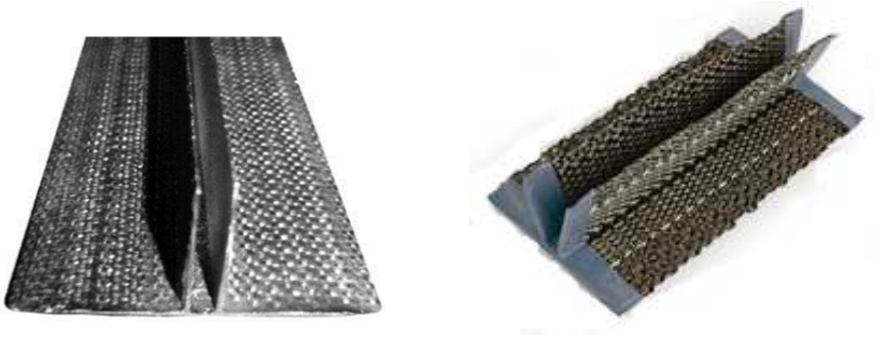


Figure 1-5 3D woven Pi shaped profiles manufactured by: left, Bally Ribbon Mills [12], and right, Albany Engineered Composites [13]

Laminated composite structures with tapering or varying cross-sections are often made by ply drop-off or cutting, adding additional costs to the manufacturing process as well as leaving discontinuous fibres in the materials. However, these problems can be overcome if 3D weaving technology is used to manufacture such structures. One successful application example is the 3D woven fan blade of the LEAP engine (Figure 1-2). The design of the 3D woven preform was shown to be able to meet the complex aerodynamic geometry of the fan blade alongside offering higher impact resistance due to the 3D fibre architecture.

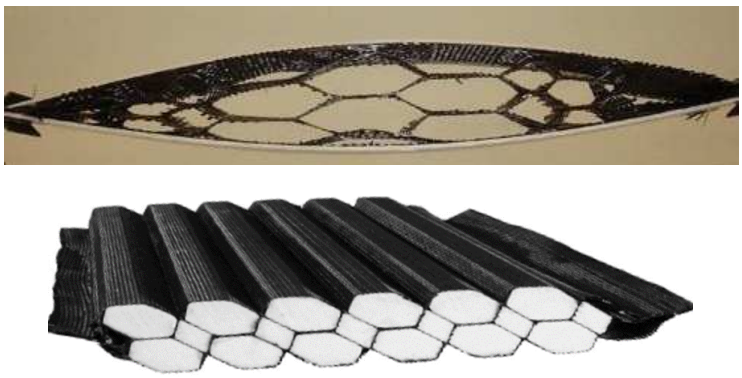


Figure 1-6 Hollow structures woven by: top, Sigmatex [14] and bottom, Bally Ribbon Mills [12]

Through contour weaving or polar weaving, inherent curvature can be introduced into the preform, which consequently would be much easier to

conform to the shapes of finished composite components with minimum wrinkles in the reinforcement. Pre-processing like preform cutting, darting or forming required for moulding a curved structure with 2D fabrics can be largely avoided, due to the high level of conformability of these specially designed 3D preforms. The 3D woven fan case of the LEAP engine benefits from this technology, and potential applications in other structures, for instance, an aircraft window frame and a gear box casing (Figure 1-7), are being considered [12].



Figure 1-7 3D woven profiles for aircraft window frame (top) and gear box casing (bottom) made by Bally Ribbon Mills [12]

Figure 1-8 also shows some promising woven profiles/structures which have non-orthogonal webs aiming to overcome the potential weakness under shear loading, caused by the absence of bias yarns in preforms. It should be noted that the number of preform shapes that can be made from 3D weaving is virtually unlimited, whilst this section only presents a few typical examples. 3D woven composites are most efficiently designed on a per application basis, as applications of such materials require expertise in

both weaving and design techniques.

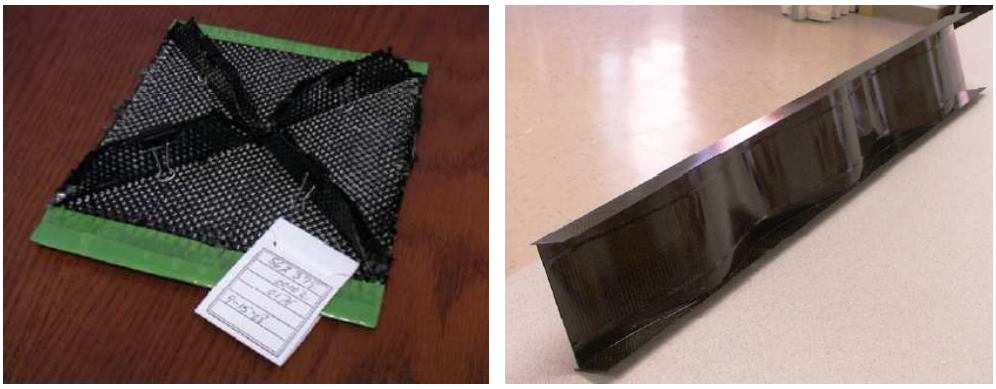


Figure 1-8 Left, 3D woven off-axis stiffener; right, prototype sine wave web beam [13]

1.3 Motivation

For 3D woven composite structures, especially for those with geometric features, the design space of their preforms is large as the design variables are not limited to fibre orientations and ply thicknesses, with an enormous amount of variations in the 3D spatial reinforcement architecture also available. Understanding the influence of the fibre architecture of 3D woven composites on their mechanical properties is fundamental to the material design phase. However, at present this is mainly dependent on experimental testing [15-18], due to the lack of analysis techniques that are able to accurately predict the resulting structural performance for 3D weave architectures, which restricts the application of 3D woven composites. Based on the textile geometry preprocessor TexGen developed at the University of Nottingham [19] and finite element (FE) analysis, this thesis aims to meet these challenges through developing modelling and design techniques for 3D woven composite T-joints, in which near net-shape preforms are manufactured by the aforementioned bifurcation method, with the desire to promote the application of such structural elements particularly in aerostructures.

1.4 Thesis overview

Chapter 2 examines the mechanical properties of composite T-joints experimentally, including two types of 3D woven T-joint with only weave variation at the junction and one type of laminated T-joint for comparison, under quasi-static tensile pull-off loading. The aim is to identify the benefits that the 3D woven T-joints can offer over 2D alternatives, and more importantly, the effects of fibre architecture of the 3D woven T-joints on mechanical properties. The details of material description, T-joint specimen manufacturing, testing method and results are given in this chapter.

Chapter 3 describes a geometric modelling approach developed to model the deformation in the 3D woven T-joint reinforcement caused by the bifurcation process. This intends to improve the accuracy of meso-scale geometric models towards the realistic fibre architectures in the composites, which is of great importance for subsequent material performance modelling in Chapter 5. The deformation modelled by the proposed analytical algorithm is compared with real fibre architecture characterised by x-ray micro-computed tomography.

Chapter 4 justifies the use of a voxel mesh based FE approach to model yarn/matrix delamination, which has to be accounted for in the modelling framework proposed in Chapter 5, because conformal meshing is not readily available for composites with complex fibre architectures. This study is based on a simplified version of the tested 3D woven T-joint, so that direct comparison can be made between the voxel and conformal models.

Chapter 5 presents a meso-scale modelling framework that predicts fibre architectures of 3D woven composite T-joints and the resulting mechanical behaviour under quasi-static tensile pull-off loading as described in Chapter 2. Based on realistic fibre architecture models, this FE method accounts for

both interface and constituent material damage in the meso-scale model. The results of FE modelling are validated against experimental data obtained from the testing of the two types of 3D woven composite T-joint specimens from Chapter 2, in terms of load-displacement response, damage initiation and propagation.

Chapter 6 aims to understand the effects of fibre architecture on the mechanical behaviour of 3D woven T-joints under tensile pull-off loading through a parametric study, and accordingly to develop a philosophy for designing optimum 3D woven T-joint reinforcements. It first explores other possible weave variations for the 3D woven T-joint reinforcements, in which variations are applied at the junction of the T-joint. Newly designed T-joint models are evaluated using exactly the same procedure as proposed in Chapter 5, and results are compared to determine the mechanical responses from the weave variations. Finally, a design philosophy for 3D woven T-joint reinforcements under tensile pull-off loading is outlined.

Chapter 7 contains the discussion and conclusions of the work along with recommendations for future investigations.

Chapter 2 Experimental testing of composite T-joints

2.1 Introduction

To understand the influence of the fibre architecture of 3D woven composite T-joints on mechanical performance, as well as the benefits that 3D woven T-joints can offer over the equivalent 2D laminates, in this chapter, experimental testing is performed on two types of 3D woven T-joint with only weave variation at the junction, and one type of laminated T-joint. With the intention to promote the use of 3D integrally woven T-joints in aerostructures, a quasi-static tensile pull-off test is selected in the presented work, as this out-of-plane load case is one of the typical loading conditions for such structures [20-22]. However, the T-joints should also be fully evaluated under other possible loading conditions [23, 24] before application, and this is recommended for further work.

This chapter first presents a literature review of composite T-joints in Section 2.2, including their applications in aerostructures along with recent studies focusing on how to improve the mechanical properties of conventional laminated T-joints. It then describes the materials used and the manufacturing process for the 2D and 3D woven T-joint specimens in Section 2.3, 2.4, followed by a description of experimental techniques in Section 2.5. The results of mechanical tests are analysed in Section 2.6.

2.2 Literature review

Composite T-joints are commonly used in aerostructures for joining of composites, with typical applications including spar-to-skin and stiffener-to-skin interfaces in wing structures, as well as bulkhead-to-skin interfaces

in the fuselage [21, 23]. 'T' structures are also found as stiffeners to prevent skin buckling in aerostructures. The flange of the T-joint interacts with the skin, whilst the web provides an attachment to the substructure. For such applications, tensile and flexural loads are representative of typical in-service loading conditions [21], and hence they dominate the testing performed on T-joints in the literature (Figure 2-1).

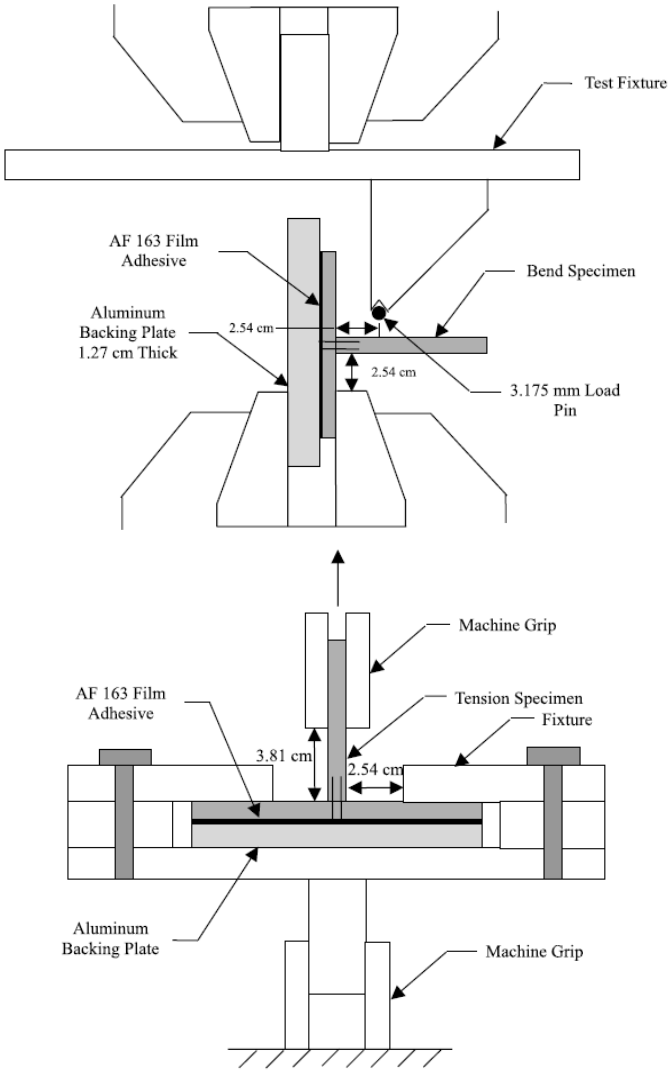


Figure 2-1 Bending (top) and tensile (bottom) testing layout in [21]

As composite T-joints are subjected to out-of-plane in-service loads, the catastrophic failure mode of delamination for laminates is commonly observed in laminated T-joints [20, 25, 26]. As a result, recent studies have

investigated the benefits of adding through-thickness reinforcements to composite T-joints. This includes inserting z-pins, stitches or tufts into laminated structures, as well as using 3D integrally manufactured reinforcement in the T-joints.

The effects of adding z-pins into composite T-joints has been experimentally and numerically studied in [27-32]. Through tensile pull-off tests performed on composite T-joints with and without z-pins (Figure 2-2), Koh et al.[27-29] found that introducing z-pins can improve the ultimate failure strength and total energy absorption of the T-joints by a maximum of 75% and 600% respectively at a z-pin content level of 4% by volume. However this does not raise the initial stiffness and damage initiation load. It was also shown that z-pins can improve the damage tolerance of composite T-joints with impact-induced cracks. The improvement in T-joint properties was attributed to improved delamination resistance by the bridging tractions across delamination cracks from the pins. It should be noted that the in-plane properties of the composites decreases with increase in z-pin volume content due to fibre damage resulting from the insertion process [33].

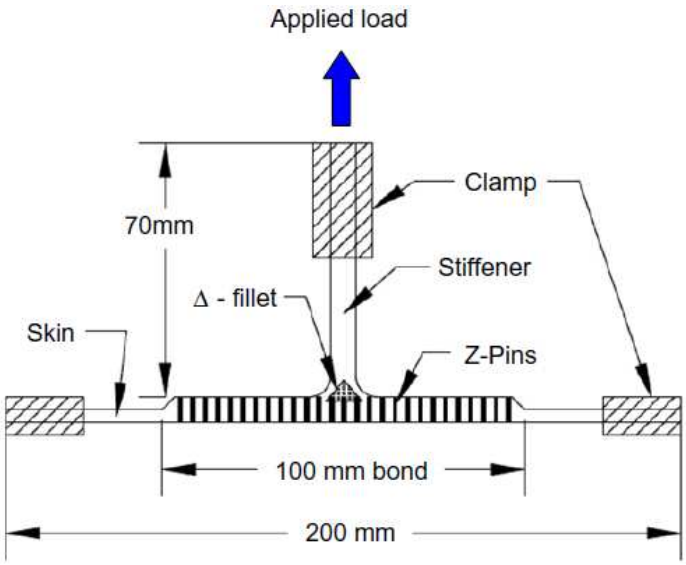


Figure 2-2 Tensile testing layout in [29] for z-pined T-joints

Tufting can also be used to reinforce laminated T-joints but this process is only suitable for dry preforms before liquid moulding (Figure 2-3). Cartié et al. [34] found the tufted T-joints had a ultimate strength twice that for T-joints without tufts under a tensile pull-off test, along with a higher total energy absorption. It was shown that delamination in tufted specimens was stopped by the tufting thread.

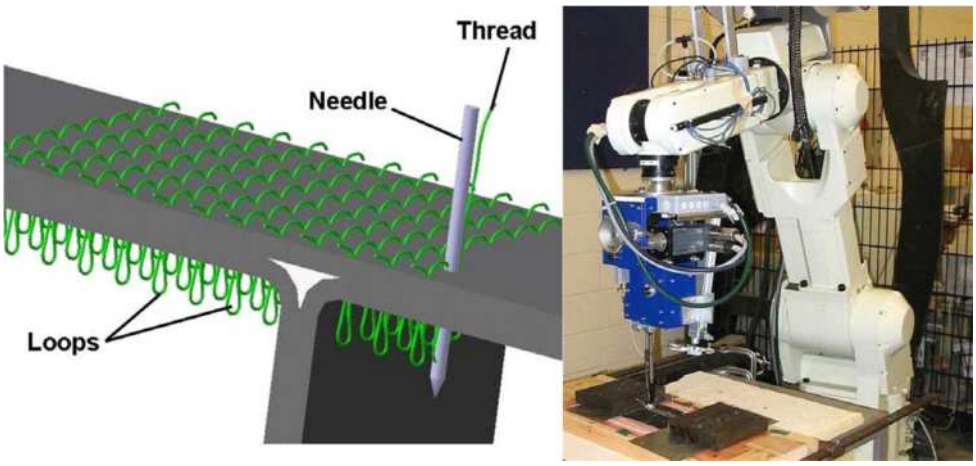


Figure 2-3 Schematic of tufting and equipment for the tufting process [34]

Yang et al. [22] studied the mechanical behaviour of 3D integrally braided T-stiffeners under tensile pull-off loading, in comparison with a 2D laminated alternative. They found that the 3D braided specimen did not show delamination at the junction region unlike the 2D specimen, and consequently the 3D braided T-stiffener achieved a large improvement in ultimate strength. They concluded this advantage benefited from the fibre architecture of the 3D braided T-stiffener which led to a uniform strain distribution at the junction region, instead of a severe stress concentration.

Soden et al. [15] assessed the influence of variations in the through-thickness reinforcement of 3D woven composite T-shaped specimens on mechanical behaviour under in-plane tensile loading (Figure 2-4), in comparison with a similar 2D laminated composite. It was found that the initial failure load of 3D woven specimens was similar to the laminated

specimen and not improved by the 3D woven fibre architecture; however the peak load and damage tolerance were significantly increased. Although weave variations in the 3D woven specimens were limited to the proportion of through-thickness yarns, significant differences were shown from the results. In general, the peak failure load increases with increasing level of through-thickness yarns. It was indicated by the authors that the weave variations affect the failure mode of the specimens but the relationship is complex.

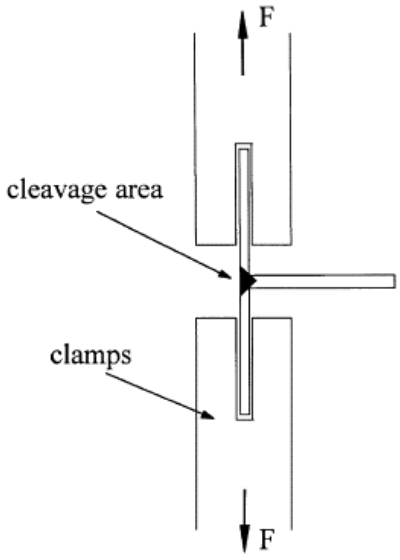


Figure 2-4 In-plane tensile testing layout in [15]

In general, it has been shown that z-pining, tufting or using 3D textile preforms in composites are all effective methods to improve the properties of composite T-joints, especially for suppressing delamination and improving damage tolerance. As discussed in Section 1.1, 3D woven materials are of particular interest in this work. Therefore, mechanical testing of the 3D woven T-joints is selected based on the tensile pull-off test, as it is a typical loading condition widely adopted by previous studies. Research to date has not addressed the mechanical performance of 3D woven composite T-joints under this loading case.

2.3 Materials

The two types of 3D woven T-joint preform used in this work were manufactured by Sigmatex based on Hexcel IM7 12K carbon fibre. Specimens were woven flat with pre-positioned bifurcations (as described in Section 1.2) on a Jacquard machine and then folded into a T shape. The preforms are based on a 3D orthogonal weave with the only variation at the junction. Figure 2-5 from x-ray micro computed tomography (µCT) shows the fibre architectures with the direction of weft yarns marked, illustrating type 2, where half of the weft yarns are crossing over the other half at the junction, in comparison with type 1.

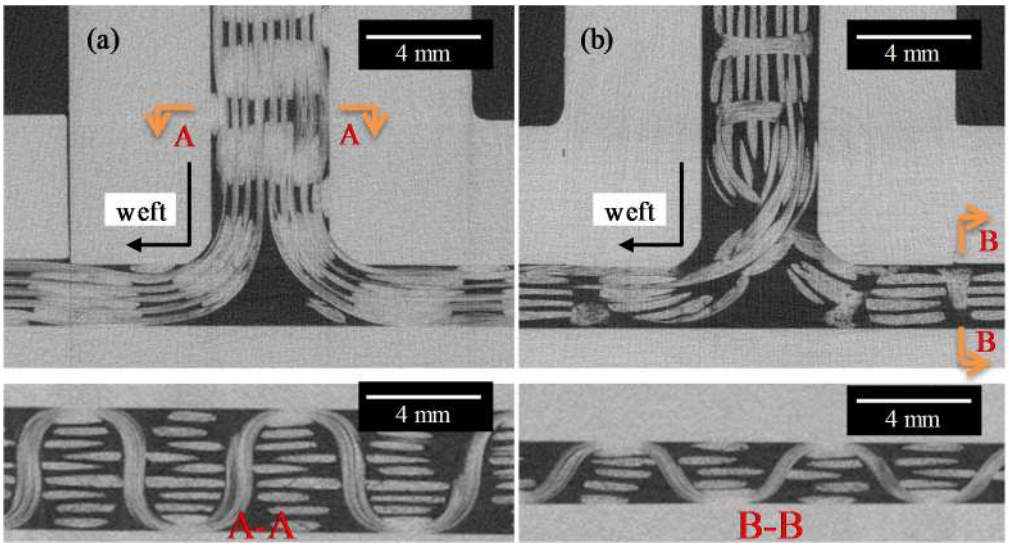


Figure 2-5 Images from µCT scan of the two types of 3D preforms showing the weave variation at the junction: (a) type 1; (b) type 2; section views show the weave pattern (orthogonal) at web and flange

This weave variation was formed by opening different sheds when inserting the weft yarns at the junction, which consequently changed the path of weft yarns at the junction only. The details of the µCT setup are described in Section 3.3. To facilitate understanding, schematic woven structures for the two types of 3D woven T-joint preforms highlighting the weave variation are presented in Figure 2-6. Both 3D woven preforms consist of 8 layers of

warp yarns and 9 layers of weft yarns in the web and 5 layers of warp yarn and 4 layers of weft yarns in the flange. More technical details about the 3D woven preforms are given in Section 3.3.

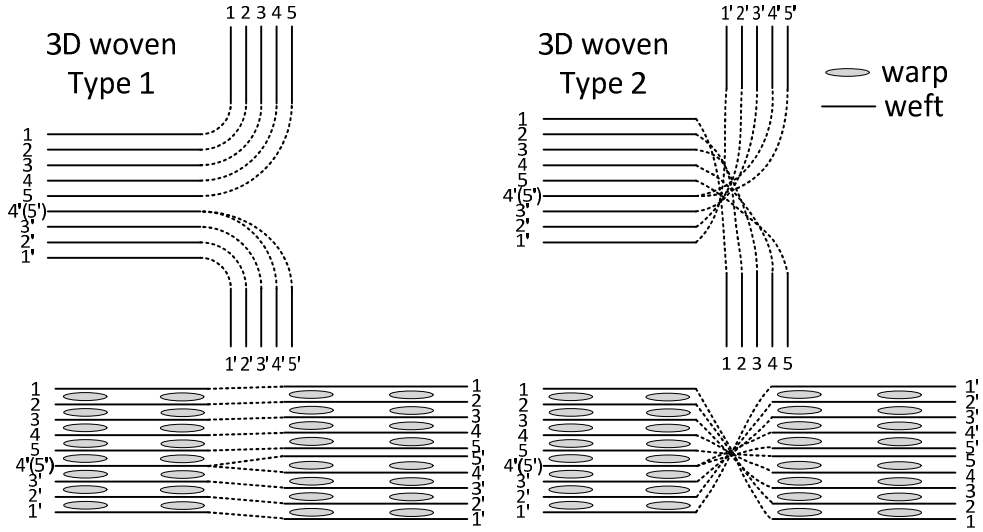


Figure 2-6 Schematic woven structures for the two 3D preforms after (top) and before (bottom) bifurcation, showing the weave variation at the junction (dashed line area), with binders omitted

2.4 Fabrication of T-joint specimens

A vacuum assisted resin transfer moulding (RTM) process was used for moulding the composite T-joint specimens (Figure 2-7), with the detail of the mould design given in Appendix A. The 2D woven specimens for comparison are made of 6 layers of 2×2 twill weave Hexcel IM7 12K carbon fibre fabrics with an areal density of 660g/m^2, infused with Gurit Prime 20LV epoxy resin, corresponding to a fibre volume fraction (V_f) of 56% with thicknesses of 4mm in the web and 2mm in the flange. The two types of 3D woven composite T-joint specimens reinforced by the above preforms were moulded in the same way as the 2D woven specimen, giving a V_f of 45%, which is calculated based on the preform areal weight. One preform (approximately 170 mm in width) for each type of T-joint was moulded. The resin infusion, assisted by a vacuum, took 10 to 20 minutes at room temperature and then the specimens were cured in an oven at 50°C for 16

hours. Acetone was applied on the mould surfaces as a mould release agent before moulding. It should be noted that 2D fabrics with suitable areal density to achieve a V_f of 45% were not available, resulting in a higher V_f for the 2D specimens.

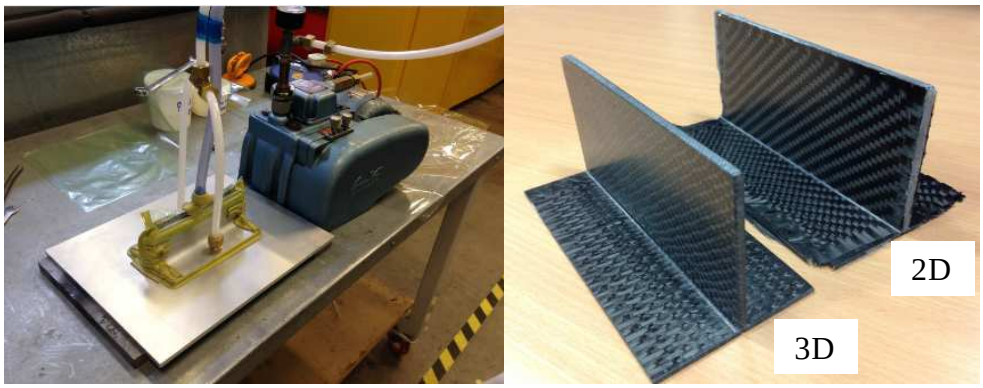


Figure 2-7 Vacuum-assisted RTM process (left) and moulded specimens before cutting (right)

2.5 Mechanical testing methodology

All three types of T-joint specimen were cut and tested under quasi-static tensile pull-off loading. Using a 50kN Instron 5581 testing machine, a displacement load at a constant rate of 1mm/min was applied on the web of the specimen, with the flange clamped at two ends by the fixture shown in Figure 2-8.

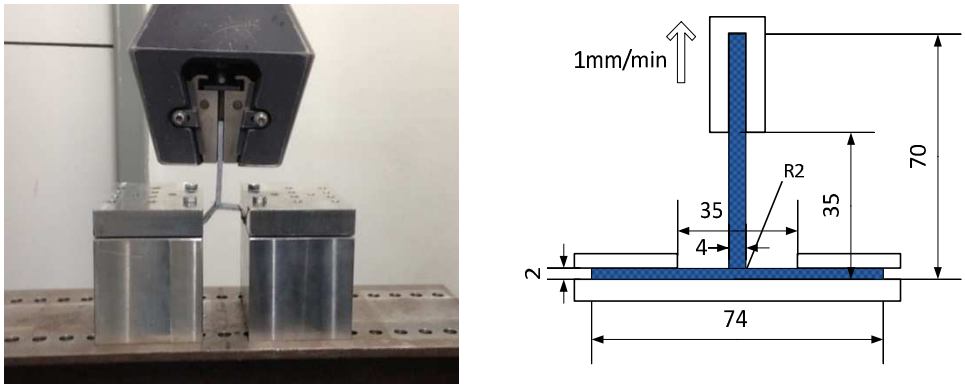


Figure 2-8 Testing layout for composite T-joints (units, mm), specimen width (out of page) is 20 mm

Testing continued after damage onset until the specimen fractured. A minimum of 3 specimens were tested for the 2D and 3D woven T-joints respectively at constant room temperature. Specimens were painted on the front cross-sections before testing and a DANTEC Q400 Digital Image Correlation (DIC) system was used to monitor the full-field strains around the junction regions of all specimens.

2.6 Test results

2.6.1 Load-displacement responses

Load-displacement responses for the three types of composite T-joints under tensile loading are plotted in Figure 2-9. Both linear response in load-displacement curves at the beginning (displacement less than 0.1 mm) and stiffness degradation after that can be observed for the two 3D woven T-joints.

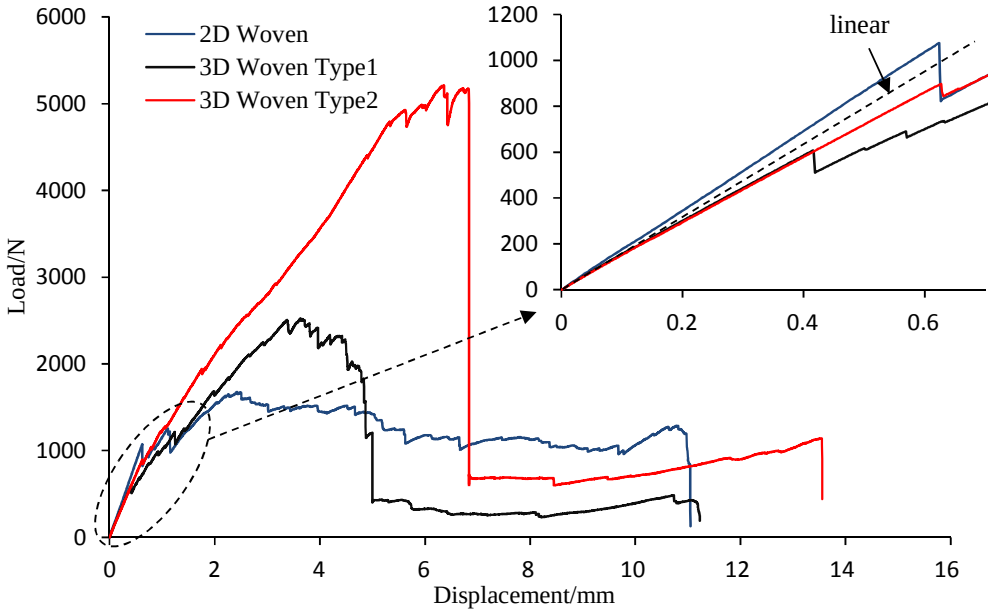


Figure 2-9 Load-displacement responses for the three types of composite T-joints, with initial section of the curves enlarged shown on the top right, the dashed line in the top-right figure represents the initial linear stiffness of 3D woven T-joints

Each of the curves demonstrates the failure process of one typical T-joint, and can be divided into three stages in terms of the failure: 1) from the start of loading to the first load drop that represents the initial stiffness and failure onset of the T-joint; 2) from the first load drop to the peak load showing the ultimate strength of the structure; 3) from peak load to final failure load showing the final extension on the T-joints needed to completely destroy the structure.

2.6.2 Stiffness and damage initiation

The enlarged figure in Figure 2-9 shows the initial section of the curves that presents the initial failure load and stiffness of the structure. The stiffness at a displacement of 0.35 mm, initial and ultimate failure load and their standard deviations are compared in Table 2-1. Standard deviations were calculated based on the complete experimental data for all tested specimens (Appendix B). This shows that the 2D woven T-joint has the highest initial failure load at approximately 1128N, from where a significant load drop can be observed, as well as a higher initial stiffness. This can be attributed to the higher V_f in the 2D woven T-joint. Although the two types of 3D woven joints have the same V_f, the initial failure load and stiffness of the 3D woven type 2 specimen are respectively 37.7% and 6.5% higher than those of type 1, which results from the weave variation at the junction.

Table 2-1 Stiffness, initial and ultimate failure loads of the three types of specimen, with standard deviations in brackets

Specimen configuration	Stiffness at 0.35mm unit: N/mm	Initial failure load[1] unit: N	Ultimate failure load[2] unit: N
2D woven	1627(±93)	1128(±44)	1620(±88)
3D Woven Type1	1378(±72)	710(±93)	2338(±152)
3D Woven Type2	1468(±32)	978(±59)	4951(±234)

[1] Initial failure load is defined at where a first significant load drop can be observed
[2] Ultimate failure load is defined at the maximum load

2.6.3 Ultimate strength and damage progression

3D woven composite T-joints show a significant improvement in energy absorption after damage initiation over the 2D woven T-joints in the tests. It is observed that the ultimate strength of the 3D woven type 1 specimens is improved by 44.3% over the 2D woven specimens, and the ultimate strength of the 3D woven type 2 specimens is 205.6% higher than that of the laminate as presented in Table 2-1.

The non-linear behaviour of the composite T-joints is more evident after damage initiation. The 2D woven T-joints show a greater degradation in stiffness after damage initiation as well as a lower extension to failure than the 3D woven T-joints. This is partially explained by the absence of through-thickness reinforcement that can prevent the propagation of damage. Moreover, the 3D woven type 2 specimens exhibit a higher post-failure stiffness than the 3D woven type 1 specimens. It is found that the weave variation alleviates strain concentration at the junction of 3D woven type 2 specimens to a large extent, as shown by strain distributions at a similar load after damage onset for the two types of 3D woven specimens in Figure 2-10.

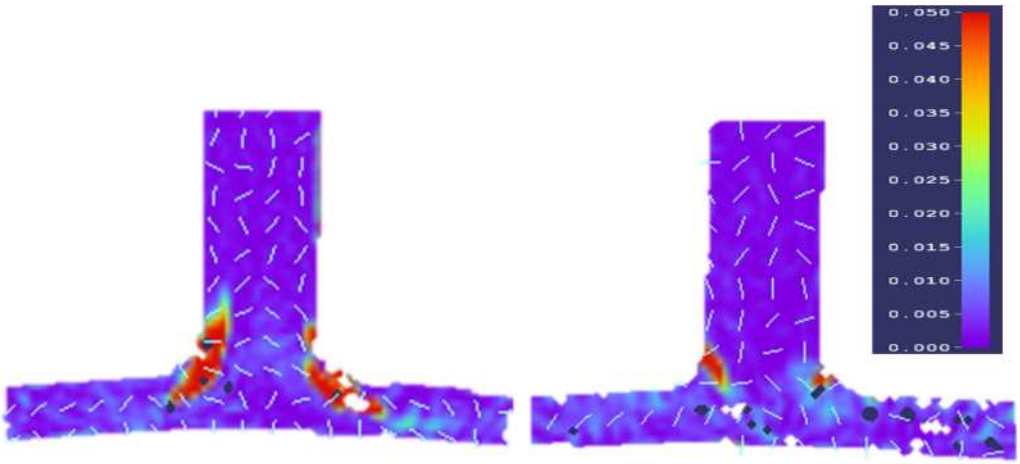


Figure 2-10 DIC images showing maximum principal strain distributions of 3D woven type 1(left) and type 2(right) T-joints at a load of 1079N for (a) and 1089N for (b) respectively, with lines representing strain directions

2.6.4 Characterisation of failure modes

Damage was initiated at the junction region of the three types of T-joint specimens and all tests ended by specimens rupturing at the edges of the clamps in the flange. Figure 2-11 shows the failure propagation progress at the junction regions. For the 2D woven specimen, a thin crack in the yarn/matrix interface was observed when failure initially occurred, and increasing load caused several obvious cracks at the junction until it reached the ultimate strength. After that the T-joint can no longer withstand further loading and delamination propagated to the web and flange of the T-joint until fracture occurred at the clamps. The main failure mode for laminated T-joint structures is delamination which has been extensively investigated in previous studies [20, 35], and thus it is only briefly discussed in this work. Similarly, yarn/matrix interface damage shown in Figure 2-11 (Stage 2), was observed to be the dominant failure mode for the 3D woven type 1 specimen. However, in Stage 3, in contrast to the 2D woven specimens, the binder yarns of 3D woven type 1 specimens at the junction limited the propagation of delamination into the web and flange which led to a higher ultimate strength. This comparison with the 2D woven specimen in terms of failure mechanism clearly demonstrates the effect of binder yarns in 3D woven composites on delamination resistance.

Post-mortem μCT scans were carried out to characterise the failure events inside the 3D woven T-joints. Figure 2-12 shows the severe delamination at the yarn/matrix interfaces along with fibre fracture in binders and weft yarns experienced by the 3D woven type 1 specimen. Transverse cracking in warp yarns, fibre fracture in binders and weft yarns, and matrix cracking were also observed in the 3D woven type 2 specimen as shown in Figure 2-13. Moreover, section views at A-A and B-B in Figure 2-12 further demonstrate the benefit of binder yarns in restricting the propagation of delamination. Unfortunately, an accurate sequence of damage events is not available due to the lack of in-situ μCT scan during the tests.

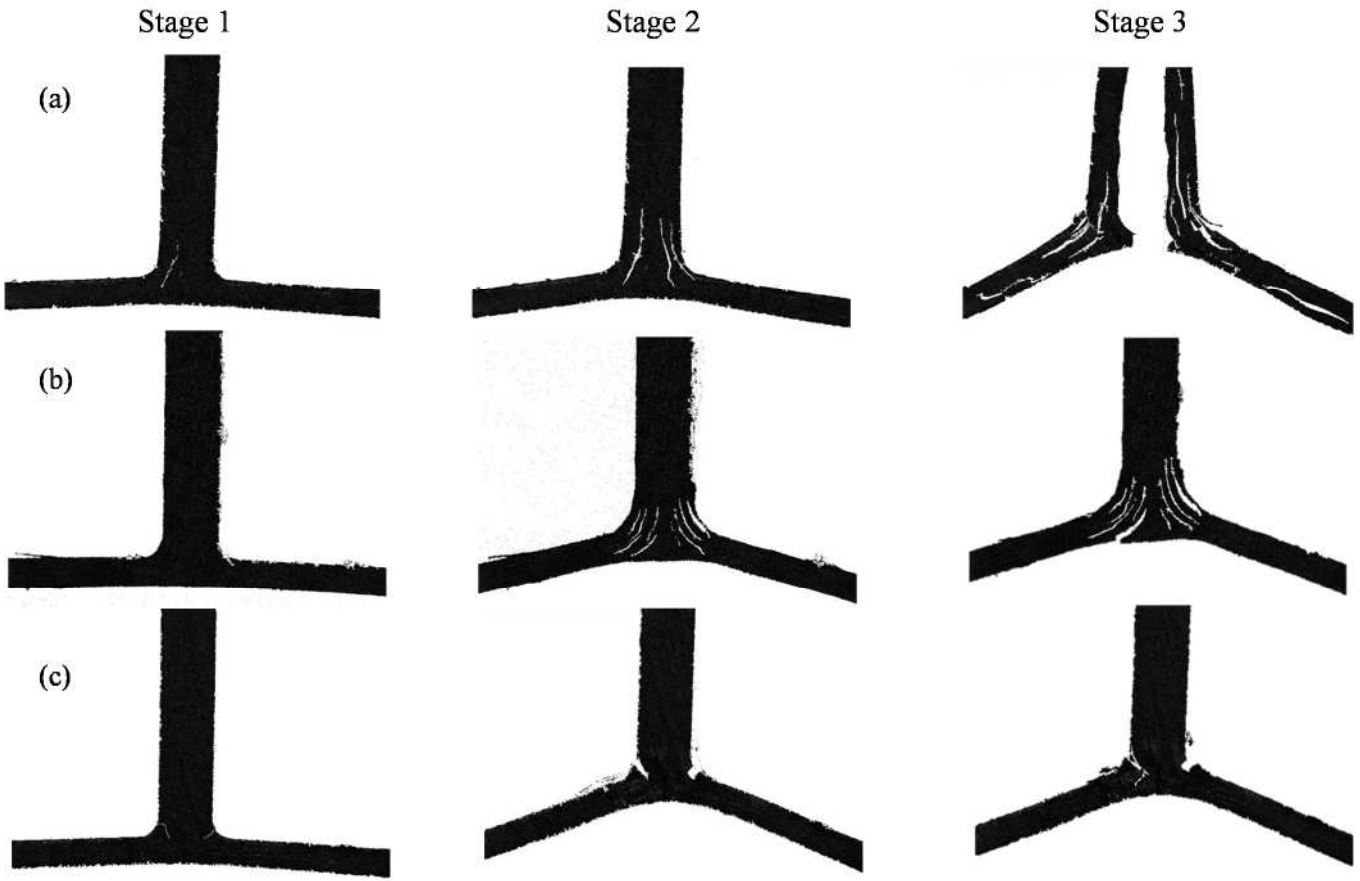


Figure 2-11 Photographs taken by DIC camera during tests showing the damage at the end of each failure stage: (a) 2D woven; (b) 3D woven type 1; (a) 3D woven type 2

The 3D woven type 2 T-joint specimen revealed a different failure mode in testing. As presented in Figure 2-13, resin cracking was first observed at the fillets of the specimen, where two resin-rich regions were formed because of its weave pattern. After that the cracks grew until fractures occurred in the flange near the clamps. Minor delamination, transverse and fibre ruptures were observed in the μCT scan of the failed specimen.

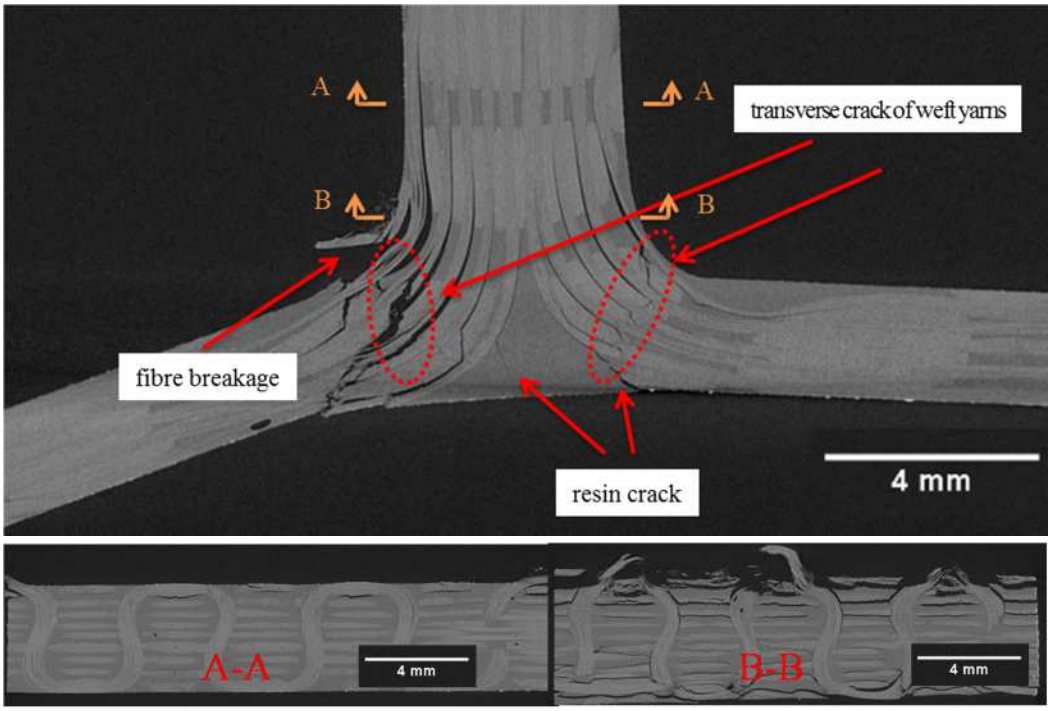


Figure 2-12 Failure events in 3D woven type 1 T-joint specimen

Varying the weave pattern is found to change the failure mode of 3D woven T-joints which corresponds to a significantly different load-displacement response. It is also concluded from the experimental work that delamination in composite T-joints is a catastrophic failure mode, as the specimen without dramatic interfacial damage absorbs more energy than those that failed because of delamination. This experimental assessment demonstrates that using 3D woven reinforcements is an effective way to improve the damage tolerance of composite T-joints by reducing delamination under tensile pull-off loading, and also that this potential improvement could be optimised with regard to reinforcement fibre architecture.

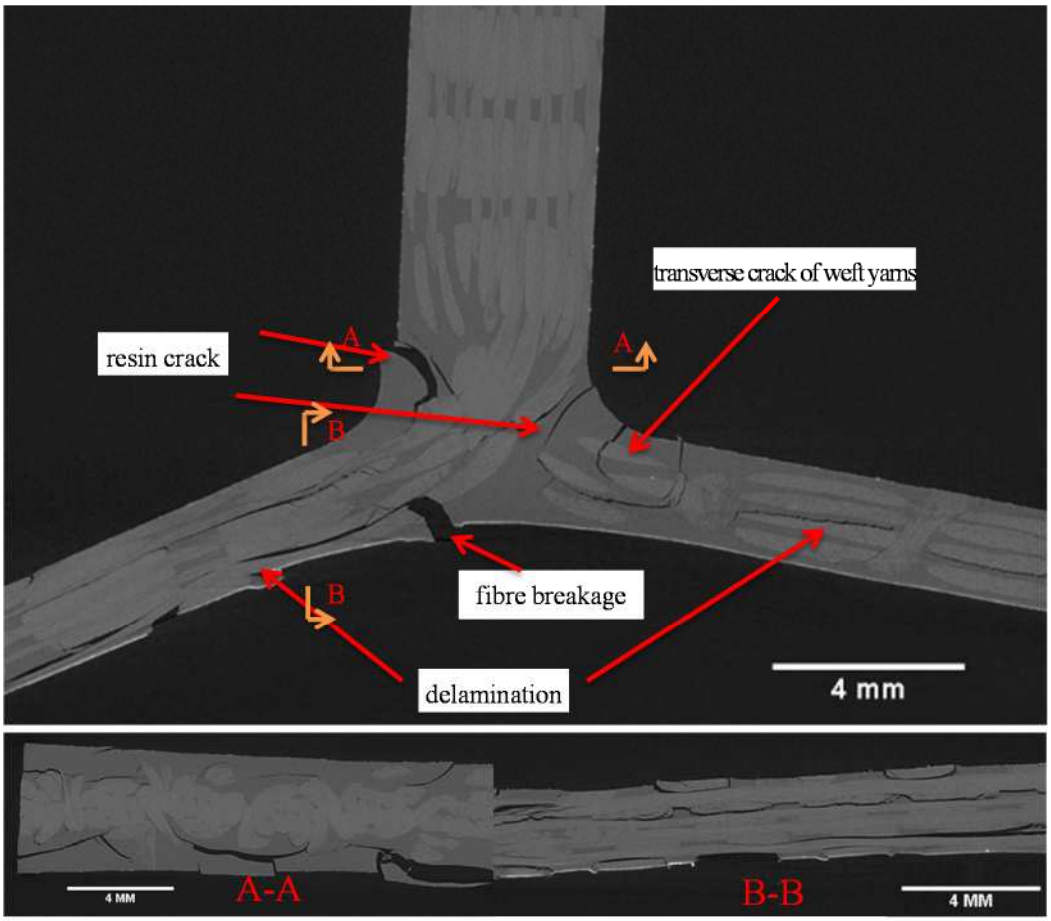


Figure 2-13 Failure events in 3D woven type 2 T-joint specimen

2.7 Conclusions

The mechanical behaviour of two types of 3D woven T-joint with only weave variation at the junction were evaluated under a quasi-static tensile pull-off test, along with one type of 2D woven T-joint for comparison. All samples were made of carbon fibre/epoxy resin through a vacuum assisted RTM process. The advantages of 3D woven composite T-joints in terms of ultimate strength and damage tolerance over the 2D alternative were shown in the testing, although the 2D woven T-joint was found to have higher stiffness and initial failure load due to its higher fibre volume fraction. More importantly, this work showed that variation in the fibre architecture resulting from opening different sheds when inserting the weft yarns can considerably enhance properties such as delamination resistance, damage

tolerance and total energy absorption to failure, as well as increasing slightly in the stiffness and initial failure load. This experimental assessment has demonstrated that using 3D woven reinforcements is an effective way to improve the load bearing capability of composite T-joints over laminates, and also that this improvement could be optimised with regard to fibre architecture.

Chapter 3 Geometric modelling of 3D woven preforms in composite T-Joints

3.1 Introduction

A common method to fabricate net-shaped 3D woven preforms for composite T-joints is to weave flat 3D preforms via a standard weaving machine with variation in binder yarn path and then separate the preform in the form of a bifurcation. Folding introduces fibre architecture deformation at the 3D woven bifurcation area. However, it was found by previous researchers that variability in fibre architecture affects significantly material properties including permeability and formability [36, 37]. The accuracy of the predicted composite performance can be improved based on a meso-scale model with realistic fibre geometry when compared with that based on an idealised model, as demonstrated for example by Green et al. [38]. As the reinforcement geometry plays a pivotal role in determining the composite's properties, a geometric modelling approach is proposed to represent the realistic fibre architecture, as a preprocessor for finite element analysis to predict composite structural performance. Supported by x-ray micro-computed tomography (μCT), three important deformation mechanisms are observed including yarn stack shifting, cross-section bending and cross-section flattening resulting from the folding process. Furthermore, a set of mathematical formulae for simulation of the deformations at the junction are developed and satisfactory agreement is observed when compared with μCT scan results.

3.2 Literature review

The exploration of 3D reinforced composites has included studies of load-bearing profiles such as T, I, and Pi shaped joints. As discussed in Section

2.2, there are three basic ways to manufacture 3D reinforced composite joints with woven preforms. The first method is to use 2D woven fabric lay-ups, reinforcing the through-thickness direction with tufting, stitching or Z-pinning [28, 34]. The second way is to weave flat 3D preforms via a standard weaving machine with variation of binder yarn path to form locally unreinforced planes (bifurcations) and then fold the preforms into the desired shape [15, 39-41]. The third way is to fabricate the preform directly into a complex 3D shape through a specially developed 3D weaving loom [12, 42, 43]. Although composites reinforced by the first method can offer better damage tolerance in terms of delamination than 2D laminated joints subjected to equivalent loads [24, 34], they can be less competitive in in-plane properties because of geometric defects or fibre damage caused by retrospectively inserting through-thickness reinforcements [44]. In addition, due to the high investment and innovation needed for developing a special 3D loom for the third kind of preform, 3D preforms woven by a conventional loom are popular for current composite T-joints and other profiles.

Deformation is likely to occur when folding a flat woven preform into a 3D shape. Because the internal architecture of a woven preform is complex, its variability in geometry can directly affect material properties such as the effective elastic properties [45]. Mechanical testing in Chapter 2 has also shown that reinforcement geometry plays an important role in determining the composite's failure behaviour, as two types of 3D woven composite T-joint with only weave variation at the 3D woven bifurcation area (in which the formed resin pocket is usually referred to as the 'noodle') were tested under the same tensile loading case but very different load-displacement responses were observed. Thus, in order to closely predict the properties of composite T-joints reinforced by a flat woven 3D preform, it is necessary to model the fibre architecture as realistically as possible.

Characterising the realistic fibre architecture of 3D woven composites is

difficult because of the complexity of the internal geometry, but this can benefit from the use of μCT [46, 47]. Some general frameworks for geometric modelling of woven preforms with respect to characterisation of yarn path, crimp and cross-section shape have been provided in the literature [19, 48-50]. Furthermore, compaction induced yarn crimp and cross-section shape change were studied with a number of models [51, 52], however, as they are based on beam theory, numerically solved by the finite element method, they are computationally intensive. Some mathematical methods were also proposed to model yarn cross-section shape under compression. An energy based method used to characterise yarn deformation in compression was developed by Lomov and Verpoest [53] but the method asks for a measurement of the mechanical properties of yarns in bending and compression. Chen et al. [54, 55] modelled yarn cross-section deformation of both single and multi-layer woven preforms under compaction at the mesoscopic level based on the assumption that yarn width deformation is negligible compared with the deformation of yarn thickness. The model is not applicable when yarn width change is significant, for instance for a yarn subjected to bending load. Cornelissen and Akkerman [56] observed yarn cross-section flattening in a cantilever experiment of yarns bending under their own weight. They concluded that cross-section flattening would affect the yarn flexural rigidity by one order of magnitude but they were not able to derive a trend from the experiment. However, yarn cross-section deformation in bending is significant as observed in this study via μCT analysis and an effective model is needed to capture this feature.

This chapter focuses on the geometric modelling of 3D woven preform deformation caused by folding a flat woven preform into a T-piece, which is a typical fabrication process for composite T-joints. Through the μCT analysis of a formed and compacted preform, three important deformation mechanisms specifically for this type of preform were observed, namely yarn stack shifting, cross-section bending and cross-section flattening resulting from the folding process. These features have been modelled

geometrically and the models have been compared against μCT analysis data of a 3D woven T-joint preform.

3.3 Material characterisation

To characterize the intrinsic geometric features of this flat woven preform for composite T-joints, the dry preform was compacted into a T-shape acrylic fixture and analysed via μCT as shown in Figure 3-1. The web section of the preform was firstly fitted in the fixture before bifurcation of the flange section, thus no deformation in the web is likely to be expected from preform bifurcation and the part of the preform contacting the fixture corner would conform to its radius of curvature.

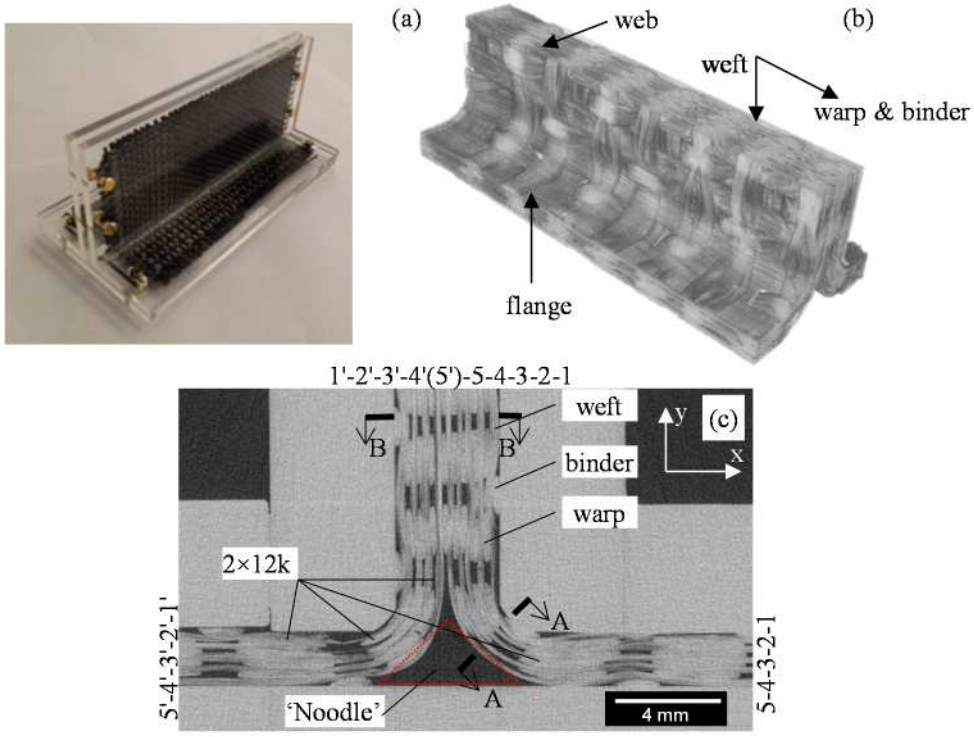


Figure 3-1 μCT scan of the preform: (a) dry preform compacted in an acrylic fixture; (b) preform visualised via volume rendering from μCT showing the yarn directions; (c) μCT section view of preform for 3D woven type 1 specimen with the numbers showing the numbering of weft layers

The GE phoenix v|tome|x m machine used a current of 240 μA and a voltage of 120 kV to achieve the imaging resolution of 30 μm per pixel in scanning. The compaction leads to an average fibre volume fraction of 45% which is the same as the 3D woven T-joint specimens in Chapter 2.

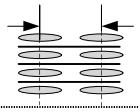
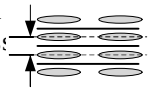
The preform has two geometric changes in its left-hand side: one is that the warp yarns at the junction are in twice the filament count as those in the web; the other is a weft layer in the web (numbered as 4'(5') in Figure 3-1) is formed of two weft yarns as used in other layers and separated into two layers (layer 4' and 5') at the flange, for the purpose of yarn layer balance in the flange. Meanwhile, the flange part of the preform was woven with warp yarns of 24k filament count. In addition, it should be noted that the only difference in the weave pattern between the two types of preform, as introduced in Section 2.3, is at the junction of the preform.

In this chapter, the proposed geometric models for predicting preform deformation are mainly applicable for 3D woven type 1 preform which is based on orthogonal weave pattern. The weave variation in 3D woven type 2 preform further complicates the fibre architecture so that modelling of its architecture is currently dependent on μCT characterisation.

In order to validate the proposed geometric modelling approach, necessary geometric parameters measured from the preform are listed in Table 3-1. Measurements of each parameter were made using the software ImageJ at a number of μCT slices covering different yarns, from which the average and standard deviation (SD) were obtained.

The folding process introduces additional yarn deformation at the junction of the 3D woven type 1 preform, and three significant features, namely yarn stack shifting, cross-section bending and cross-section flattening, were observed as described in the following sections.

Table 3-1 Measured geometric parameters of the 3D woven preform through μCT

Location	Yarn	Height(SD) in mm	Width(SD) in mm	Number of measurements
Web	warp(surface[1])	0.32(±0.04)	1.72(±0.08)	20
	warp(internal[2])	0.29(±0.02)	1.97(±0.08)	50
	weft(surface)	0.35(±0.03)	1.71(±0.07)	20
	weft(internal)	0.32(±0.03)	2.00(±0.13)	50
Flange	warp(surface)	0.35(±0.04)	3.61(±0.14)	20
	warp(internal)	0.31(±0.03)	3.85(±0.08)	20
Section A-A	weft layer1	0.28(±0.01)	2.63(±0.08)	20
	weft layer2	0.29(±0.03)	3.01(±0.11)	20
	weft layer5	0.29(±0.02)	3.57(±0.04)	20
		Spacing in the same layer(mm) 	Spacing between through-thickness layers(mm) 	
	warp	2.71(±0.03)	0.45(±0.10)	20
	weft	3.33(±0.16)	0.44(±0.04)	20

[1] surface yarns are those on the layers next to compaction fixture surfaces
[2] internal yarns are all other yarns except surface yarns

3.3.1 Warp yarn shift

The first distinctive deformation is the shift of the warp yarn stack at the junction, in the direction orthogonal to the yarn length direction. The warp yarns within the same stack are aligned vertically with each other before folding the preform, but their relative position is shifted after folding due to the rigid body transformation at the junction. However, the warp yarn shift could be suppressed by the surrounding binder yarns.

The shift begins in the warp yarn stack at the bend as marked in Figure 3-2, and is followed by the next 1-2 stacks in the flange. It is noted from the μCT scan that this phenomenon is most evident at the junction, and the level of shift reduces in the following stacks of warp yarns in the flange. To quantify the shift of the warp yarn stack, shift in the bend can be represented by angle shift S_θ, which is measured as the angle between the two lines

connecting centres of yarns to the normal direction of each yarn. Shift of the following stack is depicted as displacement shift S_d, representing the horizontal distance between two yarn centres as illustrated in Figure 3-2. The measured values for the warp yarn shift are compared with the model prediction in Section 3.5.1.

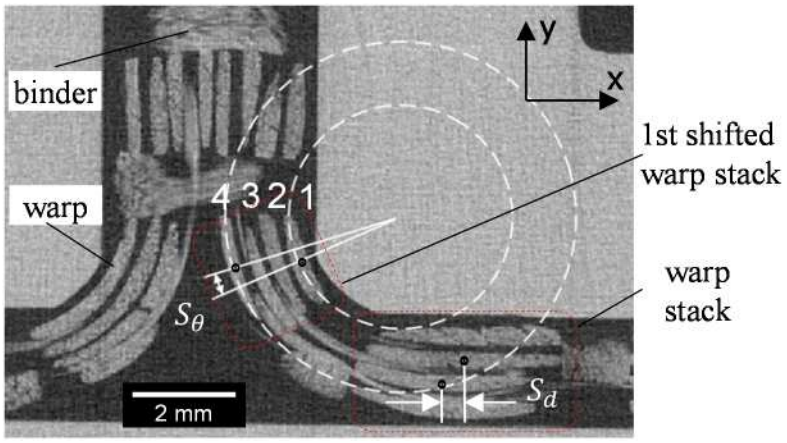


Figure 3-2 Warp yarn shift quantification at the junction (weft yarns not shown); numbers show the numbering of warp layers

3.3.2 Warp yarn cross-section bending

Bent cross-sections of warp yarns were observed at the junction. As shown in Figure 3-2, each warp yarn bends about the centreline (or centre-plane) of its cross-section uniformly along its length direction and its shape complies with the curvature of the adjacent weft yarn layers.

For this 90° folded preform, the centreline of each weft layer in the bend follows the path of a quarter of the circumference of a circle. As a result, the centrelines of bent warp yarn cross-sections could be approximated with circular paths of different radii. The measured radii of curvature of centrelines of bent warp cross-sections (R_n^{warp} in Figure 3-5) and weft yarn layers (R_n^{weft} in Figure 3-4) are listed in Table 3-2.

Table 3-2 Measured and calculated radii of curvature of centrelines of bent warp yarn cross-sections and weft yarn layers, where subscript *n* is the yarn layer number (mm; 5 measurements)

	Measured values		Calculated values (Eq.(3.1))	
	$\overline{R_n^{weft}}$	$\overline{R_n^{warp}}$	R_n^{weft}	R_n^{warp}
Layer 1	2.19(±0.07)	2.38(±0.10)	2.18	2.4
Layer 2	2.42(±0.12)	2.78(±0.15)	2.62	2.84
Layer 3	3.11(±0.08)	3.11(±0.14)	3.06	3.28
Layer 4	3.63(±0.12)	3.71(±0.13)	3.5	3.72
Layer 5	4.25(±0.10)		3.94	

3.3.3 Weft yarn cross-section flattening

In Figure 3-3, section view A-A of Figure 3-1 shows the cross-sections of weft yarns at the middle of the bend arc, while section B-B denotes cross-sections of weft yarns in the flat region. It is obvious that the cross-sections of weft yarns at section A-A are significantly flattened, i.e. an increase in yarn width and decease in yarn height, especially for those not sitting in the peak or trough of the binder yarn path since here yarn flattening is not constrained by binders.

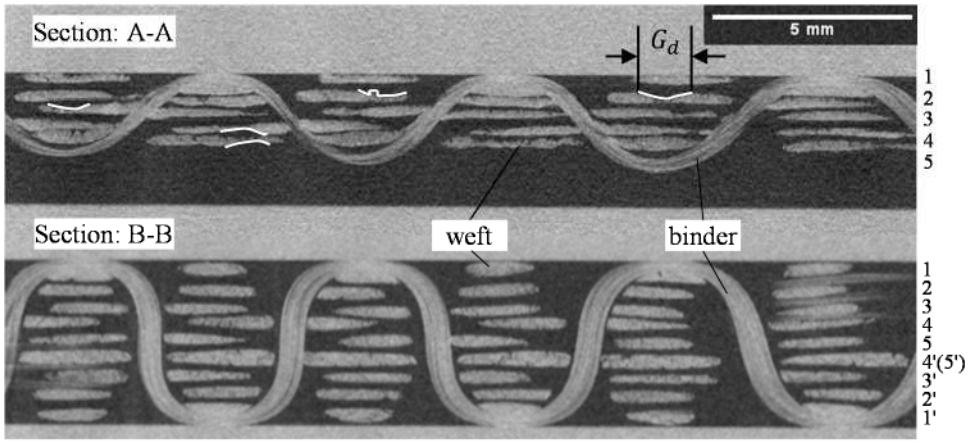


Figure 3-3 μCT images showing weft yarn flattening (A-A: flattened; B-B: non-flattened); serrated cross-section shapes are marked in Section A-A

The cross-section data of flattened weft yarns without binder constraint at position A-A were measured from the μCT scan and results are listed in Table 3-1. The layer sequence of weft yarns in section A-A is numbered as Figure 3-1 shows. From further observation of μCT images, the most slender cross-section of weft yarn occurs at position A-A in Figure 3-1, from where it transitions symmetrically back to the dimension of the yarn cross-section in the flat part of the preform. It is also observed that the length of yarn width transition varies for yarns on different layers, but all the flattened yarns are of almost same height as shown in Table 3-1.

Meanwhile, a number of gaps in yarn cross-sections at section A-A were observed, which caused serrated cross-section shapes in most of the weft yarns as marked in Figure 3-3. A number of different slices near section A-A indicate this phenomenon and therefore it is unlikely to be an artefact of the μCT scan. The position of each gap appears random as observed and the cross-sectional gap is simply quantified by its maximum width that is named gap distance G_d. The value of G_d is no more than 1.5 mm from several measurements. The flattening and cross-sectional gaps of weft yarns at the bend partly result from fibre migration when the preform is folded [57].

3.4 Geometric modelling

3.4.1 Warp yarn shifting

The warp yarn shift is inevitable due to the rigid body transformation at the junction. Each warp yarn has a different radius of curvature of cross-sectional centreline to the fillet origin *O*. As illustrated in Figure 3-4, half of a flat piece of 3D woven preform (left) is folded to a 90° angle (right). R_1^{weft}, R_2^{weft} and R_3^{weft} are the radii of curvature of centrelines for weft yarns on layer 1, 2 and 3 respectively. As the radius of the inner surface of a T-piece is confined by the mould corner radius R_m, the following can be

obtained:

$$\begin{aligned} R_1^{weft} &= R_m + \frac{H_{weft}}{2} \\ R_2^{weft} &= R_1^{weft} + D_{weft} \\ R_3^{weft} &= R_2^{weft} + D_{weft} \\ R_n^{warp} &= (R_n^{weft} + R_{n+1}^{weft})/2 \end{aligned} \tag{3.1}$$

where H_{weft} is the height of the weft yarn; D_{weft} is the spacing between through-thickness weft layers; R_n^{warp} is the radius of curvature of centreline for the warp yarn cross-section on layer *n*.

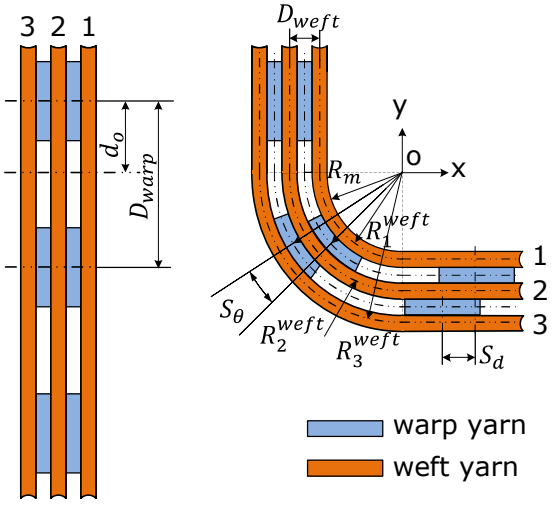


Figure 3-4 Schematic view of warp yarn shift due to rigid body transformation

Assuming there is no yarn sliding, angle shift S_θ between warp yarn layer 1 and layer 2 (in radians) in Figure 3-4 can be expressed as:

$$S_\theta = \frac{2(D_{warp} - d_o)}{R_1^{weft} + R_2^{weft}} - \frac{2(D_{warp} - d_o)}{R_2^{weft} + R_3^{weft}} = (D_{warp} - d_o)\left(\frac{1}{R_1^{warp}} - \frac{1}{R_2^{warp}}\right) \tag{3.2}$$

where D_{warp} is the warp yarn spacing within the same layer, and d_o the offset distance from the centre of nearest unbent weft yarn describing the position where the weft yarns start to bend; therefore $D_{warp} - d_o$ denotes the arc length in between bending onset position and bent yarn centre along the bend.

Also, the displacement shift S_d in adjacent layers for the following stacks of weft yarns can be described as:

$$S_d = \frac{\pi}{2}\left(\frac{R_2^{weft} + R_3^{weft}}{2} - \frac{R_1^{weft} + R_2^{weft}}{2}\right) = \frac{\pi}{2} D_{weft} \tag{3.3}$$

3.4.2 Warp yarn cross-section bending

Yarn cross-section shapes have been approximated by elliptical, power elliptical and lenticular shapes which can be defined by parametric equations in two dimensions [19]. Therefore it is convenient to model the cross-section deformation by a parameterized transformation that can apply to every current parametric cross-section shape rather than defining a new description for a curved cross-section. The cross-section of one warp yarn is presented in Figure 3-5 prior to and after deformation, where *x* and *y* represent the original yarn width and yarn height directions, and the origin is at the yarn centre. Accordingly the *x* and *y* coordinates of the original cross-section (the dashed line in Figure 3-5) can be defined by:

$$\begin{aligned} C(t)_x &= f(t) \quad 0 \le t \le 2\pi \\ C(t)_y &= q(t) \quad 0 \le t \le 2\pi \end{aligned} \tag{3.4}$$

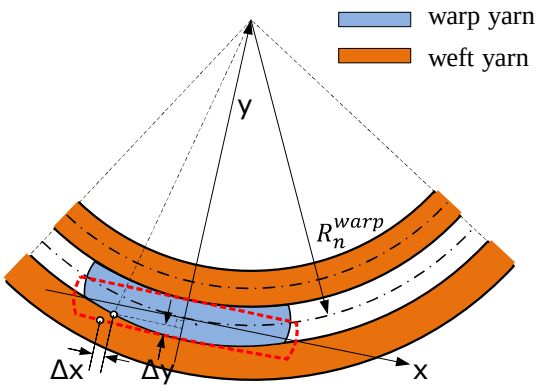


Figure 3-5 Schematic view of warp yarn cross-section bending

It is assumed that the bent shape is a result of a simple conformation of the major axis from the axis *x* to the arc in radius R_n^{Warp} (Eq.(3.1)). Thus, for

each point on the upper half of the edge of a bent cross-section, the transformation can be achieved by adding (Δx, Δy) to the coordinates of corresponding points on the original cross-section, where Δx, Δy can be defined by:

$$\begin{aligned}\Delta x &= (R_n^{warp} - H_{warp}/2)\sin(\frac{C(t)_x}{R_n^{warp} - H_{warp}/2}) - C(t)_x \\ \Delta y &= (R_n^{warp} - H_{warp}/2)(1-\cos(\frac{C(t)_x}{R_n^{warp} - H_{warp}/2}))\end{aligned} \tag{3.5}$$

where H_{warp} is the height of the warp yarn. Similarly, for the point on the lower half of the edge of a bent cross-section, Δx, Δy are given by:

$$\begin{aligned}\Delta x &= (R_n^{warp} + H_{warp}/2)\sin(\frac{C(t)_x}{R_n^{warp} + H_{warp}/2}) - C(t)_x \\ \Delta y &= (R_n^{warp} + H_{warp}/2)(1-\cos(\frac{C(t)_x}{R_n^{warp} + H_{warp}/2}))\end{aligned} \tag{3.6}$$

Usually the value of $H_{warp}/2$ is quite small compared with R_n^{Warp}, thus the above equations can be simplified into one transformation for all the points on the cross-section:

$$\begin{aligned}\Delta x &= R_n^{warp}\sin(\frac{C(t)_x}{R_n^{warp}}) - C(t)_x \\ \Delta y &= R_n^{warp}(1-\cos(\frac{C(t)_x}{R_n^{warp}}))\end{aligned} \tag{3.7}$$

3.4.3 Weft yarn cross-section flattening

As shown in Figure 3-4 for half of a T-joint, each weft yarn is under a bending load. An idealized fibre distribution in the weft yarn would consist of parallel layers with concentric arcs whose arc lengths are dependent on each layer's radial position. For illustration, Figure 3-6 represents a multi-filament yarn by inner, middle and outer fibres/layers. The model assumes that a fibre with high stiffness, such as carbon or glass fibre, has negligible

axial deformation in a bent yarn. After folding a straight yarn (Figure 3-6 (a)), it is clear that the assumed fibre arrangement in Figure 3-6 (b) would lead to a fibre length difference which would not be realistic, in order to satisfy the boundary condition that a fibre bundle is undisturbed beyond the bending location. Meanwhile, Figure 3-6 (c) shows another scenario where a fibre bundle with constant length complies with a 90^{o} bend resulting in fibre ends at a sheared angle, which contradicts the real boundary condition. Therefore, to maintain constant fibre length at a localised 90° bend, fibres tend to migrate and rearrange resulting in a flattened yarn cross-section as observed in Figure 3-3.

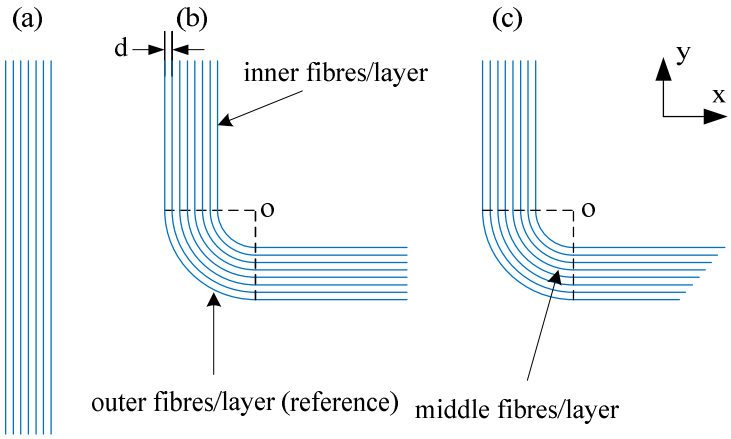


Figure 3-6 Idealized fibre arrangement in a 90° bent yarn

Taking the outermost layer of fibres in Figure 3-6 (b) as a reference line for fibre movement, the rest of the fibres have to migrate to maintain their lengths. The positions of fibres except the reference ones in Figure 3-6 (b) are considered as base positions for the movement. Hence the length differences between fibre on a specific fibre layer and fibre on the reference layer can be expressed as:

$$L_d = \frac{\pi}{2} d \tag{3.8}$$

where d is the distance from a specific fibre layer within the yarn to the reference layer. In practice, d can be a series of discrete values depending on the fibre arrangement within the yarn.

There are two possible mechanisms for a fibre to migrate that maintains fibre length at a bending corner. One mechanism is to move in the yarn height direction, referred to as in-plane migration (i.e. in the *x-y* plane shown in Figure 3-7). The other way is to move in the yarn width direction, referred to as out-of-plane migration (*z* direction in Figure 3-8). In-plane fibre migration will result in a reduction of yarn height while out-of-plane migration will increase the yarn width.

3.4.3.1 In-plane fibre migration

A reference fibre and a fibre on a neighbouring layer before and after migration are shown in Figure 3-7. The fibre loci in the bend can be approximated by circular paths as shown in Figure 3-2, thus in this model each single fibre path is described by one quadrant and two tangential straight lines, such as R_0, l_a^0 and l_b^0 in Figure 3-7 for example (where script *0* or *d* refers to reference or neighbouring layer). The positions of the two tangent straight lines are assumed to be fixed in migration based on the μCT observation that weft yarn height is almost unchanged in the region away from the bend. According to the length relation in two axial directions shown in Figure 3-7, the following expressions can be obtained:

$$l_a^0 + R_0 = l_a^d + R_d + d \tag{3.9}$$

$$l_b^0 + R_0 = l_b^d + R_d + d \tag{3.10}$$

where R_0 is the radius of curvature of the reference fibre that can be expressed by the sum of radius of curvature of yarn centreline and half of the flattened yarn height; R_d is radius of curvature of the fibre that is distance *d* away from the reference fibre.

If a proportion α of the above defined arc length difference as shown in Eq.(3.8) is compensated by in-plane fibre migration, the arc length difference between migrated and base fibres is $\pi d\alpha/2$. Thus the relation between the length of the reference fibre and a migrated fibre on a layer

distance *d* away can be given as:

$$l_a^0 + \frac{\pi}{2}R_0 + l_b^0 = l_a^d + \frac{\pi}{2}R_d + l_b^d + L_d(1-\alpha) \tag{3.11}$$

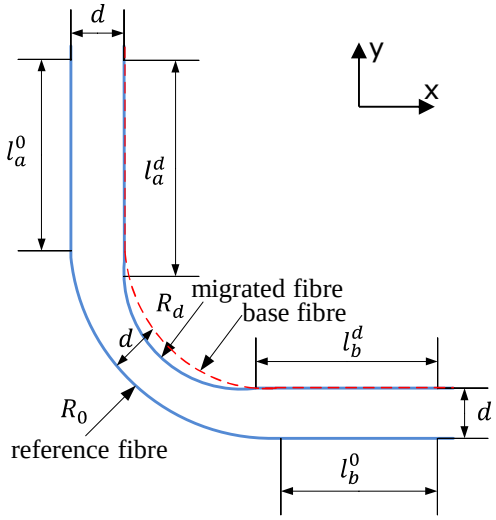


Figure 3-7 Schematic view of in-plane fibre migration

Hence, the in-plane path of a migrated fibre at distance *d* away from the reference fibre is described by:

$$R_d = R_0 - d - \frac{\pi\alpha d}{4-\pi}$$

$$l_a^d = l_a^0 + \frac{\pi\alpha d}{4-\pi}$$

$$l_b^d = l_b^0 + \frac{\pi\alpha d}{4-\pi} \tag{3.12}$$

3.4.3.2 Out-of-plane fibre migration

Since a proportion α of the defined fibre length difference is compensated by in-plane fibre rearrangement, the rest of the length difference, i.e. *(1-α)* of the whole length difference, has to be compensated by out-of-plane fibre migration to meet the assumption that the folding process would not increase the arc length of each fibre within a 90° bent yarn. In theory, fibres can migrate in both directions across the yarn width. In Figure 3-8, L_{ABCD} is the arc of a fibre which had in-plane but no out-of-plane migration so that

its arc length is given by:

$$L_{ABCD} = \overline{AB} + \widehat{BC} + \overline{CD} = 2(l_0 - R_d) + \frac{\pi}{2}R_d \tag{3.13}$$

where l_0 is the length of yarn width transition, denoted by length between A (or D) and G, from where the yarn width starts to change.

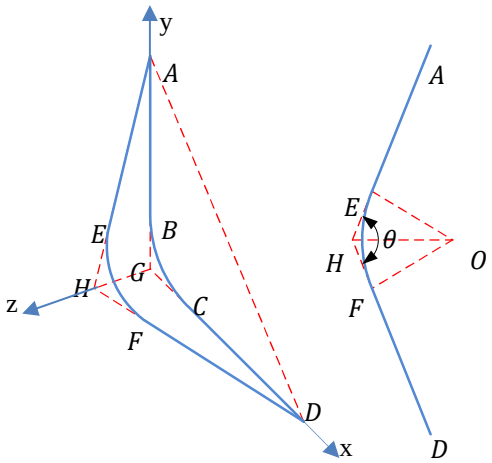


Figure 3-8 Schematic view of out-of-plane fibre migration

To calculate the arc length of a post-migration fibre L_{AEFD}, it is assumed that its radius of curvature is still the same as L_{ABCD}. $\overline{GH}$ denotes the distance that the fibre has migrated laterally, therefore in ΔADH:

$$\sin^2\frac{\theta}{2} = \left(\frac{\overline{AD}/2}{\overline{AH}}\right)^2 \tag{3.14}$$

Also, in ΔAGH and ΔADG:

$$\overline{AH}^2 = \overline{AG}^2 + \overline{GH}^2;\ \overline{AD}^2 = \overline{AG}^2 + \overline{GD}^2 \tag{3.15}$$

Hence, Eq.(3.14) is given by:

$$\sin^2\frac{\theta}{2} = \frac{\frac{1}{2}l_0^2}{l_0^2 + w^2} \tag{3.16}$$

where for simplicity l_0 equals $\overline{AG}$ or $\overline{DG}$; w equals $\overline{GH}$.

From trigonometry:

$$\tan^2\frac{\theta}{2} = \frac{l_0^2}{l_0^2 + 2w^2} \tag{3.17}$$

Hence, in ΔEHO $\overline{EH}$ is given by:

$$\overline{EH} = \frac{\overline{EO}}{\tan\frac{\theta}{2}} = \frac{R_d}{\tan\frac{\theta}{2}} \tag{3.18}$$

The arc length of migrated fibre L_{AEFD} is:

$$\begin{aligned} L_{AEFD} &= \overline{AE} + \widehat{EF} + \overline{FD} \\ &= 2\left(\sqrt{l_0^2 + w^2} - \frac{R_d\sqrt{l_0^2 + 2w^2}}{l_0}\right) + R_d\left(\pi \right. \\ &\left. - 2\tan^{-1}\left(\frac{l_0^2}{l_0^2 + 2w^2}\right)\right) \end{aligned} \tag{3.19}$$

Thus, the relation between fibre arc length differences caused by out-of-plane fibre migration can be represented by:

$$L_{AEFD} - L_{ABCD} = L_d(1 - \alpha) \tag{3.20}$$

Substituting Eq.(3.13) and Eq.(3.19) into Eq.(3.20), the displacement for out-of-plane migration *w* can be obtained for a fibre at a distance *d* away from the reference fibre.

3.4.3.3 Yarn cross-section

The process of fibre migration resulting from bending is complex, as each single fibre may have a different value of α for its in-plane and out-of-plane migrations. Ideally, if all fibres on the same layer move with the same α and direction for out-of-plane migration, the cross-section of a weft yarn, assuming a square array for fibre packing, at Section A-A in Figure 3-1 would have a parallelogram shape as shown in Figure 3-9 (b), where Figure 3-9 (a) is the fibre arrangement before flattening with its left-hand layer as reference for in-plane migration (Figure 3-7). Since there are thousands of fibres in a single yarn, a large number of fibres might migrate uniformly in the above way, i.e. without a change to their initial relative spatial sequence,

as shown for the fibres represented by black dots in Figure 3-9 (c) which remain in their ideal positions as in Figure 3-9 (b). Meanwhile, a few fibres, not following the above ideal migration law, can penetrate into a position out of their own layers through more in-plane migration once out-of-plane migration of fibres on prior layers makes a space, as indicated by grey dots in Figure 3-9 (c), which can cause a random serrated cross-section shape as observed in Figure 3-3. Additionally, a second possible cross-section shape is shown in Figure 3-9 (d) if it is assumed fibres move with the same α but in both directions for out-of-plane migration. Hereafter the first large group of fibres following the pre-migration relative spatial sequence are named ideally migrated fibres, and the second small group are called randomly migrated fibres. Under this assumption, the values of α for the ideally migrated fibres are supposed to be identically denoted by $\bar{\alpha}$. Therefore the yarn height could be characterised by the distance between two corresponding fibres on the outermost layer (reference) and on the innermost layer respectively as shown in Figure 3-10.

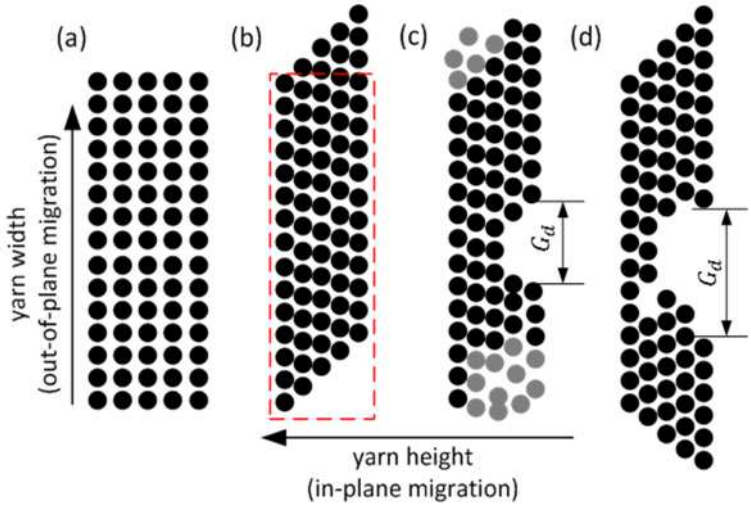


Figure 3-9 Schematic cross-section of fibre arrangement for a weft yarn showing fibre migration mechanisms: (a) pre-migration, square packing fibre arrangement; (b) post-migration, idealized migration; (c) and (d) post-migration, possible realistic migration accounting for serrated cross-section shape

If the flattened yarn height (at Section A-A in Figure 3-1) can be measured from a μCT scan, the value of $\bar{\alpha}$ for ideally migrated fibres on the innermost layer could be calculated by solving the following equation after substituting $R_{d_{max}}$ with Eq.(3.12):

$$H_{weft}^{fla} = R_0 - R_{d_{\max}} - \sqrt{2}dx \tag{3.21}$$

where d_{max} is the maximum value of d which is the original yarn height; $(-dx,\ -dy)$ in Figure 3-10 is the position of the centre of curvature of a fibre on the innermost layer in the coordinate system of reference fibre with its centre of curvature as origin, which is given by:

$$dx = dy = R_0 - R_{d_{\max}} - d_{\max} \tag{3.22}$$

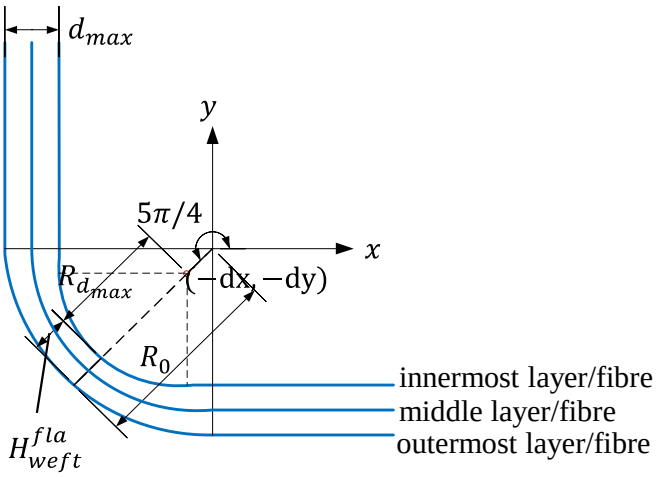


Figure 3-10 Yarn in-plane section view ($\bar{\alpha}$*=0.4;* d_{max}*=0.35*)

The yarn width is determined by the fibres that had out-of-plane migration. Irrespective of randomly migrated fibres and considering all fibres to be ideal ones migrating in the yarn width direction with an identical $\bar{\alpha}$, the relative migration displacement w could be obtained by solving a combination of Eq.(3.13), (3.19) and (3.20). In this case, if the yarn extension, defined as the area beyond its original cross-section (area of fibres outside of the dotted rectangle in Figure 3-9 (b)), for the flattened yarn is full of ideally migrated fibres, the total fibre area for fibres in the yarn extension can be roughly estimated by:

$$Area_{\text{ext}} = \sum_{i=1}^{n_f} w_i d_f \tag{3.23}$$

where d_f is the fibre diameter and n_f is the number of total fibre layers along the yarn height direction before flattening; w_i is the displacement of out-of-plane migration for a fibre on layer i.

In reality, ideally migrated and randomly migrated fibres coexist in a bent yarn so that a flattened cross-section can be near to rectangular with the observed gap (Figure 3-3) rather than a parallelogram (Figure 3-9 (b)) if all fibres are considered ideally migrated fibres. Some of the fibres, namely randomly migrated fibres, in the yarn extension do not have to move that much in the yarn width direction because there is enough space ahead of them to accommodate in-plane migration in the yarn height direction, and in the meantime the bending force will prioritise in-plane migration. Therefore a rectangular cross-section is likely to be formed, and a rough prediction of weft yarn width extension W_{weft}^{ext} in terms of constant fibre area in the yarn extension can be made by:

$$W_{weft}^{ext} = Area_{\text{ext}} / H_{weft}^{fla} \tag{3.24}$$

where the value of H_{weft}^{fla} should be known in advance.

However, it is not possible that different fibres on the same layer can move in both directions simultaneously for out-of-plane migration as shown in Figure 3-9 (d), because the measured G_d is much smaller than double the value of maximum w_k as calculated in the following section. Hence the predicted flattened yarn width can be expressed as:

$$W_{weft}^{fla} = W_{weft} + W_{weft}^{ext} \tag{3.25}$$

where W_{weft} is the original weft yarn width. This model is capable to predict the change of yarn cross-section if H_{weft}^{fla} can be determined.

3.5 Validation

Three proposed models for warp yarn shifting, cross-section bending and weft yarn cross-section flattening were compared to experimental data from the standard orthogonal weave region of the preform as listed in Table 3-1.

3.5.1 Warp yarn shifting

The value of R_m is 2mm which equals the radius at the junction of the acrylic fixture contacting the preform. Based on Eq.(3.1), the radii of curvature of centrelines for warp cross-sections and weft yarns on different yarn layers can be obtained as listed in Table 3-2, which shows good agreement with the measured values. The offset distance d_o for the preform is measured as 2.0 mm and thus the relative angle shift of a warp yarn can be derived by Eq.(3.2). Furthermore, the displacement shift in adjacent layers can be determined by Eq.(3.3). Since the yarn shift is not significant for this preform, the angle shift measurements were only taken between yarns on layer 1 and yarns on other layers, whilst the displacement shift measurements were carried out between yarns on layer 2 and 3, as numbered in Figure 3-2. The warp yarns shift in a uniform manner but show a deviation along the yarn length direction. The measured shift values taken at different cross-sections along the length direction with standard deviations are shown in Table 3-3 in comparison with predicted values.

Table 3-3 Warp yarn shift measured and predicted results (10 measurements)

	Angle shift $S_\theta(°)$ between			Displacement shift S_d(mm)
	layer 1 and 2	layer 1 and 3	layer 1 and 4	between layer 2 and 3
Measured value	2.96(±0.23)	-1.48(±0.17)	6.48(±0.25)	0.87(±0.13)
Predicted value	2.63	4.55	6.01	0.69

It is noticed that the measured angle shift between layer 1 and 3 is negative, which means the warp yarn on layer 3 has slid to the flange while folding. Warp yarn stack shift can be observed but the trend does not always agree

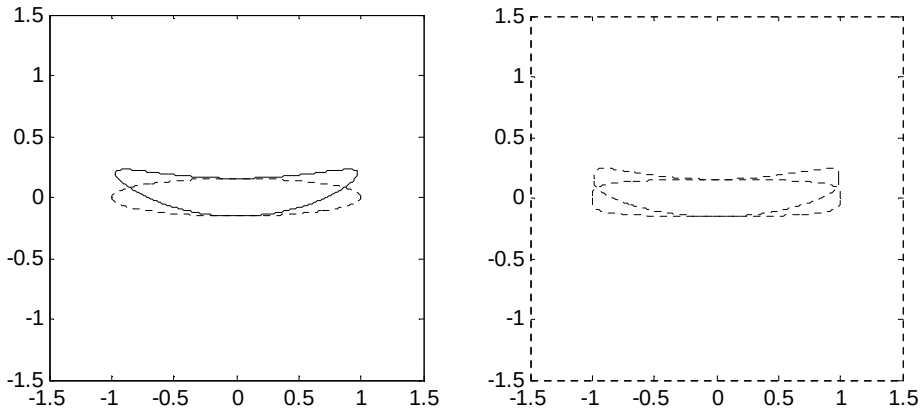
closely with the model since binder yarns influence the movement of warp yarns as well as yarn sliding induced by the weaving process.

3.5.2 Warp yarn cross-section bending

A bent cross-section shape can be obtained by the transformation defined in Eq.(3.7) on the basis of an original parameterized cross-section description. Figure 3-11 (a) is based on an elliptical cross-section and its radius of curvature of centreline is 3mm; Figure 3-11 (b) is transformed from a power ellipse (Eq.(3.26)) with m=0.4 where radius of curvature of centreline of bent yarn cross-section is 2.4mm. It is observed that a real warp cross-section shape for this preform in the flat region can be better approximated with a power ellipse than an ellipse, thus validation of warp yarn bending is based on the cross-section function for a power ellipse (m=0.4) with yarn height and width measured from the unbent region in the web, where Eq.(3.4) can be expressed as:

$$C(t)_x = \frac{W_{warp}}{2}\cos(t) \qquad 0 \le t \le 2\pi$$

$$C(t)_y = \begin{cases} \frac{H_{warp}}{2}\sin^m(t) & 0 \le t \le \pi \\ -\frac{H_{warp}}{2}(-\sin(t))^m & \pi \le t \le 2\pi \end{cases} \tag{3.26}$$



(a) elliptical cross-section (b) power elliptical cross-section

Figure 3-11 Transformation of bent yarn cross-section shapes: dashed lines for original shapes and solid lines for bent shapes

Then the bent cross-sections for different radii of curvature can be plotted and compared with real yarns as shown in Figure 3-12. The modelled cross-section gives good agreement with realistic bent cross-section shapes.

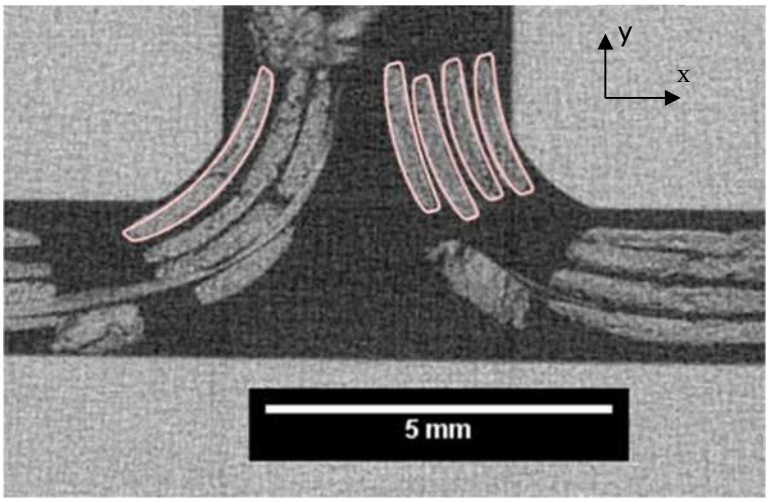


Figure 3-12 Model produced cross-section shapes in comparison with real yarns

3.5.3 Weft yarn cross-section flattening

Validation of cross-section flattening was carried out for yarns on three different layers in order to cover the full radius of curvature values which are the most essential parameters in yarn bending. The three layers selected are layer 1, 2 and 5 in section A-A of Figure 3-3. Weft yarn cross-section transition length l_0 is obtained from measurement for each layer, and radius of curvature of the reference fibre R_0 is derived based on calculated radius of curvature yarn centreline and flattened yarn height.

The total number of fibre layers along the yarn height direction before flattening n_f (Eq.(3.23)) is estimated based on yarn dimensions before flattening and filament count as well as the assumption that the cross-section was a rectangular shape with square fibre packing. Based on the flattened yarn height, $\bar{\alpha}$ can be obtained by solving a combination of Eq.(3.12), (3.21) and (3.22). Then the displacement of fibre out-of-plane migration along the yarn height if all the fibres are ideally migrated can be

obtained by solving a combination of Eq.(3.13), (3.19) and (3.20) as plotted in Figure 3-13. Yarn extension width can be calculated from Eq.(3.23) and (3.24), and all the parameters for the model are listed in Table 3-4.

Table 3-4 Parameters for the yarn flattening model

	l_0 (mm) 10 measurements	R_0 (mm)	$\bar{\alpha}$ (-)	d_{max} (mm)	n_f (-)	W_{weft}^{ext} (mm)	W_{weft}^{fla} (mm)
Yarn on layer 1	4.54(±0.18)	2.32	0.132	0.35	50	1.22	2.93
Yarn on layer 2	4.86(±0.16)	2.77	0.062	0.32	44	1.15	3.15
Yarn on layer 5	6.31(±0.14)	4.09	0.062	0.32	44	1.46	3.46

Furthermore, the measured yarn width and predicted yarn width for the flattened weft yarns are compared in Figure 3-14 and reasonable agreement is observed.

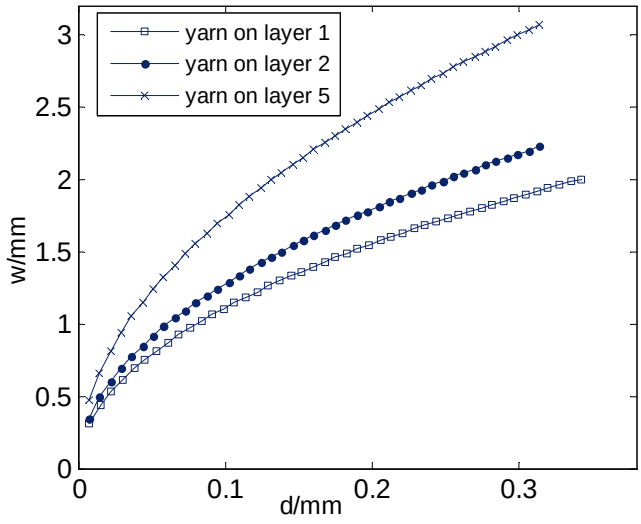


Figure 3-13 Relative displacement for fibre out-of-plane migration

Although the prediction accuracy is good, the model is semi-empirical based on the input parameters of flattened yarn height and cross-section transition length. However it is interesting that all the flattened weft yarns with different radii of curvature have nearly the same height while the

length over which cross-section transitions occur seems to increase linearly with radius of curvature in bending, both of which merit further investigation.

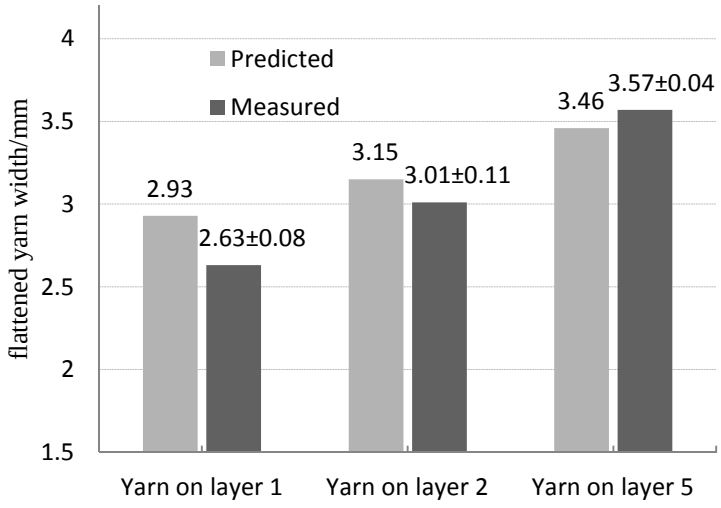


Figure 3-14 Comparison of measured and predicted yarn width for weft yarns

3.6 Conclusions

To characterise the relationship between the fibre architecture and composite mechanical performance, a numerical simulation requires a realistic geometric model as input. In this chapter, three geometric features, yarn shifting, cross-section bending and flattening, caused by the bifurcation of a 3D flat woven preform for composite T-joints were identified by μCT analysis and approximated analytically. A simple model based on rigid body movement was used to approximate warp yarn shifting but the experimentally observed trend does not always agree closely with the model. The model would benefit from considering the influence of binder yarns on movement of warp yarns as well as yarn sliding induced by the weaving process but this would complicate the model significantly. Yarn cross-section bending was modelled by a transformation of the existing parameterized description of cross-section shape instead of proposing a new

shape function, and good agreement was obtained when compared with μCT results. Lastly, weft yarn flattening was described in detail and a semi-empirical model was developed to predict the flattened yarn width and satisfactory agreement with experiments was observed. However, it is worthwhile to further study the preform compaction behaviour and form a fully predictive model for yarn flattening. These proposed analytical models would be helpful in developing the geometric model of the 3D woven T-joint (Type 1) for the subsequent FE modelling in the absence of μCT analysis and can be implemented in TexGen for automated generation of T-joint geometries.

Chapter 4 Modelling approach for composite delamination based on meso-scale voxel method

4.1 Introduction

Delamination was found to be a typical failure mode in the mechanical testing of composite T-joints in Chapter 2, and hence it has to been accounted for in the modelling framework, in order to accurately model weave architectures of 3D woven composite T-joints and the resulting mechanical behaviour. For modelling of the tested 3D woven T-joint specimens, conformal meshing at meso-scale is extremely difficult to achieve due to the complex 3D fibre architecture. Using voxel meshing in modelling of such advanced composites is a compromise between the accuracy of the results that could be decreased by the voxel discretisation, and the ease of mesh generation where conformal meshing is not readily available. A surface-based cohesive zone model (CZM) has been employed increasingly to model composite delamination, however, research to date has not justified the use of CZM to model composite delamination in conjunction with meso-scale voxels.

In this chapter, the feasibility of using a voxel mesh in CZM is investigated based on a reduced composite T-joint structure reinforced by unidirectional non-crimp fabric (NCF), before proceeding with computationally intensive studies on the 3D woven T-joints. This reduced structure makes conformal meshing available and can also represent the problem of the step-like interface between the matrix and yarns due to voxel discretisation at the junction of the T-joint. The limitations of using voxel meshing in CZM are evaluated both analytically and numerically in terms of prediction accuracy

in structural stiffness and strength, in comparison with conformal meshing. Finally, recommendations on using voxel meshing in CZM are given.

4.2 Literature review

For composites with complex fibre architectures, such as 3D weaves, in most cases meso-scale unit cell modelling has to be adopted in FE analysis, as the anisotropic properties of these materials cannot be readily homogenised. The presence of constituent interfaces in the meso-scale models should be considered for modelling damage at yarn/matrix interface. Thus to model a composite structure with complexity in fibre architecture, the first step is to build the reinforcement and matrix geometry and then meshing is performed based on the geometry [58]. For composites with complex fibre architecture or geometric features like curvature or holes, it is not always easy to obtain a 3D mesh where element connectivity is required as well as accurately representing the constituent domains, which is thought to be beyond the capability of current meshing software [59]. In order to achieve a feasible FE mesh for subsequent meso-scale FE analysis of composites, geometry simplification or adaptation is usually employed although such techniques could either lead to a deviation from the predicted performance or require more effort to develop an algorithm. A common method to simplify the geometry is to artificially decrease the size of yarn cross-sections in order to eliminate extremely thin layers of matrix in-between adjacent yarns [58, 60], but this would correspondingly lead to the usage of a higher intra-yarn fibre volume fraction in the model, as well as an unrealistic constituent interface.

Voxel meshing is an alternative to the aforementioned conformal meshing, along with some emerging methods without requiring a continuous mesh for the constituent domains such as the Independent Mesh Method [59] or Domain Superposition Technique [61]. Benefiting from ideas from image processing, voxel-based FE models are increasingly used for analysis of

composite structures due to their significant advantage in the ease of meshing. The idea behind the voxel-based method is to mesh the whole geometry with equal-sized volume pixels and assign each pixel a property of yarn, matrix or a mixture between them based on the position of the pixel regarding the constituent geometry. The voxel-based FE method has proved to be effective in stress/strain analysis of composite structures but it might lack accuracy in failure analysis due to its step-like constituent interface [62], although some good agreements with experiment results were found based on a number of proposed models for composite performance predictions [38, 63, 64].

A comparison between voxel and conformal models of a multi-layer plain woven composite was undertaken by Doitrand and colleagues [62]. They found that the voxel method shows a good agreement with the conformal method in terms of elastic properties but spurious predictions on damage initiation caused by stress concentrations were also observed. However, mesh dependency was found by Ernst et al. [64] when using a conformal mesh to analyse the failure of textile composites with a fracture energy approach. Irregular elements defined as not having an aspect ratio close to one would usually be generated near the constituent interface by automated meshing if the interface is not formed of flat surfaces, which were found to be “crack stoppers” in the simulation when compared with results from a manually altered regular mesh with element aspect ratio close to one. However, more irregular elements are normally to be expected at the yarn/matrix interface for textile composites as they have more complex fibre architecture. Instead, a voxel mesh was adopted by the authors [64] as the specific mesh dependency problem vanished with this method, and also good agreement in stiffness and progressive damage was observed between simulations and experimental results for a thick NCF specimen subjected to a three-point bending load [64].

Apparently, the voxel method has both its advantages and disadvantages

and sometimes a compromise of using a voxel mesh has to be taken for modelling of composites with complex fibre architecture when a high quality conformal mesh is not readily available based on state-of-art meshing techniques. The step-like interface resulting from the use of voxels, which would lead to stress field jumps on adjacent material phases or stress concentrations, is thought to be the primary source of errors in analysis, and therefore some effective methods for ameliorating this impact were proposed. A stress averaging technique is one way to alleviate the stress prediction error for voxel meshes as verified on simple fibre architecture models, whose performance relies on the used stress averaging algorithm [65]. It is still open to debate whether this technique works for composites with complex fibre architecture as Doitrand et al. found that it was an insufficient solution for a multi-layer plain woven composite [62], based on their averaging algorithm. Another promising alternative to overcome the limitation of the voxel method is local mesh size refinement [66] or mesh geometric smoothing [67, 68] on the elements in the vicinity of constituent interfaces. This method tends to transform the step-like voxel mesh into a conformal mesh at the interface but depends on a sophisticated algorithm to avoid a distorted mesh being generated at the constituent boundaries.

Delamination was found to be a typical failure mode in the mechanical tests of composite T-joints and CZM based on a conformal mesh has been proven to be an efficient way to model delamination in FE analysis [20]. For composites with complex reinforcement geometry, meso-scale models have to be employed to distinguish constituent interfaces as they cannot be represented by a combination of homogenised lamina layers. However, it is open to question whether it is feasible to use surface-based CZM with a voxel method to model delamination as the interface elements will be generated on the step-like constituent boundaries. Zhang et al. used a voxel mesh to perform damage simulation of a single-layer triaxially braided composite with surface-based cohesive elements accounting for tow-tow

delamination and good correlation with experimental results was obtained [63]. In contrast, some authors claimed that it is not possible to use a voxel mesh in CZM, as generation of interface elements with a step-like geometry would be problematic [65], or that interface damage initiation and fracture energy cannot be computed on a step-like interface [69]. This chapter aims to assess the usage of surface-based voxel CZM to model mixed-mode delamination for a T-joint composite structure subjected to tensile pull-off loading. The accuracy of delamination analysis by voxel-based CZM will be compared with a conformal model, and recommendations will be given for successful delamination analysis with CZM.

4.3 Geometry, material properties and boundary conditions

4.3.1 Geometry and meshing

Composite T-joints can be made from laminates, laminates with Z-pinning or textiles for the aerospace sector [20, 22, 30]. In many cases, a 90° bent stack of unidirectional lamina is the basic element in the fibre architecture, onto which Z-pins or binders may be added. Therefore, the geometry of a simple laminated composite T-joint was constructed by TexGen (Figure 4-1), with each half comprising of four layers of bent uniaxial non-crimp fabric without any fixation material, to study the effects of meshing technique on the mechanical performance of the structure with CZM.

The reasons for selecting such a geometry are as follows: 1) This structure has a typical failure mode of delamination at the yarn/matrix interface under a number of loading cases, and CZM based on conformal meshing has already been proven to be an efficient way to model the delamination [20, 70]. 2) This geometry is a reduced model for the tested 3D woven composite T-joints by removing the orthogonal and binder yarns. 3) Meshing a composite with curved layer paths could expose the problem of the step-like mesh interface between yarns and matrix due to voxel discretisation,

which meets the objective of this study to examine the feasibility of using a voxel mesh in CZM.

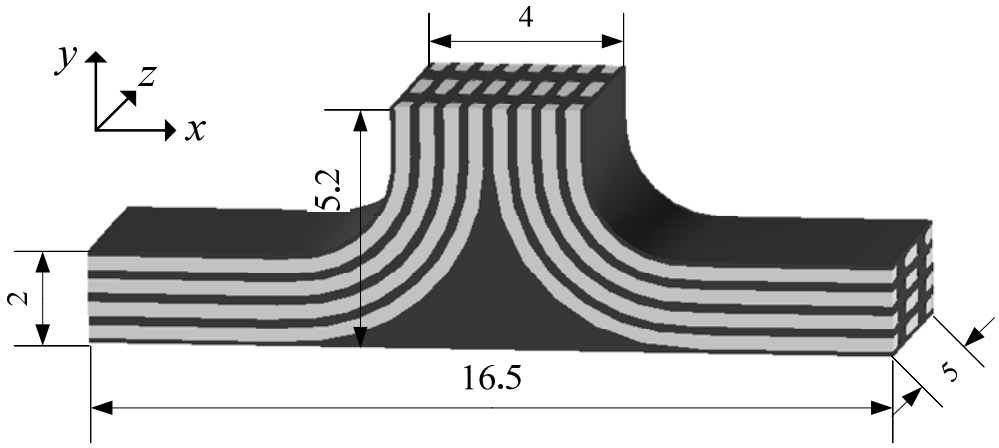


Figure 4-1 Baseline geometry of the T-joint composite (unit: mm)

A voxel mesh of this T-joint composite is directly exported from TexGen along with the yarn element orientation database. Each of the voxel elements is either assigned to the matrix or a yarn set based on the position of voxel element centroid. A hexahedron-based conformal is generated by Hypermesh based on the geometry imported from TexGen. Hexahedral mesh generation accounts for most of the model development time due to the geometric complexity imposed by features of the T-joint. Although tetrahedral meshing is relatively easier to achieve, it was not used in this work as it is not always recommended in FE analysis. For the FE analysis, an 8-node linear brick element with reduced integration (Abaqus notation: C3D8R) is assigned to the voxel and conformal mesh. Both of the meso-scale models are presented in Figure 4-2. By comparing between the two types of mesh as shown in Figure 4-3, it is found that the inaccuracies of voxel mesh discretisation for the solid geometry lie in the following two aspects: 1) generating a step-like yarn/matrix interface due to the curvature of the yarn path; 2) loss of geometric feature of the yarn cross-sectional shape when it is not rectangular.

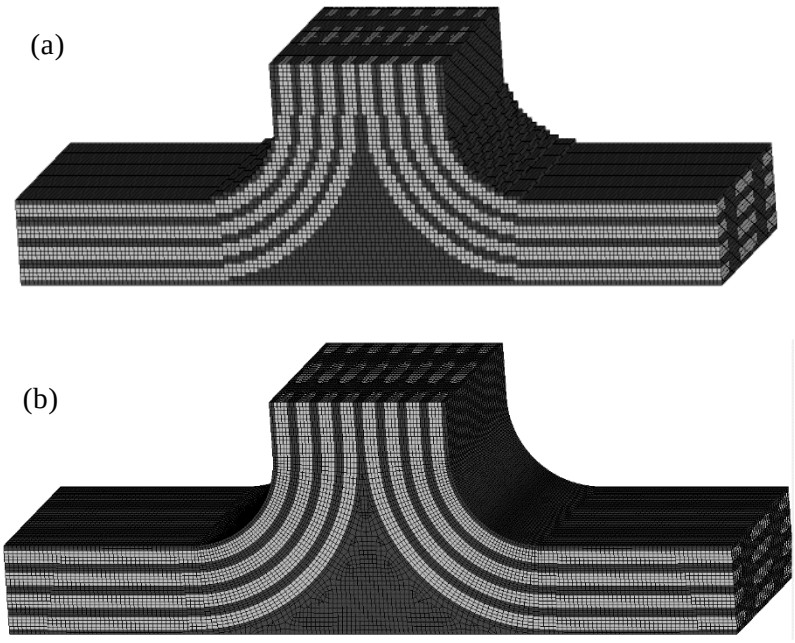


Figure 4-2 Meso-scale models of the T-joint composite: (a) voxel mesh (element length: 0.1 mm; number of elements: 238,750); (b) conformal mesh (element length: approx. 0.08 mm; number of elements: 539,784)

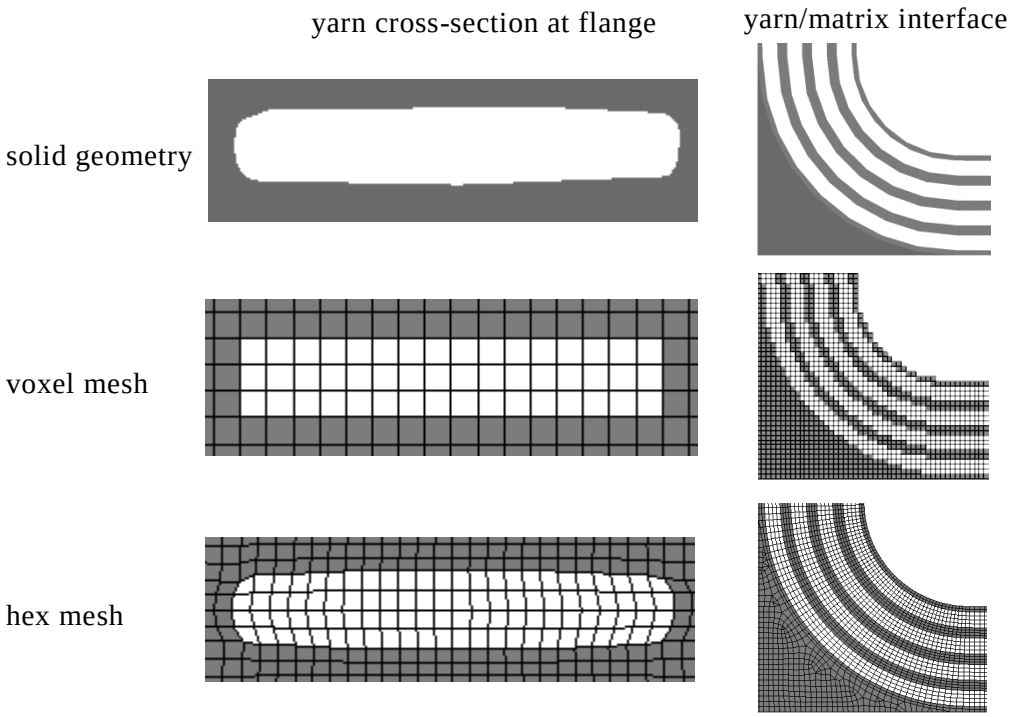


Figure 4-3 Mesh representations of the solid geometry of a half composite T-joint

4.3.2 Constituent material properties

The composite T-joint is assumed to be made of aerospace-grade carbon fibre, Hexcel IM7 12K, and epoxy resin, Gurit Prime 20LV, as used in the tested composite T-joints. The transversely isotropic properties of impregnated yarns are calculated based on the Chamis model [71], assuming an intra-yarn fibre volume fraction of 63%. The elastic properties of the constituents are listed in Table 4-1. Note that this study is mainly for the purpose of analysing the effects of voxel meshing on the CZM method and thus the assumed constituent properties are only required to be in reasonable range for the composite. More details about yarn properties in textile composites are given Section 5.5.2.

Table 4-1 Elastic properties for constituent materials used in the FE models

IM7 Carbon Yarn		Prime 20LV Epoxy resin	
E_1 (GPa)	174.4	E (GPa)	3.5
E_2=E_3 (GPa)	8.9	v (-)	0.35
v_{12}=v_{13} (-)	0.3		
G_{12}= G_{13} (GPa)	4.2		
G_{23} (GPa)	3.0		

4.3.3 Boundary conditions

Numerical testing was performed on the voxel and conformal meso-scale CZM models, with a displacement-controlled tensile quasi-static pull-off load, prescribed on the top surface of the structure while both of the boundary surfaces at the end of the flange are constrained in all translational degrees of freedom. An illustration for the boundary conditions (BCs) is given in Section 5.4, which is to simulate the loading condition on the T-joint specimens tested in Chapter 2. Before analysing the CZM models, a mesh convergence study, which is simplified as an elastic analysis under the condition of perfect bonding between matrix and yarn elements, was

performed with Abaqus Explicit. The mechanical testing of 3D woven T-joints in Chapter 2 demonstrated both material and interface damage in the specimens, and therefore Abaqus Explicit was chosen to solve this non-linear analysis as it is difficult to deduce the Jacobian matrix in the subroutine required by Abaqus Standard. As strain rate effect was not considered in the materials, mass scaling was not used, and the loading speed was chosen as 1 mm/ms to ensure the inertial effect is negligible. The global load-displacement responses for both conformal and voxel models, plotted as the reaction force of the loading surface against the loading displacement, for a range of element lengths are shown in Figure 4-4. Furthermore, it was found that the use of a voxel mesh with an element length of 0.1 mm leads to a maximum deviation of 2% in the load at 0.4 mm displacement against the conformal mesh (0.08 mm), as compared in Figure 4-5, which will be adopted as baseline element lengths for the following voxel-based CZM analysis in order to avoid high computation cost from an excessively fine mesh.

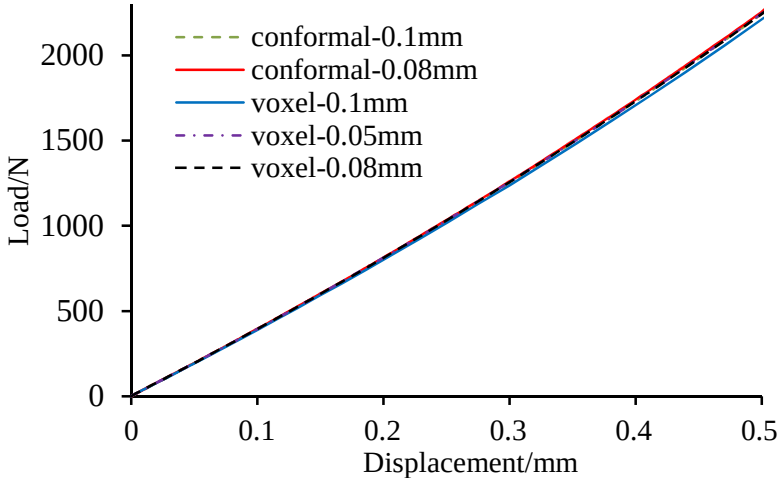


Figure 4-4 Load-displacement responses for perfectly bonded models with different mesh densities

In addition, the stress contours of the voxel model (0.1mm) and conformal model (0.08mm) at 0.33 mm displacement are compared in Figure 4-6 (S11) and Figure 4-7 (S22) to show that the voxel model is fine enough for failure modelling.

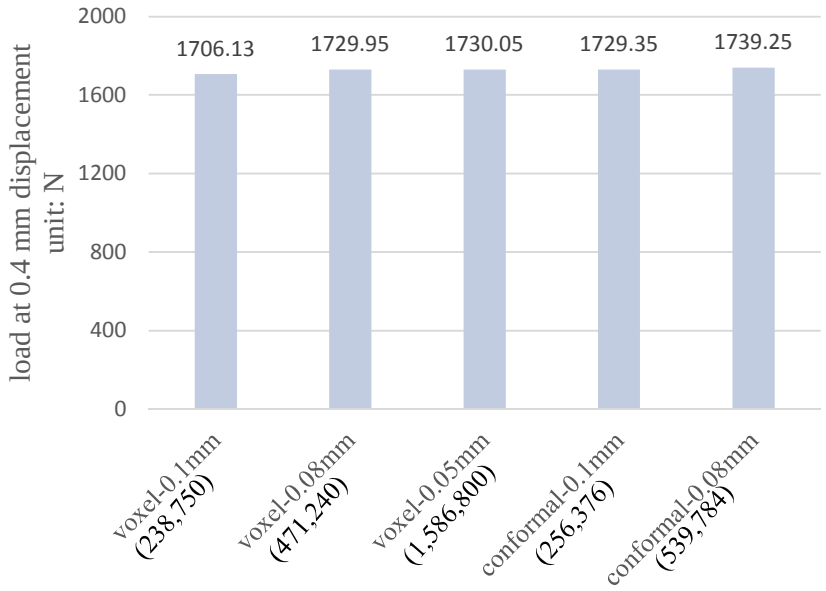


Figure 4-5 Comparison of load at 0.4 mm displacement for perfectly bonded models with different mesh densities (the number in bracket is the number of element for each model)

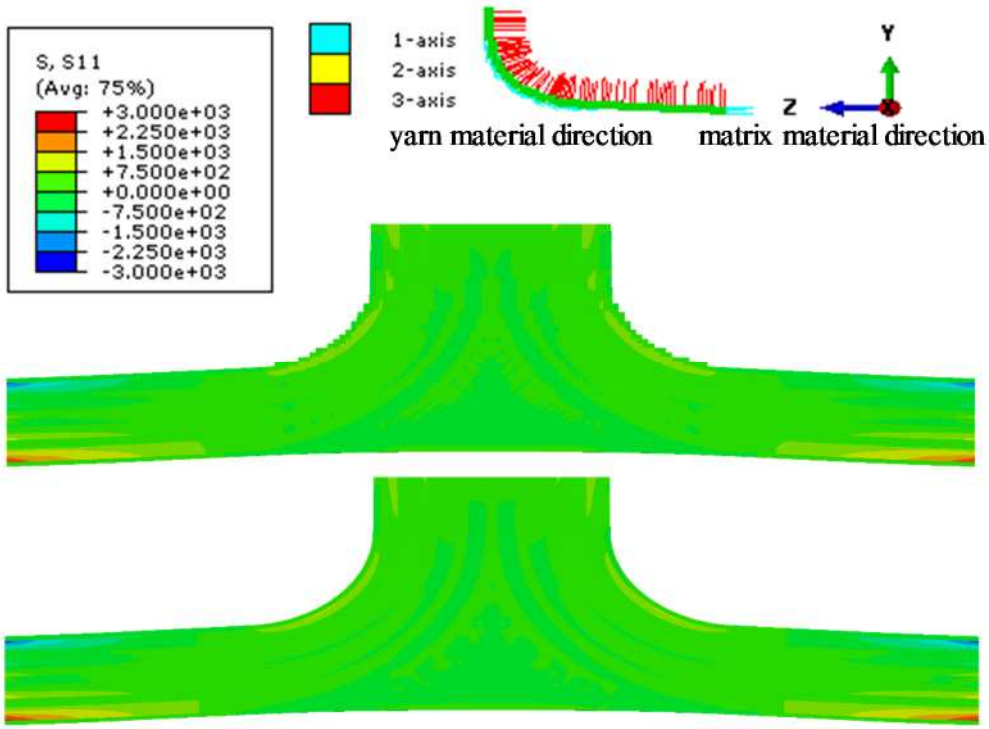


Figure 4-6 Comparison of stress state (stress component S11) at 0.33 mm displacement for perfectly bonded voxel (top) and conformal (bottom) models

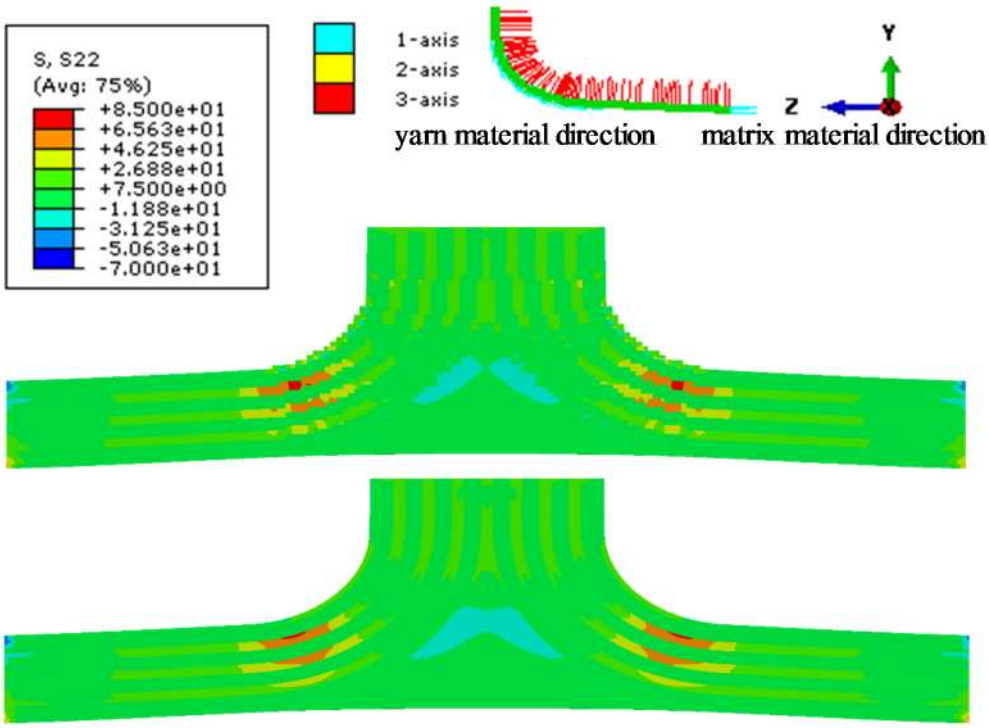


Figure 4-7 Comparison of stress state (stress component S22) at 0.33 mm displacement for perfectly bonded voxel (top) and conformal (bottom) models

4.4 Cohesive zone model

4.4.1 Interface formulation

The thickness of a constituent interface in composite materials is usually negligibly small. Hence surface-based cohesive modelling method is more suitable for modelling composite delamination than the finite-thickness cohesive element method which accounts for the interface thickness effect [72]. The surface-based cohesive behaviour is available in Abaqus with damage initiation and evolution models. It has been widely employed to model composite delamination [20, 70, 73]. As shown in Figure 4-8, the surface-based cohesive behaviour used here correlates cohesive tractions (stresses) in the normal, first shear and second shear directions (τ_n, τ_s and τ_t) with their corresponding separations (displacements) in the same direction (δ_n, δ_s and δ_t) through a bilinear constitutive law. The areas

under the tractions and their corresponding separations excluding the recoverable energy denote the energy release rate, G_n, G_s, and G_t, for each delamination mode [74].

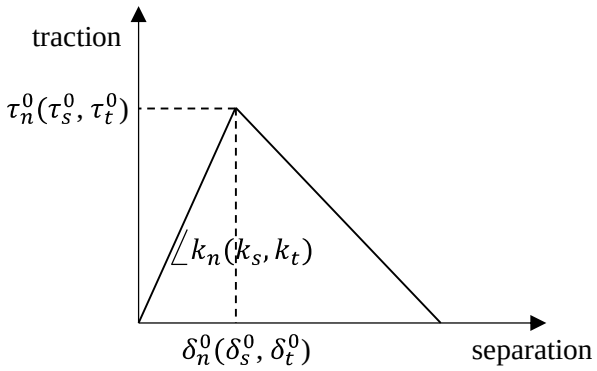


Figure 4-8 Bilinear traction-separation law [72]

As the T-joint composite is expected to have mixed-mode delamination under the tensile pull-off load, a quadratic stress criterion for damage onset is adopted and thus when the following expression reaches a value of one, damage is assumed to initiate:

$$\left\{\frac{\langle\tau_n\rangle}{\tau_n^0}\right\}^2+\left\{\frac{\langle\tau_s\rangle}{\tau_s^0}\right\}^2+\left\{\frac{\langle\tau_t\rangle}{\tau_t^0}\right\}^2=1 \tag{4.1}$$

where τ_n^0, τ_s^0 and τ_t^0 denote the initial failure stress in the normal, first shear and second shear directions for each of the single-mode delamination modes, respectively. The symbol <> is the MacAulay operator.

After damage initiation, there is a reduction in interface stiffness until total fracture of the interface, based on the mixed mode power law for damage evolution:

$$\left\{\frac{G_n}{G_n^C}\right\}^p+\left\{\frac{G_s}{G_s^C}\right\}^p+\left\{\frac{G_t}{G_t^C}\right\}^p=1 \tag{4.2}$$

where G_n^C, G_s^C and G_t^C are the critical energy release rate values in the normal, first shear and second shear directions under each of the single-

mode delamination modes, and *p* is the power in the criterion.

4.4.2 Interface stiffness

4.4.2.1 Conformal model interface

The slope (denoted by *k* in Figure 4-8) for the elastic stage of the bilinear constitutive law, which could affect the global compliance prior to crack development, is referred to as interface stiffness with subscript denoting its direction. As it is not considered as a material constant but a numerical value introduced by the CZM method, the selection of interface stiffness value was initially empirical or based on correlation with experimental results [75]. Minimising the spurious global compliance by not using a low interface stiffness is regarded as a necessity for a successful FE analysis with the CZM method. Meanwhile, there is no benefit in applying an excessively high interface stiffness as it could cause numerical instability and increase computation cost. Based on mode I delamination (in normal direction), an equation for estimating the minimum value of interface stiffness was proposed by Turon et al. [75], in order to ensure that the laminate's stiffness is not decreased by the presence of a cohesive surface between two identical plies (Appendix C). According to Turon et al. [75], when $\boldsymbol{A}$ (Appendix C) is greater than 50, the loss of stiffness due to the cohesive surface would be less than 2%, and also they found that the analytical solutions for the interface stiffness values were close to the those empirically proposed by previous authors. However, Turon's equation is only applicable for a laminate within which the two neighbouring plies hosting the cohesive surface have the same transverse modulus and thickness. Thus an extension to Turon's method is proposed here for estimating the interface stiffness, under model I delamination, for a cohesive surface presented between different materials. Shown in Figure 4-9 is a heterogeneous material comprised of two types of sub-materials (in this case yarn and bulk matrix) with a cohesive surface present between

them, which is subjected to a tensile loading stress σ in the through-thickness direction.

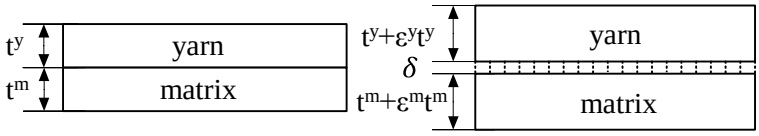


Figure 4-9 Effects of the cohesive surface on deformation for conformal mesh

According to the equilibrium condition,

$$\sigma = \tau = k\delta = E^{y}\varepsilon^{y} = E^{m}\varepsilon^{m} \tag{4.3}$$

where τ and δ are the traction and separation at the interface respectively, and k is the interface stiffness (note that the normal direction subscript n is omitted); t is the thickness of the sub-materials, ε is the strain in the through-the-thickness direction and E is the modulus in the through-the-thickness direction, with superscript y denoting the sub-material yarn and superscript m denoting the sub-material matrix respectively.

The effective strain of the composite in Figure 4-9 is:

$$\varepsilon_{eff} = \frac{\varepsilon^{y}t^{y} + \varepsilon^{m}t^{m} + \delta}{t^{y} + t^{m}} \tag{4.4}$$

Assuming there is no cohesive surface between yarn and matrix, i.e. a perfect-bonding condition, the effective strain of such a composite is:

$$\varepsilon'_{eff} = \frac{\varepsilon^{y}t^{y} + \varepsilon^{m}t^{m}}{t^{y} + t^{m}} \tag{4.5}$$

where ε'_{eff} is the effective strain for the idealised perfectly bonded composite.

Therefore Eq.(4.4) can be rewritten as:

$$\varepsilon_{eff} = \varepsilon'_{eff} + \frac{\delta}{t^{y} + t^{m}} \tag{4.6}$$

Since $\sigma = E_{eff}\varepsilon_{eff}$, the effective modulus of the composite in Figure 4-9 can be obtained as:

$$E_{eff} = \frac{\sigma}{\varepsilon_{eff}^{'} + \frac{\delta}{t^y + t^m}} = \frac{\sigma}{\frac{\sigma}{E_{eff}^{'}} + \frac{\sigma}{k(t^y + t^m)}} = \frac{E_{eff}^{'}}{1 + \frac{E_{eff}^{'}}{k(t^y + t^m)}} \tag{4.7}$$

where $E_{eff}^{'}$ is the effective modulus for the assumed perfectly bonded composite and it is defined as:

$$E_{eff}^{'} = \frac{\sigma}{\varepsilon_{eff}^{'}} = \frac{(t^y + t^m)E^y E^m}{t^y E^m + t^m E^y} \tag{4.8}$$

In Eq.(4.7), the effective modulus of the composite will not be affected by the presence of cohesive surface if $E_{eff}^{'} \ll k(t_1 + t_2)$, i.e. $E_{eff} \approx E_{eff}^{'}$.

Therefore the minimum interface stiffness is described as

$$k = \frac{\mathrm{A}E_{eff}^{'}}{t^y + t^m} \tag{4.9}$$

where ***A*** is a parameter much greater than 1.

NB: Eq.(4.7) and Eq.(4.9) are the same as Turon's equations (Appendix C) if sub-materials have the same modulus and thickness.

4.4.2.2 Voxel model interface

For textile composites discretised by a voxel mesh, a step-like yarn/matrix mesh interface is generated due to the curvature of the yarn path, as voxel elements are orthogonal in the mesh and could not rotate to accommodate an inclined material interface. Shown in Figure 4-10 is the voxel-discretised mesh interface for a 45°-inclined yarn/matrix material interface as can be observed at the junction of the studied T-joint (Figure 4-2), where *e* is the element length of the voxels. Suppose there is still a tensile loading stress σ in the through-thickness direction applied on the voxel-discretised composite (Figure 4-10), and all the properties are the same as above for

the conformal model, a different separation δ^v at the interface is expected for the voxel model, because the loading condition at the interface is changed from model I delamination to mixed-mode delamination.

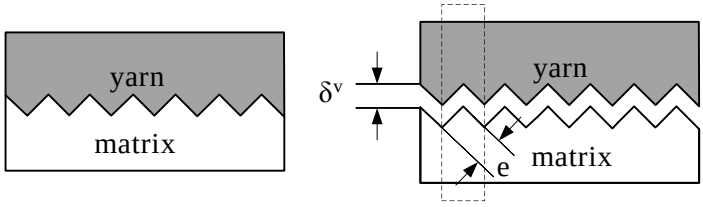


Figure 4-10 Effects of the cohesive surface on deformation for voxel mesh

Figure 4-11 shows a representative unit of the voxel-discretised composite as that marked in the dashed rectangle in Figure 4-10. As the separation vector at the interface can be decomposed into two components in the normal and shear directions (δ_n, δ_s) of the interface respectively, two tractions in the corresponding directions (τ_n, τ_s) therefore arise on each of the surfaces CD and ED in Figure 4-11 in line with the traction-separation law of the cohesive surface. Similarly, according to the equilibrium condition in the through-thickness direction, if there is a tensile stress σ applied on the surface AB, then:

$$\sigma\sqrt{2}e = 2\times(\tau_n e\cos 45^\circ + \tau_s e\cos 45^\circ) \tag{4.10}$$

where the composite is assumed to have unit length in the out-of-page direction; the length of ED and CD equals the element length d, while the length of AB is $\sqrt{2}e$.

The normal traction is equal to the shear traction as the same interface stiffness is usually used for the two directions. Thus, the tractions on surfaces CD and ED are:

$$\tau_n = \tau_s = \frac{1}{2}\sigma \tag{4.11}$$

If the interface stiffness for the voxel model is the same as that for the conformal model, the separation at the interface for the voxel model is:

$$\delta^v = \sqrt{\delta_n{}^2 + \delta_s{}^2} = \sqrt{2 \times (\frac{1/2\sigma}{k})^2} = \frac{\sqrt{2}\sigma}{2k} = \frac{\sqrt{2}}{2}\delta \qquad (4.12)$$

where k is the interface stiffness and δ is the resulting separation due to a tensile stress σ applied on the composite for the equivalent conformal model (Eq.(4.3)).

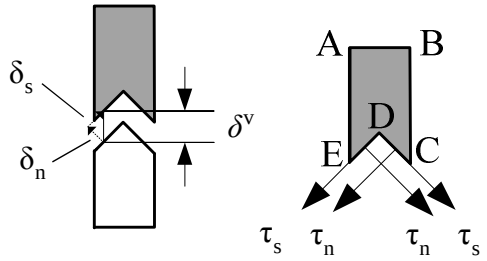


Figure 4-11 Free body diagram of the voxel model interface

The composite effective strain (defined in Eq.(4.6)) of the voxel model is less than that of the conformal model, as $\delta^v < \delta$, under the same loading stress σ. Hence an additional stiffness for the voxel model is introduced by the step-like mesh interface in the elastic loading stage, when compared with an equivalent conformal model. Apparently, the inherently stiffer behaviour of voxel models results from the altered stress state on the voxel mesh interface which leads to a smaller interface separation (Eq.(4.12)).

However, the separation at the interface is also affected by the interface stiffness. An identical effective modulus for the voxel model can be obtained, through scaling down the interface stiffness, to ensure a constant interface separation for the voxel and conformal models under the same loading:

$$k^v = \beta k \qquad (4.13)$$

where k^v is the interface stiffness for the voxel models; β is the scaling factor, In this elastic loading case, the scaling factor is $\beta = \sqrt{2}/2 \approx 0.7$.

It should be noted that the above analysis is only applicable for mode I

delamination as this is the critical case in T-joint loading. In terms of pure model II loading on the above conformal (Figure 4-9) and voxel interfaces (Figure 4-10), an ineligible error is expected from the step-like voxel interface.

4.4.2.3 Effects of interface damage on the stiffness

When the loading stress σ reaches the initial failure stress in the normal direction τ_n^0, the conformal model would initiate damage at the interface, according to the damage imitation law of the interface (Eq.(4.1)):

$$\left\{\frac{\tau_n^0}{\tau_n^0}\right\}^2 = 1 \tag{4.14}$$

As discussed above, the loading condition on the voxel model interface is altered from model I delamination to mixed-mode delamination (Figure 4-11) due to its step-like mesh interface, therefore the interface of the voxel model is still intact when σ reaches τ_n^0 by evaluating the interface stress state (Eq.(4.11)) through the damage initiation criterion:

$$\left\{\frac{\frac{1}{2}\tau_n^0}{\tau_n^0}\right\}^2 + \left\{\frac{\frac{1}{2}\tau_n^0}{\tau_s^0}\right\}^2 < 1 \tag{4.15}$$

where τ_s^0 is usually equal to or greater than τ_n^0.

It is noted that a conformal model would initiate interface damage and enter the interface stiffness degradation stage of the bilinear law earlier than the voxel model, thus there will be a further reduction in the effective modulus of the composite (Eq.(4.7)) for the conformal model with the decrease of its interface stiffness *k* caused by interface damage, after the loading stress reaches the critical value. For the voxel model, the interface is evaluated as intact at the same loading stage and therefore the interface stiffness remains the elastic value. As a result, the voxel model could not capture the above

reduction in the effective modulus of the composite in contrast to the conformal model, which would further contribute to the additional stiffness of the voxel model. This contribution to the additional stiffness of the voxel model could be removed phenomenologically by artificially reducing the interface stiffness of the voxel model, i.e. further decreasing the scaling factor β in Eq.(4.13), to match the degraded interface stiffness of the conformal model. However, it is difficult to quantify analytically how much reduction is necessary in the case of interface damage, but this will be evaluated numerically in the following section.

4.5 Results and discussion

4.5.1 Baseline predictions

In this study, the meso-scale cohesive models are simplified only to have interface damage and thus linear elastic behaviour is used for the constituent materials (Table 4-1). The interface properties used in the cohesive models are listed in Table 4-2, which are comparable with those used in previous studies for a carbon/epoxy interface [76, 77]. By substituting the material properties for the yarn and matrix into Eq.(4.9), the minimum interface stiffness for this case derived from the analytical solution is 5.5×10^5 MPa/mm, against which a numerical minimum interface stiffness found by parametric study will be compared in Section 4.5.3.

Table 4-2 Interface properties used in the cohesive models (For baseline prediction)

$k_n = k_s = k_t$	$\tau_n^0 = \tau_s^0 = \tau_t^0$	G_n^C	G_s^C	G_t^C	p
10^6 MPa/mm	60 MPa	0.2 mJ/mm^2	0.84 mJ/mm^2	0.84 mJ/mm^2	2

Figure 4-12 shows the load-displacement responses for the meso-scale cohesive models, based on the interface properties listed in Table 4-2. Both of the voxel and conformal models predict intensive interfacial failure, when the applied force on the T-joint composite reaches approximately

750N. The final failure is mostly determined by the calculation of critical energy release rate, which appears not to be affected by the voxel interface. The composite structure progressively loses its structural integrity above 750N due to delamination. However, the voxel model exhibits a higher stiffness than the conformal model during the loading step, even though the same interface properties (Table 4-2) were used. Moreover, when comparing the interface damage parameter for the two models, as shown in Figure 4-13, the interface of the conformal model tends to initiate damage earlier than the voxel model, which is consistent with the analysis in Section 4.4.2.3 (for validation of Eq.(4.15)). The damage at the interface of the voxel model propagates much faster after initiation than the conformal model, and consequently an earlier loss of load-bearing capability of the voxel model is reflected in the load-displacement responses in Figure 4-12.

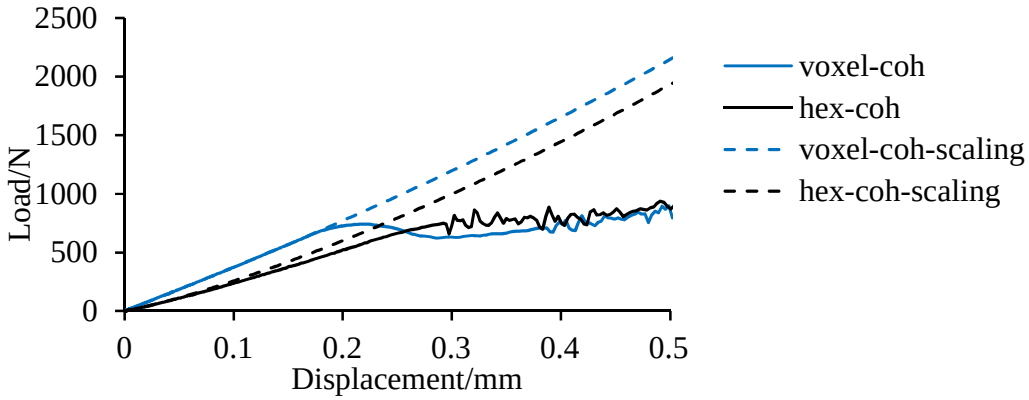


Figure 4-12 Load-displacement responses for the cohesive models

In order to rule out the influence from interface damage on stiffness reduction, the interface strength and critical energy release rate for each delamination mode were scaled up by a factor of 10 to delay interface damage. The load-displacement responses for the two models with scaled up interface properties are plotted as dashed lines in Figure 4-12.

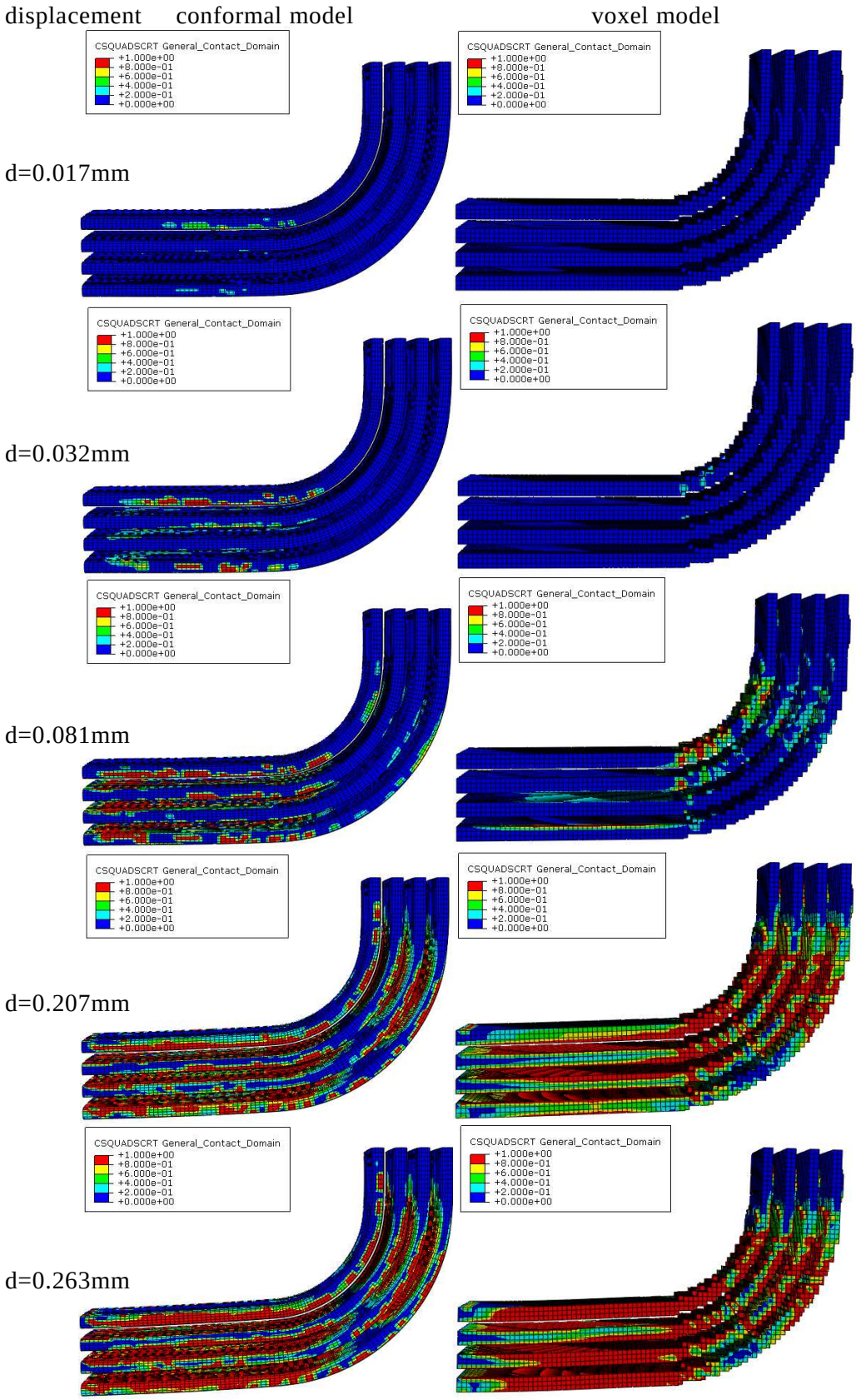


Figure 4-13 Progressive interface damage in the conformal and voxel models (CSQUADSCRT in the legend denotes quadratic stress-based damage initiation criterion for cohesive surfaces (Eq.(4.1))

Apparently there is still a difference in structural stiffness between the voxel and conformal models, which agrees with the analysis in Section 4.4.2.2, caused by the altered stress state at the step-like voxel interface. Meanwhile, the stiffness degradation resulting from interface damage can be observed by comparing the solid and dashed lines in Figure 4-12 for each model, in which the conformal model exhibits a more compliant behaviour than the voxel model due to earlier interface damage as shown in Figure 4-13. As the conformal model could represent the geometry and interface more accurately than the voxel model, it is therefore considered to have higher accuracy. In addition, the accuracy of CZM depends on having a sufficient number of elements within the cohesive zone [77]. A finer voxel model (element length 0.05 mm) was further analysed based on the same conditions. No difference in stiffness was found with the previous voxel model (element length 0.1 mm). Based on the FE analysis of the meso-scale cohesive models for the T-joint composite, it is found that the voxel mesh model could be used in CZM. It is capable of capturing the peak failure load in the mixed-mode delamination analysis, but it would show a higher structural stiffness which is an inherent problem due to its inaccurate discretisation at the interface. This limitation in stiffness over-estimation may not be critical, particularly at the conceptual design stage.

4.5.2 Effects of interface strength

The values of interface strength for different delamination modes used in the CZM were justified by previous authors [77] with regard to the numerical cohesive zone length. Typically, the cohesive zone length for an aerospace carbon/epoxy laminate is approximately 0.3 to 1 mm [78]. To minimise mesh-dependency, appropriately reducing the interface strength in CZM was found necessary when a large structure is coarsely meshed, for example element length is greater than 1 mm (compared to the above typical cohesive zone length), because a longer cohesive zone length resulting from lower interface strength could incorporate more interface elements to

capture the cohesive zone stress distribution [73, 75, 77]. Inaccurate results were also observed by applying excessively low interface strength due to earlier damage initiation at the interface leading to overly compliant structural behaviour [77]. The effects of varying interface strength (the other properties remain unchanged as listed in Table 4-2) for both conformal (Figure 4-14) and voxel (Figure 4-15) cohesive models in this work are consistent with previous research [77].

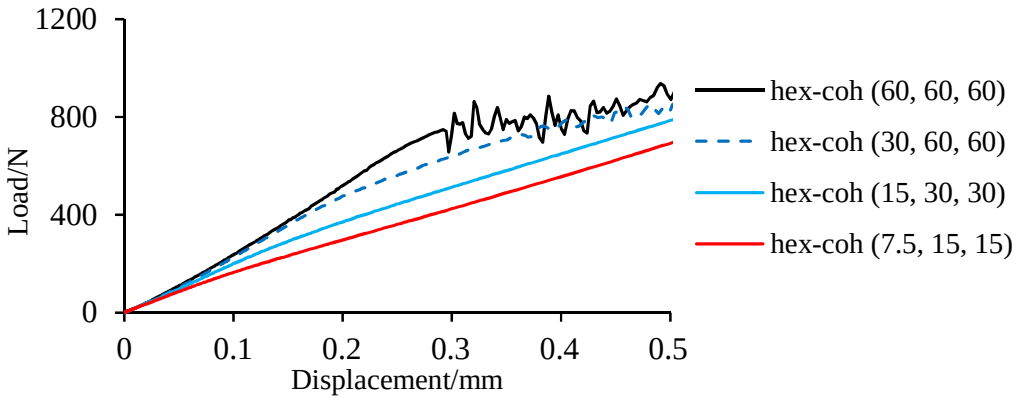


Figure 4-14 Load-displacement responses for the conformal model with different interface strength for τ_n, τ_s and τ_t (units: MPa)

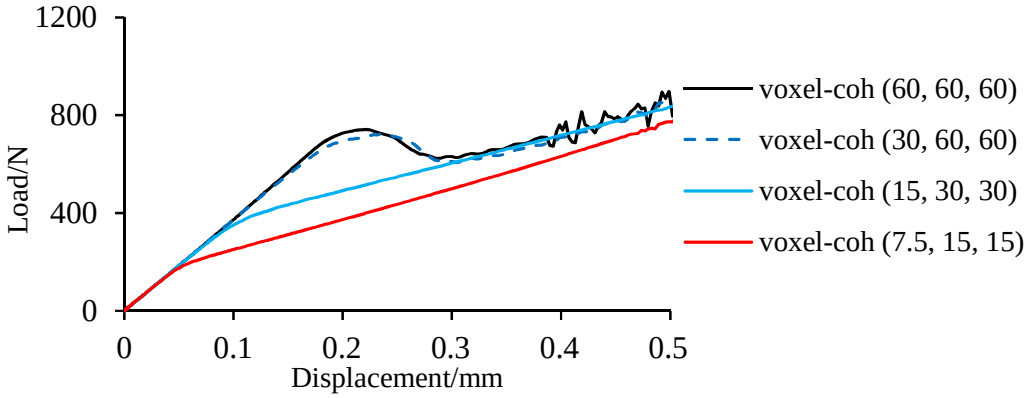


Figure 4-15 Load-displacement responses for the voxel model with different interface strength for τ_n, τ_s and τ_t (units: MPa)

The realistic interface strength between yarn and matrix in a carbon/epoxy composite is supposed to be not greater than the tensile strength of the

matrix, i.e. 60 MPa for modes I and II. With small variations in the interface strength around the realistic values, there is no significant change in the global load-displacement response. However, consistent results for the mode I value below 15 MPa show a severe stiffness degradation even at the early stage of loading.

4.5.3 Effects of interface stiffness

Figure 4-16 and Figure 4-17 show the effects of varying interface stiffness (the other properties remain unchanged as listed in Table 4-2) for the conformal and voxel models on load-displacement responses of the T-joint composite. It is validated that there is a converged value for the stiffness which means increasing the order of magnitude of the interface stiffness will not lead to any change in the load-displacement response. For both the conformal and voxel models, the stiffness converges when the interface stiffness is greater than 10^5 MPa/mm, which is in the same order of magnitude as that predicted by the analytical method (5.5×10^5 MPa/mm through Eq.(4.9)). In addition, applying an excessively high value of interface stiffness in the FE analysis is found to significantly increase the computation cost, e.g. stable time increment for the analysis would decrease from 10^{-9} to 10^{-12} s, if the interface stiffness is increased from 10^6 to 10^{10} MPa/mm. It is believed that if the interface stiffness of both voxel and conformal cohesive models are increased to the limit of infinity then they should both theoretically converge on the models with no cohesive elements (perfectly bonded). However, these models converge on different values and this is likely to be caused by the cohesive element formulation within Abaqus as it may not allow using an extremely high interface stiffness in FE analysis due to high computation cost and numerical stability issue. Meantime, the voxel cohesive model converged more closely to the perfectly bonded model due to its additional stiffness. Further work to examine the Abaqus formulation on cohesive surface in terms of the difference between cohesive and perfectly bonded models is recommended.

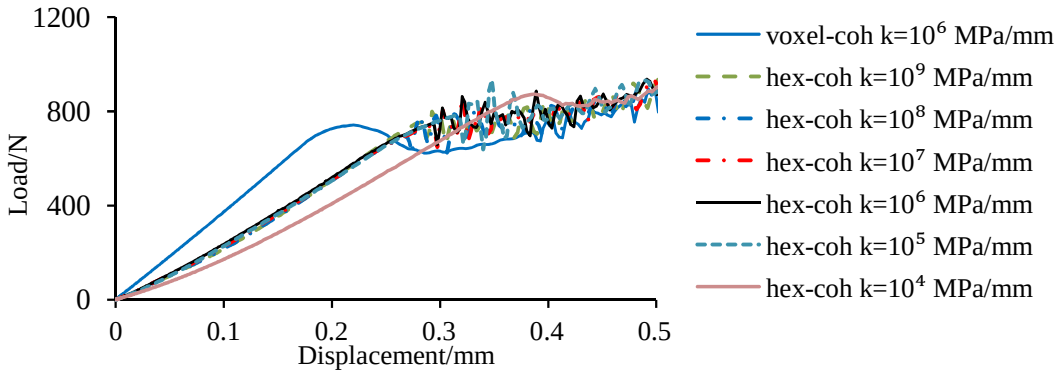


Figure 4-16 Load-displacement responses for the conformal model with different interface stiffness: from 10^4 MPa/mm to 10^9 MPa/mm; response converged at k=10^5 MPa/mm

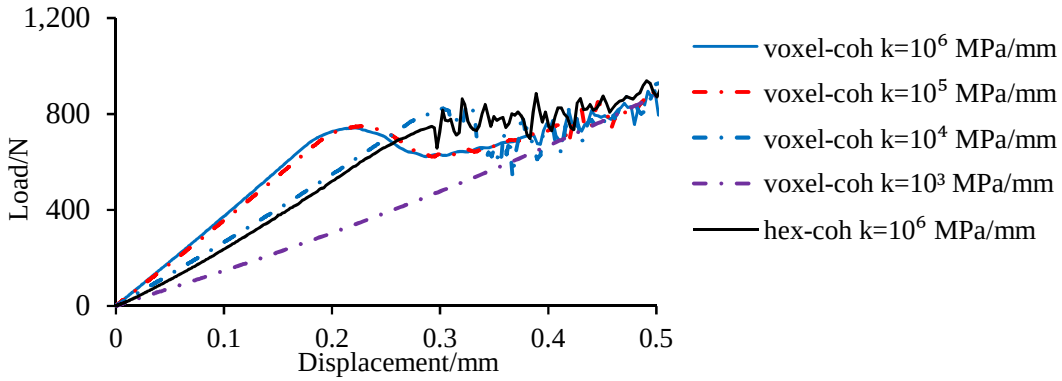


Figure 4-17 Load-displacement responses for the voxel model with different interface stiffness: from 10^3 MPa/mm to 10^6 MPa/mm

Using an interface stiffness less than the converged value will introduce a spurious compliance on the structure before crack propagation for both the voxel and conformal models. When the interface stiffness was reduced by one order of magnitude, i.e. β in Eq.(4.13) is further reduced to 0.1, from the converged magnitude (10^5 MPa/mm), the voxel model showed a similar load-displacement response to the conformal model. This level of reduction in the interface stiffness for the voxel model comprised of the component for reducing the additional stiffness at the elastic stage (Eq.(4.13)) and that for reducing the stiffer behaviour caused by delayed damage initiation (Eq.(4.15)). Interface stiffness scaling for the voxel-based cohesive models is found to be a possible way to improve the accuracy of the voxel mesh for

delamination modelling, and this finding will be validated against experimental data in the next chapter.

4.6 Conclusions

The feasibility of using a voxel mesh in CZM to model composite delamination was investigated in this chapter based on a reduced model for the tested 3D woven composite T-joint, before proceeding with computationally intensive studies on the 3D woven T-joint models. The reduced T-joint composite which is only reinforced by non-crimp fabric can represent the problem of the step-like interface between the matrix and yarns in the 3D woven T-joint models whilst enabling conformal meshing of the geometry.

The interface stiffness is a numerical value introduced by CZM rather than a material constant, and its selection was initially empirical or based on correlation with experimental results. Pioneered by a previous study [75], an analytical expression based on a conformal interface for estimating the minimum interface stiffness applicable in textile composites was developed, which avoids empirical analysis. Then the effect of voxel mesh interface on structural stiffness was analysed in terms of elastic loading and damage initiation according to the interface formulation, compared with the conformal interface. It is found that voxel discretisation would change the stress state at the interface and consequently the voxel model would show a stiffer behaviour than the conformal model. The additional stiffness for the voxel model resulting from the elastic loading stage was quantified but it is difficult to evaluate the contribution from premature interface damage analytically. It should be noted that presented analysis is only applicable for mode I delamination as this is the critical case in T-joint loading. In terms of pure model II loading on the above conformal and voxel interfaces, an ineligible error is expected from the step-like voxel interface.

Numerical investigation was also performed to evaluate the difference between conformal and voxel models based on the reduced T-joint structure. Compared with the results from the equivalent conformal model, the voxel model was able to capture the peak failure load in the mixed-mode delamination analysis but overestimated the structural stiffness, which agrees with the above analysis. Benefiting from the approach for estimating the minimum/converged interface stiffness, a solution for interface stiffness scaling based on the converged value that enables the voxel model to have comparable accuracy with conformal model was proposed. Through a parametric study on interface stiffness, the level of reduction in the interface stiffness (reducing β to 0.1 in Eq.(4.13)) of the voxel model to compensate the overestimation in structural stiffness was found, which will be validated against experimental data in the next chapter.

Chapter 5 Finite element modelling of 3D woven composite T-joints under quasi-static tensile pull-off loading

5.1 Introduction

In Chapter 2, it was found that limited weave variation in 3D woven reinforcements could lead to a significant difference in mechanical performance, e.g. a more than 100% difference in the ultimate failure load, through the quasi-static tensile pull-off tests on two types of 3D woven T-joint. This implies that the design of 3D woven composites is complex, with small changes to geometric features, potentially resulting in a significant change to the structural performance.

Currently, the lack of analysis techniques that are able to accurately predict the resulting structural performance for 3D weave architectures holds back the wide applications of 3D woven composites. Besides, using the “make and test” strategy to determine the optimum reinforcement design for a 3D woven composite part is far more intensive than that for a laminate. Some encouraging predictive models, have been reported on modelling the mechanical behaviour of 3D woven composites or more generally 3D textile composites, but generally these are based on flat samples at the unit cell level. Moreover, a predictive model should also remain valid and require no change in model parameter inputs when the weave architecture is changed, which was not demonstrated for most of the published modelling methods.

The focus of this chapter is to develop a meso-scale predictive modelling framework that relates reinforcement architectures of 3D woven composite T-joints with the resulting mechanical behaviour subjected to quasi-static tensile

pull-off loading as described in Chapter 2. The meso-scale T-joint model that reflects the feature of the reinforcement architecture is built based on the geometric modelling strategy introduced in Section 5.3, and hence can be easily extended to the other types of T-joints with weave variations at the junction. Details including boundary conditions and constitutive relations for the homogenized yarn and bulk matrix along with damage modelling techniques are given in Sections 5.4, 5.5 and 5.6. Finally, the results of the FE modelling are compared with experimental data for the two types of 3D woven composite T-joints in terms of load-displacement response, damage initiation and propagation in Section 5.7.

5.2 Literature review

Methods ranging from simple analytical solutions to complex FE models have been developed to predict the mechanical behaviour of textile composites [79]. In textile composites, there are both impregnated yarns and bulk matrix in the heterogeneous materials, thus, the hierarchy of these materials is usually classified according to the length scales: fibres in matrix of the impregnated yarns at the micro-scale, impregnated textile reinforcements of the composites at the meso-scale and 3D composite components at the macro-scale. The meso-scale textile geometry is at an additional length scale compared with laminated composites, but usually the impregnated yarns are locally considered as unidirectional (UD) composites so that most of the theories for modelling of UD composites are still applicable for textile composites at the meso-scale, except those relying on simplified assumptions regarding the fibre architecture. Benefiting from this feature at the meso-scale, multiscale modelling techniques have been widely used in modelling textile composite structures, which was reviewed by Lomov et al. [58] and Llorca et al. [80]. Due to the periodic feature of textile structures, the size of FE model can be significantly reduced compared with the size of composite part, after introducing the idea of representative volume element (RVE) or unit cell, which is the smallest repetitive portion of a composite at the meso-scale. At the micro-scale, a unit cell is also used in the

micro-meso homogenisation procedure to calculate the material properties for the impregnated yarn elements. The use of a unit cell requires assigning periodic boundary conditions to preserve continuity in the material, as demonstrated in [81] for UD composites with square or hexagonal fibre arrangements at the micro-scale, and in [82-84] for 2D and 3D textile composites at the meso-scale.

Lomov et al. [58] summarised the steps for meso-scale FE modelling of textile composites, which generally include: 1) Building the geometry of the reinforcement; 2) Transferring the fibre geometry into a volume description, i.e. a solid CAD model; 3) Adaption of solid geometry (CAD) model for meshing (not necessary if the geometry can be directly meshed; 4) Meshing; 5) Assigning material properties of the impregnated yarns and bulk matrix; 6) Boundary conditions; 7) Meso-macro homogenisation (only necessary for macro-scale FE modelling); 8) Damage initiation and propagation modelling. Some of the essential steps in meso-scale FE modelling are further discussed below.

Textile geometry models and meshing

As discussed in Chapter 2, the geometry of the textile reinforcement is essential for the subsequent simulation. For building the reinforcement geometry of textile composites, specially developed textile geometry preprocessors like TexGen [19] or WiseTex [50] are often used, which simplify this process significantly compared with using any other CAD software. Many successful attempts were made to model the geometries of textile composites using the above preprocessors for the resulting performance analysis. For example, TexGen was used for modelling of 2D textile composites in [85] and 3D textile composites in [86].

However, it should be noted that the actual textile structure in a composite is usually different from the idealised textile structure, as deformation arises from compaction or preforming in the manufacturing of textile composites. Numerical and analytical algorithms for modelling of textile deformation at the meso-scale

is the subject of significant research [87-89]. For complex textile composite, e.g. 3D textile composites, the creation of reinforcement geometry largely relies on the input of experimental measurements from microscopic and μCT analysis.

The meshing difficulty facing composites with complex fibre architecture was discussed in Section 4.2. In contrast to the geometry simplification/adaption methods introduced previously, Drach et al. [90] proposed a promising algorithm which does not significantly reduce the yarn volume fraction through artificially decreasing the size of yarn cross-sections, based on which meso-scale FE models for 3D woven composites can be constructed. However, the current method only supports the generation of tetrahedral elements and requires a fine mesh with 1–10 million degrees of freedom for a flat 3D woven composite unit cell, which limits its wide application due to high computation cost from modelling of a unit cell with geometric features or if damage modelling is to be incorporated in the FE analysis.

Properties of the impregnated yarns

The yarn in a textile composite is an assembly of thousands of fibres impregnated with the matrix like a unidirectional composite. The properties of the impregnated yarns are the parameters for the meso-scale FE analysis, which can be obtained by micromechanical formulae [71, 91], micro-scale FE analysis [92], with certain assumptions in the models, or experimental testing [93]. Lomov et al.[58] compared the results of micro-meso homogenisation by the Chamis model [71] and micro-scale FE modelling (hexagonal packing) for a carbon fibre/epoxy composite. As shown in Figure 5-1, there is good agreement in most of the predicted elastic constants between the two methods, when the intra-yarn fibre volume fraction V_f is ranging from 60% - 80%. The intra-yarn V_f is an important input for calculating these properties, determined by the V_f of the composite and the volume of the specific reinforcement geometry. Due to the large variability in reinforcement geometry of textile composites, the intra-yarn V_f may vary at different locations but this has not been taken into account in most

of the proposed FE modelling methods.

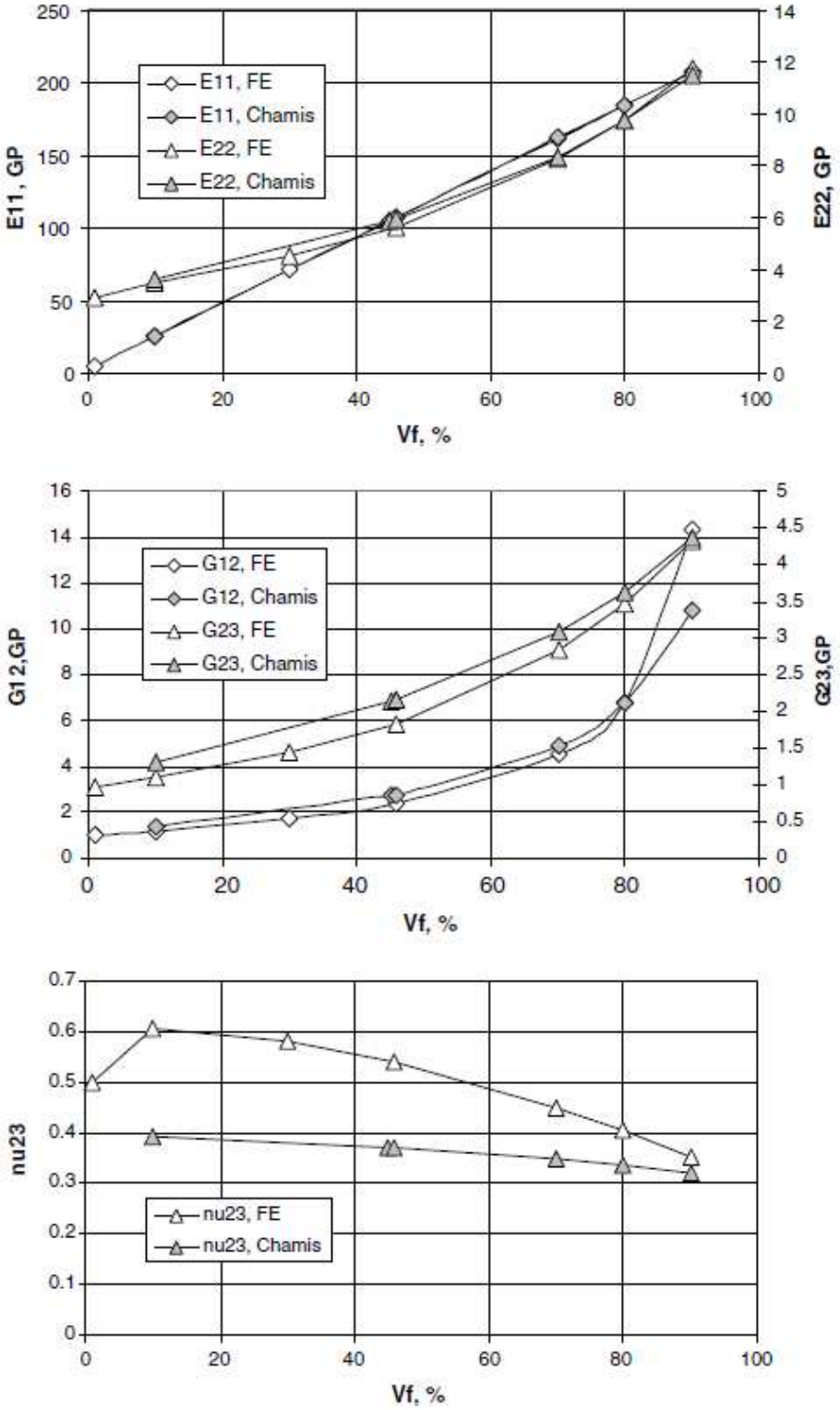


Figure 5-1 Comparison of the results of micro-homogenisation by the formulae of Chamis and micro-scale FE modelling for hexagonal packing of fibres [58]

The strength of the impregnated yarn depends on the strength of fibres, matrix and the bonding condition at their interface, as well as the intra-yarn V_f. Because of the heterogeneity of the impregnated yarn, damage might initiate in different constituents under different loading conditions which might lead to distinctive difference in the yarn's strength at different material directions. At the present stage, empirical approximate formulae can be used to obtain these in the absence of experimental data [58].

Meso-scale damage modelling

In meso-scale FE modelling, the impregnated yarn is usually homogenised and assumed to be transversely isotropic in most cases. The failure mechanisms for the impregnated yarn are mostly classified as fibre-dominated failure, caused by fibre rupture, and matrix-dominated failure, caused by matrix damage. In addition, the failure mechanisms under tension, compression, shear and any combination are distinctive, and as a result, the study of composite failure theories under 3D states of stress is complex when compared with those for isotropic materials.

The maximum stress/strain theory is the simplest failure criterion (e.g. Eq.(5.1) is the maximum stress criterion under plane stress) for homogenised UD composites, which can be used to predict the failure in principal material axes. Failure occurs if one of the stresses/strains is greater than the corresponding allowable stress/strain value in that direction. Note that as there is no interaction between stresses/strains, i.e. the stress/strain in one material direction would not affect the failure in another material direction, the prediction accuracy is not good under 3D states of stress.

$$\begin{aligned} -F_1^c < \sigma_1 < F_1^t \\ -F_2^c < \sigma_2 < F_2^t \\ \left|\tau_{12}\right| < F_{12} \end{aligned} \tag{5.1}$$

where F is the material strength, with subscripts *1* and *2* denote the fibre and

transverse directions in the local coordinate system of the yarn (fibre), and subscripts *c* and *t* stand for the compression and tension.

Several quadratic failure criteria accounting for interaction between stress components were proposed and used to predict the failure of UD composites, including the well-known Tsai-Hill criterion [94], Hoffman criterion [95] and Tsai-Wu criterion [96]. These criteria, as shown in Eq.(5.2) for the Tsai-Hill criterion for example, are not able to distinguish different failure modes in the composites, which strongly affects the mechanical behaviour during the damage stage.

$$\frac{\sigma_1^2}{F_1^2}-\frac{\sigma_1\sigma_2}{F_1^2}+\frac{\sigma_2^2}{F_2^2}+\frac{\tau_{12}^2}{F_{12}^2}=1 \tag{5.2}$$

A list of state-of-the-art failure criteria capable of predicting failure mode of the composites under different loading conditions were summarised in [97] , including Puck's failure theory [98], and Hashin's failure theory [99], which have been widely adopted for modelling of damage in laminated [100-102] and textile composites [103-108].

A number of leading composite failure theories were benchmarked by Hinton and colleagues [109-112] through a series of so-called World Wide Failure Exercises (WWFE), in which the predicted results from these theories for UD and multiply laminates under various loading conditions were compared with experimental data. Although some of the above-mentioned criteria, such as Hashin's and Puck's, performed much better than the others in the WWFE, none of the available failure criteria has been demonstrated to accurately predict damage for all composites and loading cases, therefore failure theory for composites, especially under complex states of stress, is the subject of continuing research.

For damage in directions other than the fibre direction, brittle failure does not

always occur and thus continuum damage mechanics (CDM) are often exploited to model damage propagation. Damage initiation is first evaluated by a failure criteria and then a degradation scheme on elastic constants is applied to the stiffness matrix. For instance, Nobeen et al. [113] proposed a modelling method for the progressive damage of braided composites based on an instantaneous damage model, in which an instantaneous reduction (degradation factor) on the material constants was applied once the damage for the impregnated yarns was predicted by the Hashin criteria. It should be noted that when damage was predicted in the fibre direction, the constants were reduced to a near zero value as it was assumed to be a complete failure. Good agreement with experiments was observed, however, one limitation with this method is that the degradation factor needs to be correlated with the experimental results. Similar schemes to degrade the elastic constants was also previously used in [114, 115].

Zako et al. [116] extended Hoffman's criterion through using stress-to-strength ratios to distinguish failure modes (Table 5-1), and introduced the Murakami damage tensor [117] into the material's global stiffness matrix after damage initiation, in the simulation of the failure behaviour of a plain weave composite. The constitutive model for the damaged materials was expressed as:

$$\begin{Bmatrix} \sigma_L \\ \sigma_T \\ \sigma_Z \\ \sigma_{TZ} \\ \sigma_{ZL} \\ \sigma_{LT} \end{Bmatrix} = \begin{bmatrix} d_L^2 C_{11} & d_L d_T C_{12} & d_Z d_T C_{13} & 0 & 0 & 0 \\ & d_T^2 C_{22} & d_Z d_T C_{23} & 0 & 0 & 0 \\ & & d_Z^2 C_{33} & 0 & 0 & 0 \\ & & & d_{TZ} C_{44} & 0 & 0 \\ & SYM & & & d_{ZL} C_{55} & 0 \\ & & & & & d_{LT} C_{66} \end{bmatrix} \begin{Bmatrix} \varepsilon_L \\ \varepsilon_T \\ \varepsilon_Z \\ \varepsilon_{TZ} \\ \varepsilon_{ZL} \\ \varepsilon_{LT} \end{Bmatrix} \tag{5.3}$$

where C_{ij} are the stiffness matrix components for the intact state. The subscripts *L*, *T*, and *Z* refer to the material principal coordinates.

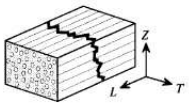
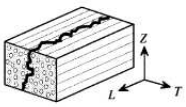
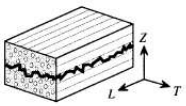
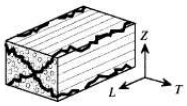
The parameters d_i (where $i=L, T, Z$) in Eq.(5.3) are defined according to the failure mode (Table 5-1) in each material direction:

$$d_L = 1 - D_L,\ d_T = 1 - D_T,\ d_Z = 1 - D_Z$$
$$d_{TZ} = \left(\frac{2d_T d_Z}{d_T + d_Z}\right)^2,\ d_{ZL} = \left(\frac{2d_Z d_L}{d_Z + d_L}\right)^2,\ d_{LT} = \left(\frac{2d_L d_T}{d_L + d_T}\right)^2 \quad (5.4)$$

where D_i, (i=L, T, Z) is the damage tensor defined in Table 5-1.

Once damage was initiated in the composites according to the criteria listed in Table 5-1, the corresponding damage tensor D_i components were suddenly increased from 0 to 0.99 (close to 1). Good agreement was obtained between the simulation and experiment on the reduction of elastic modulus under uniaxial tension (Figure 5-2), but the proposed method predicted an abrupt loss of stiffness at a strain of 1%. This is likely to be caused by the sudden change in the damage variable for the transverse direction once damage is initiated.

Table 5-1 The failure criteria and damage parameters for impregnated yarn used in [116]

Damage mode	Anisotropic damage model for fiber bundle			
	Mode L	*Mode T & LT*	*Mode Z & ZL*	*Mode TZ*
				
Maximum stress-to-strength ratio	$\frac{\sigma_L^2}{F_L^t F_L^c}$	$\frac{\sigma_T^2}{F_T^t F_T^c}$ or $\left(\frac{\tau_{LT}}{F_{LT}^s}\right)^2$	$\frac{\sigma_Z^2}{F_Z^t F_Z^c}$ or $\left(\frac{\tau_{ZL}}{F_{ZL}^s}\right)^2$	$\left(\frac{\tau_{TZ}}{F_{TZ}^s}\right)^2$
Damage tensor $\begin{bmatrix} D_L & 0 & 0 \\ 0 & D_T & 0 \\ 0 & 0 & D_Z \end{bmatrix}$	$\begin{bmatrix} 1 & 0 & 0 \\ 0 & 0 & 0 \\ 0 & 0 & 0 \end{bmatrix}$	$\begin{bmatrix} 0 & 0 & 0 \\ 0 & 1 & 0 \\ 0 & 0 & 0 \end{bmatrix}$	$\begin{bmatrix} 0 & 0 & 0 \\ 0 & 0 & 0 \\ 0 & 0 & 1 \end{bmatrix}$	$\begin{bmatrix} 0 & 0 & 0 \\ 0 & 1 & 0 \\ 0 & 0 & 1 \end{bmatrix}$

Puck and Schurmann [118] developed a phenomenological law to degrade the material constants after damage initiation, in conjunction with their failure criterion. Progressive damage behaviour can be predicted by this method and they offered recommendations on the selection of empirical parameters in the damage model in the absence of experimental data. A similar phenomenological damage model was also proposed by Ruijter [119]. Although there are suggestions on selection of empirical parameters in these models, they still need to be fully validated against experimental data due to the phenomenological nature. Energy-based damage

models were proposed in several studies [120, 121], but this requires the determination of fracture toughness through experiment as an input to the models.

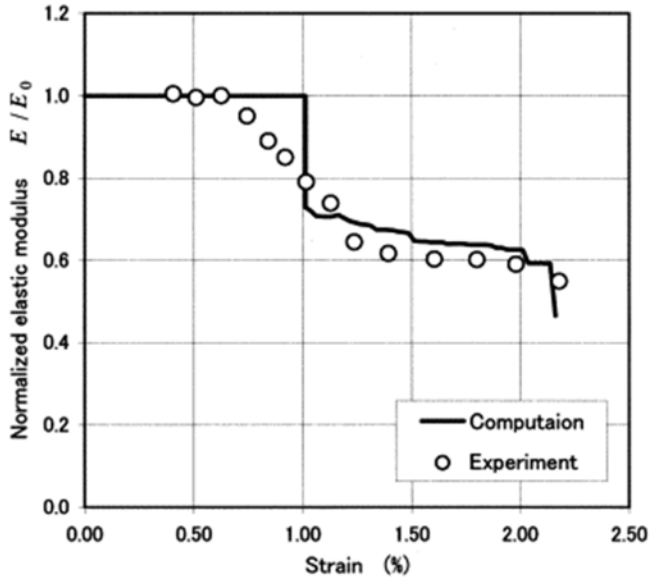


Figure 5-2 Comparison of elastic modulus at various loading strains between computational and experimental results [116]

In summary, the lack of a thorough understanding of composite failure mechanisms, and the inability to perform the required meshing and geometric modelling, hold back the development of a well-established predictive modelling method for composite's mechanical performance. Although the available meso-scale FE modelling methods for 2D textile composites are applicable to 3D woven composites, a challenge is further raised due to the complex fibre architecture and states of stress in 3D woven materials. A number of meso-scale FE models for the mechanical performance of 3D woven composites showing good agreement with experiments were reported [122-124], but the majority of published studies were based on simple flat unit cells, or were not validated for a different weave pattern. For 3D woven composites with geometric features, the fibre architecture would become more complex than for 3D woven composite flat panels, and no publications on the modelling of such materials at meso-scale have been reported.

5.3 Construction of meso-scale 3D woven T-joint models

Generating the reinforcement geometry within a composite plays a pivotal part in the meso-scale FE analysis. The accuracy of the predicted composite performance can be improved based on a meso-scale model with realistic fibre geometry [38, 45]. The reinforcement geometries of the two types of 3D woven T-joint were modelled using TexGen, based on the geometric parameters of yarns extracted from μCT analysis. The dimensions of yarn cross-sections in the TexGen models are the average values obtained from μCT data as shown in Table 3-1.

Geometry simplification methods such as artificially decreasing the size of yarn cross-sections to introduce thin layers of neat matrix in-between adjacent yarns [58, 125, 126] were not used here. For the meso-scale models, which aim to predict the mechanical behaviour resulting from yarn/matrix debonding, the effects of a non-realistic interface on accuracy is expected to be important, although little deviations in accuracy were found for damage analysis without considering failure by debonding [125, 126]. Further investigation on this effect is recommended before using such simplification methods to model interface damage.

The fibre architectures of the two types of 3D woven T-joint have identical 3D orthogonal weave patterns in the flange and web sections, with the only difference being the geometry of the junction region. Thus construction of the meso-scale models for the composite T-joints followed the strategy of dividing the T-shaped structure into three sub-geometries: the junction region representing the weave variation, and the flange and web sections which are tessellated by two unit cells of 3D orthogonal weaves, as illustrated in Figure 5-3 for the geometry of the 3D woven type 1 T-joint. This modelling strategy facilitates the construction of other types of 3D woven T-joints by only varying the geometry of the junction region (Figure 5-4).

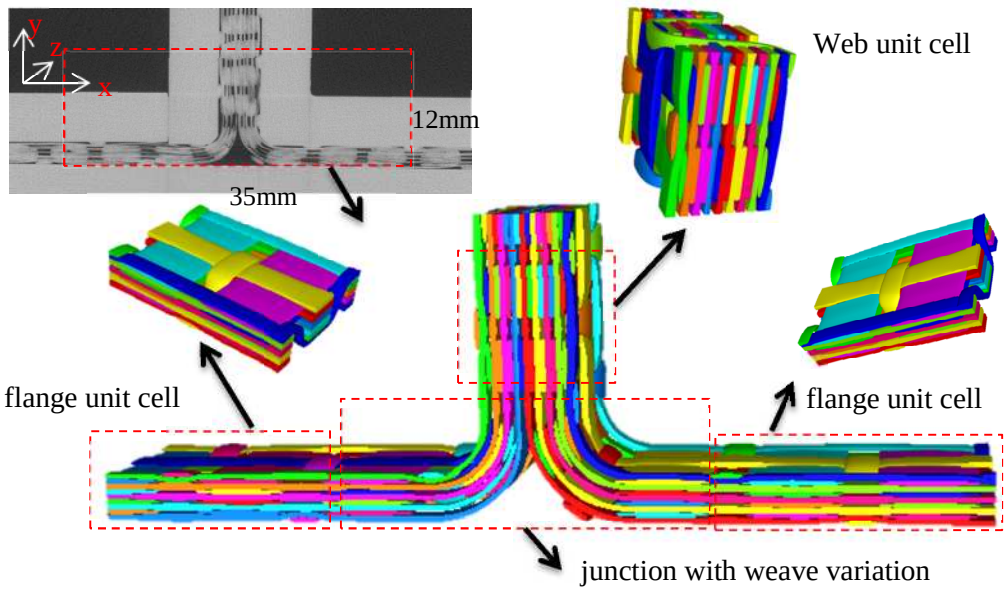


Figure 5-3 Geometric model for 3D woven type 1 T-joint

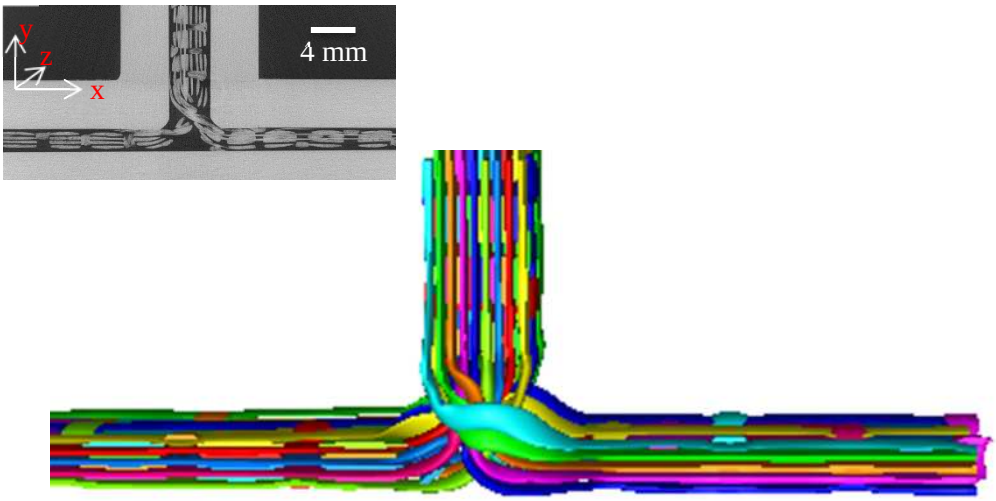


Figure 5-4 Geometric model for 3D woven type 2 T-joint

The TexGen models were built through python scripting, and a scripting guide for TexGen can be found in [127]. In summary, the general procedures for building the T-joint geometries in this work are as follows: Step 1, measuring the yarn cross-section dimensions and spacings using μCT; Step 2, measuring the coordinates of selected points on yarn path (centre of each cross-section) using μCT, subsequently to be used as "node" in TexGen; Step 3, defining the yarn

path using measured coordinates of nodes from Step 2 and assigning yarn cross-sectional shapes from Step 1 in TexGen. A script for illustrating how to implement the proposed methodology for modelling of bent yarn cross-section shape (Section 3.4.2) in TexGen, for the 3D woven type 1 T-joint, is given in Appendix D. In addition, the method used to extract geometric parameters such as yarn path and cross-section dimension at the junction region of the 3D woven type 2 T-joint model is presented in Appendix D. Building a meso-scale model for the full size of the composite T-joint specimen is unrealistic as it requires huge computation resource to run the analysis. This is also a current issue in modelling of 3D woven composite structures, as these materials could not be readily homogenised due to geometric features, or when yarn/matrix debonding is to be considered. Benefiting from the periodic fibre architecture of woven reinforcements, only a repeat unit (unit cell) was modelled along its width direction (*z*-axis in Figure 5-3). Additionally, the length of the web in the geometric models is reduced, as the deformation in the web was negligible in comparison with the deflection from bending of the flange, due to the high effective modulus in the web along its length/loading direction (*y*-axis in Figure 5-3).

As concluded from Chapter 4, a voxel meshing method was used in discretising the geometric models due to the complexity in the fibre architectures of the 3D woven T-joints where conformal meshing is difficult to achieve. Shown in Figure 5-5 and Figure 5-6 are the voxel-discretised models generated by TexGen based on the above reinforcement geometries, providing an element length of 0.1 mm (the number of elements for 3D woven type 1 model is 749,328 and for 3D woven type 2 model is 748,457). This element length was chosen based on the mesh convergence study on the reduced models in Section 4.3.3. Cohesive surfaces (zero thickness) between yarns and matrix were then added in the voxel models using Hypermesh (Version 13.0) [128]. Note that in order to improve the computational efficiency, there are no interface elements added in the web of the 3D woven type 2 model because no delamination was observed in that region in mechanical tests.

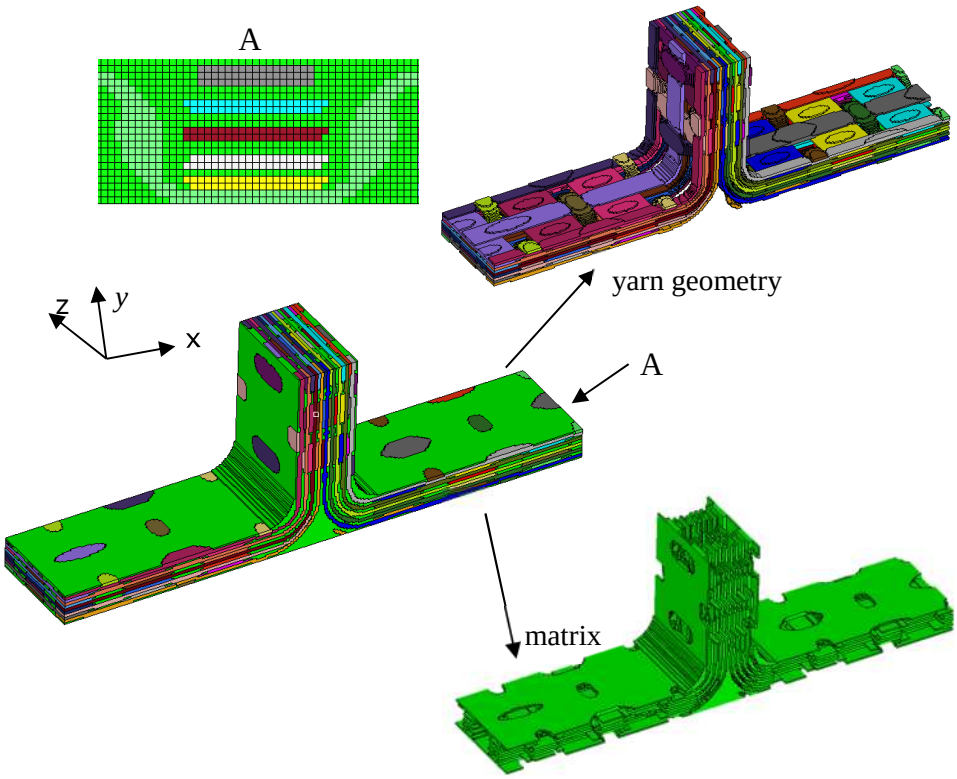


Figure 5-5 Voxel model for 3D woven type 1 T-joint (element length 0.1 mm)

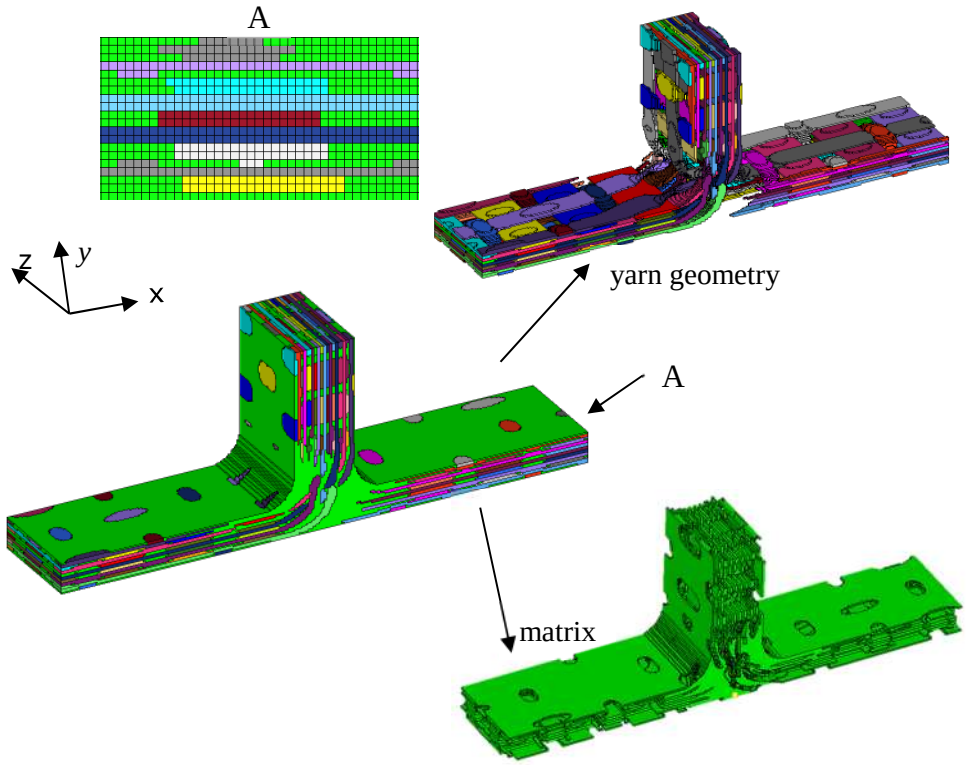


Figure 5-6 Voxel model for 3D woven type 2 T-joint (element length 0.1 mm)

5.4 Boundary conditions

The boundary conditions (BCs) used in the meso-scale models to simulate the quasi-static tensile pull-off tests on the 3D woven T-joint specimens are shown in Figure 5-7. A displacement-controlled load in the *y*-axis direction (U_2) was prescribed on the nodes of the top surface (EE'FF') of the models, with the other two translational degree of freedom constrained (U_1=U_3=0). A smooth amplitude was used rather than a linear one to avoid oscillations on the load-displacement response.

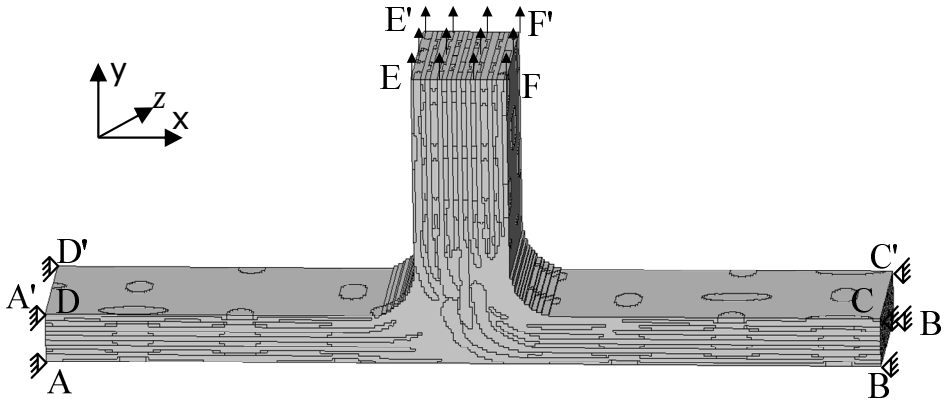


Figure 5-7 Boundary conditions for the 3D woven T-joint models subjected to a quasi-static tensile pull-off load

AA'DD' and BB'CC' are the surfaces at the edges of clamps on the flange of the specimens, and therefore the nodes on them were assumed to be fixed (U_1= U_2=U_3=0). It should be noted that after introducing the cohesive surfaces at the constituent interface, the matrix and yarn elements contacting each other no longer share nodes at their interface, instead two nodes are defined at the same spatial location (named as interfacial node pair) for the matrix and yarn elements respectively, and the traction-separation law (Section 4.4.1) is enforced between all the interfacial node pairs. To avoid over-constraint on the nodes of the boundaries of the flange, only the interfacial nodes of the matrix on the surfaces AA'DD' and BB'CC' were constrained in the above manner (U_1= U_2=U_3=0), and thus the interfacial nodes of the yarns on the surfaces AA'DD' and BB'CC' were free in the boundary conditions but constrained by the cohesive tractions from

the corresponding interfacial nodes of the matrix.

As discussed in Section 5.3, due to the periodic weave patterns of the preforms in the width direction (*z*-axis in Figure 5-7), only a unit cell width of preform was constructed in the meso-scale models. Periodic boundary conditions are thus expected to be prescribed on the front and back surfaces of the models but this was shown to lead to a higher computation cost and instability when solving by Abaqus Explicit because of the large size of the FE models, compared to the models with free boundary conditions in the width direction. In addition, a deviation of less than 2% in elastic response between unit cell models with and without periodic boundary conditions was found through a study of braided composites under uniaxial loading [125]. Similarly, non-periodic boundary conditions were also used by other authors in the failure analysis of textile composites [113], as the requirement of identical coordinates for the node pairs on the opposite faces of the model for periodic boundary conditions is difficult to meet for textile composites. In this study, an analysis of the effects of using non-periodic boundary conditions on structural stiffness and strength was carried out on a reduced model for the 3D woven T-joint subjected to the same loading condition, which only have weft yarns as shown in Figure 5-8. The results for a unit cell width model with and without periodic boundary conditions (BCs) in the width direction were compared to the results of full sized model. A deviation of about 5% in stiffness and strength was identified (Table 5-2) and therefore periodic boundary conditions were not adopted in the 3D woven T-joint models.

Table 5-2 Comparison of stiffness and peak load among full sized, unit cell with and without periodic BCs models

model	Stiffness normalized to full size	Peak load normalized to full size
full sized	1	1
unit cell with BCs	1.0074	1.0002
unit cell without BCs	0.9530	0.9493

It should be noted that since the yarns are taken from real CT scan data they will not be properly periodic, which is a potential source of variability for the geometric models generated based on CT data.

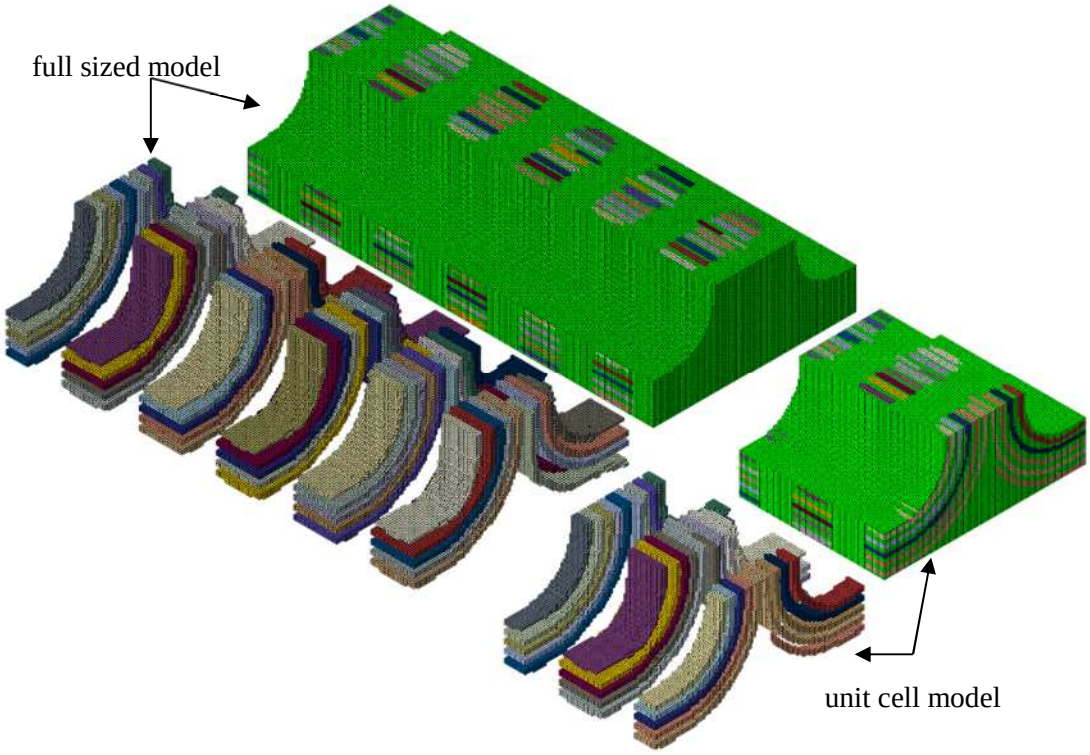


Figure 5-8 Full sized and unit cell simplified T-joint models to study the effect of periodic boundary conditions

5.5 Constituent material properties

5.5.1 Determination of intra-yarn fibre volume fraction

An averaged intra-yarn fibre volume fraction (intra-yarn V_f) by preserving the overall V_f of the composite based on the volume of yarns in the specific geometric model is commonly used to characterise the yarn's properties in modelling of textile composites [104]. However, the intra-yarn V_f may vary in different yarns or at different locations of a yarn. In the performed mechanical tests in Chapter 2, the stiffness of the structure is dominated by the effective modulus of the flange in the *x*-direction, and more specifically, the moduli in the

fibre direction of the weft yarns in the flange, as the moduli of the matrix, warp (transverse direction) and binder (transverse direction) yarns in the *x*-direction are significantly lower than that of the weft yarns (fibre direction). Additionally, the failure behaviour is sensitive to the path of weft yarns as this is the only weave variation between the two types of 3D woven T-joint. Consequently, instead of using an averaged intra-yarn V_f for the whole model, variation in the intra-yarn V_f for warp, weft and binder yarns were considered in this study, which were respectively calculated by matching the V_f of the composite in each yarn direction.

An approximation of the fibre volume fraction of the composite in the weft yarn direction V_f^{weft} is as follows, assuming a straight yarn path (without crimp):

$$V_f^{weft} = \frac{n_{weft} A_f^{yarn}}{A_{section}} \tag{5.5}$$

where $A_{section}$ is the area of the cross-section (perpendicular to the weft direction) of the flange; $A_f^{yarn} = 12k \times \pi d_f^2/4$ is the total fibre area in the section for a weft yarn of 12K filament count, d_f is the fibre diameter; n_{weft} is the total number of weft yarns in the flange which can be obtained from the µCT scan (Figure 5-9).

Then the intra-yarn fibre volume fraction can be obtained through dividing the above fibre volume fraction of the composite in the weft yarn direction V_f^{weft} by the volume fraction of weft yarns in the voxel model.

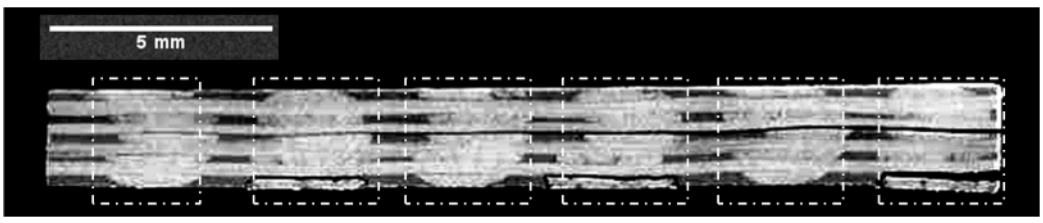


Figure 5-9 µCT scan of the section of the flange (perpendicular to the weft direction) showing n_{weft}=30, there are 6 yarn stacks and 5 weft yarns per stack

The above method is also applicable for the warp yarns. A coefficient greater than one is needed on the numerator of Eq.(5.5) to account for the yarn path curvature of the binders. µCT scan is not always necessary if n_{weft} can instead be acquired from the preform manufacturer. Based on Eq.(5.5), for the 3D woven type 1 T-joint model, the calculated intra-yarn V_f for the weft yarns is 62.7%, which is close to that of the warp (71.9%) and binder yarns (56.8%). To simplify the model, the same intra-yarn V_f of the weft yarns was used across the whole model in the FE analysis. Because the predicted failure behaviours are far more sensitive to the properties of the weft yarns than those of the warp or binder yarns, a small deviation is likely to be caused by ignoring the variation in the intra-yarn fibre volume fraction.

At the same time, the intra-yarn V_f was considered unchanged for the two types of 3D woven T-joint because they were made of the same materials at the same global fibre volume fraction, and the weave variation between them is only in the path of weft yarns at the junction.

5.5.2 Homogenized yarn properties

The yarn in the woven composite is made of thousands of fibres impregnated with the matrix like a UD composite, and usually the properties of the yarn elements are approximated by the properties of a homogenized UD composite with a V_f equivalent to the intra-yarn V_f of the yarn.

Similar to dealing with laminates, the homogenized yarn is assumed to have transversely isotropic properties which can be obtained either by the micro-scale unit cell modelling or an analytical solution based on micromechanics. As the predicted results from analytical method agrees well with the micro-scale FE modelling at the fibre volume fraction for this study (Figure 5-1), the Chamis model [71] was used to calculated the homogenized yarn properties, reproduced below:

$$
\begin{aligned}
E_1 &= V_f E_{f,1} + \left(1 - V_f\right) E_m \\
E_2 = E_3 &= \frac{E_m}{1 - \sqrt{V_f}\left(1 - E_m / E_{f,2}\right)} \\
G_{12} = G_{13} &= \frac{G_m}{1 - \sqrt{V_f}\left(1 - G_m / G_{f,12}\right)} \\
G_{23} &= \frac{G_m}{1 - \sqrt{V_f}\left(1 - G_m / G_{f,23}\right)} \\
\nu_{12} = \nu_{13} &= V_f \nu_{f,12} + \left(1 - V_f\right)\nu_m
\end{aligned}
\tag{5.6}
$$

where subscripts *1, 2* and *3* denote the fibre, transverse and through-thickness directions in the local coordinate system of the yarn (fibre) respectively; subscripts *m* and *f* stand for the matrix and fibre.

The calculated properties along with the properties for Hexcel IM7 carbon fibre and Gurit Prime 20LV epoxy resin are listed in **Error! Reference source not found.**.

Due to the absence of experimental data, a set of empirical formulae for calculating the strengths of the homogenized yarn was used [58]:

$$
\begin{aligned}
F_1^t &= F_{f,1} V_f + \left(1 - V_f\right) F_m^t \frac{E_m}{E_{f,1}} \\
F_1^c &= \frac{G_m}{1 - V_f\left(1 - \dfrac{G_m}{G_{f,12}}\right)} \\
F_2^t = F_3^t &= F_m^t \frac{E_{f,2}}{E_m}\left(1 - V_f\right) \\
F_2^c = F_3^c &= F_m^c \frac{E_{f,2}}{E_m}\left(1 - V_f\right) \\
F_{12} = F_{23} = F_{31} &= \frac{1}{2} F_2^c
\end{aligned}
\tag{5.7}
$$

where *F* is the UD material strength and superscripts *t* and *c* denote tension and compression.

Table 5-4 lists the calculated strengths of the homogenised yarn for using in the

FE analysis and they are compared to the properties of a HexPly 8552 composite (V_f=60%) obtained by mechanical testing. It is found that the analytical formulae gave good agreement with the experimental data for transverse properties but may slightly overestimate the properties in the fibre direction. However, this may be not critical until the final failure as the damage in the fibre direction occurred much later than other types of damage in the T-joints.

Table 5-3 Elastic properties of constituent materials

	E_1 (GPa)	E_2=E_3 (GPa)	v_{12}=v_{13} (-)	v_{23} (-)	G_{12}=G_{13} (GPa)	G_{23} (GPa)
Prime 20LV Epoxy resin [129]	3.5		0.35			
IM7 Carbon Fibre [122]	276	15	0.279		12	5.02
IM7 Carbon Yarn (Intra-yarn V_f=62.7%)	174.4	8.9	0.305	0.475	4.2	3

Table 5-4 Strengths of constituent materials

	F_1^t (MPa)	F_1^c (MPa)	F_2^t (MPa)	F_2^c (MPa)	F_{12}=F_{23}= F_{31} (MPa)
Prime 20LV Epoxy resin [129]	73	146			
IM7 Carbon Fibre [122]	5655				
IM7 Carbon Yarn (Intra-yarn V_f=62.7%, by Eq.(5.7))	3546	2754	116.7	233.4	116.7
HexPly 8552 Composite, V_f=60%, by testing [130]	2723	1793	111		128[1]

[1] 0º short beam shear

5.6 Damage modelling

To model the failure of composites, the damage modes considered in the FE models should cover all the potential failure modes, although sometimes for simplicity, only the failure events observed in mechanical tests are included. In the present study, the damage modelling incorporated the yarn/matrix interface

damage and damage in constituent materials, i.e. bulk matrix and homogenized yarn materials.

The same method for modelling interface damage introduced in Chapter 4 was used here with the interface properties as listed in Table 5-5 [78]. It should be noted that the interface stiffness scaling method (k_n=k_s=k_t=10^4 MPa/mm) was adopted for the voxel-based cohesive models and more detail can be found in Section 4.5.3.

Table 5-5 Interface properties used in the cohesive models

k_n= k_s=k_t	τ_n^0	τ_s^0=τ_t^0	G_n^C	G_s^C	G_t^C	p
10^4 MPa/mm	30 MPa	60 MPa	0.22 mJ/mm^2	1.2 mJ/mm^2	1.2 mJ/mm^2	2

For damage in the homogenized yarn material, Hashin's failure criteria [99] developed for UD composites were used here to capture the damage initiation for each failure mode:

$$
\begin{aligned}
&I_1 \geq 0:\ \mathrm{d}_1 = \left(\frac{I_1}{F_1^t}\right)^2 + \frac{I_4}{F_{12}^2} = 1, \\
&I_1 \leq 0:\ d_2 = \left(\frac{I_1}{F_1^c}\right)^2 = 1; \\
&I_2 \geq 0:\ d_3 = \left(\frac{I_2}{F_2^t}\right)^2 + \frac{I_3}{F_{23}^2} + \frac{I_4}{F_{12}^2} = 1, \\
&I_2 \leq 0:\ d_4 = \left[\left(\frac{F_2^c}{2F_{23}}\right)^2 - 1\right]\left(\frac{I_2}{F_2^c}\right) + \left(\frac{I_2}{2F_{23}}\right)^2 + \frac{I_3}{F_{23}^2} + \frac{I_4}{F_{12}^2} = 1; \\
&I_1 = \sigma_1;\ I_2 = \sigma_2 + \sigma_3;\ I_3 = \tau_{23}^2 - \sigma_2\sigma_3;\ I_4 = \tau_{12}^2 + \tau_{13}^2
\end{aligned}
\tag{5.8}
$$

where I_1 to I_4 are the four stress invariants; with $I \geq 0$ for tension and $I \leq 0$ for compression; d_1 and d_2 are the damage parameters for the fibre direction (fibre dominated failure modes); d_3 and d_4 are the damage parameters for the transverse direction (matrix dominated failure modes).

Bulk matrix damage was evaluated by the pressure dependent modified von Mises criterion which can take into account the difference between tensile and compressive strength for the isotropic material [131]:

$$d_m = \frac{F_m^c - F_m^t}{F_m^c F_m^t}(\sigma_1 + \sigma_2 + \sigma_3) + \frac{1}{2F_m^c F_m^t}\left[(\sigma_1 - \sigma_2)^2 + (\sigma_2 - \sigma_3)^2 + (\sigma_1 - \sigma_3)^2\right] \tag{5.9}$$

where F_m^c, F_m^t are the compressive and tensile strengths of the bulk matrix respectively.

After damage initiation, the behaviour of the damaged constituent materials was modelled by a continuum damage mechanics (CDM) approach, which degrades the moduli of the damaged constituent materials through a phenomenological law first proposed by Ruijter [119]:

$$P(d_i) = \left(1 - \frac{1}{\exp(-c_1 d_i + c_2)}\right) \tag{5.10}$$

where $P(d_i)$ is a stiffness penalty factor function for degrading the corresponding modulus in terms of the failure modes d_i defined in Eq.(5.8) and (5.9). c_1 and c_2 are constants and Ruijter [119] found that c_1=8 and c_2=13 gave good agreement with the experimental stress-strain response for plain weave carbon/epoxy composites under tensile load. A minimum value of 0.001 for the stiffness penalty factor $P(d_i)$ was maintained when the material is considered to be fully damaged to avoid numerical instability.

Thus the elastic properties of the damaged yarn material are:

$$E_1^d = E_1 coef_1 \tag{5.11}$$

$$G_{12}^d = G_{13}^d = G_{12} coef_1 \tag{5.12}$$

$$E_2^d = E_3^d = E_2 coef_1 coef_2 \tag{5.13}$$

$$G_{23}^d = G_{23} coef_1 coef_2 \tag{5.14}$$

$$coef_1 = \begin{cases} \max\left(0.001, P\left(d_1\right)\right) & d_1 \geq 1 \\ 0.001 & d_2 \geq 1 \end{cases} \qquad (5.15)$$
$$coef_2 = \max\left(0.001, \min\left(P\left(d_3\right), P\left(d_4\right)\right)\right)$$

where E, G with superscript d denote the moduli of the damaged yarn material. Note that catastrophic damage is assumed after the initiation of compressive failure ($d_2 \geq 1$) in the fibre direction, as in Hashin's failure criteria (Eq.(5.8)) it is only determined by the stress invariant I_1. The properties relating to the transverse direction are also gradually degraded with the accumulation of damage in the fibre direction. Poisson's ratios ν_{12}, ν_{13} and ν_{23} are assumed to be unchanged in order to maintain a symmetric stiffness matrix after damage initiation.

Similarly, the Young's modulus of the damaged bulk matrix material is:

$$E_m^d = E_m \max\left(0.001, P\left(d_m\right)\right) \qquad (5.16)$$

where E with superscript d denotes the Young's modulus of the damaged matrix material. The stiffness penalty factor for the Young's modulus of damaged bulk matrix is calculated by using d_m and the same constants c_1 and c_2 in Eq.(5.10).

5.7 Results

FE models were solved by Abaqus Explicit (version 6.13) with a user-defined material subroutine (VUMAT), in a parallel mode (16 CPUs) using the High Performance Computing facility at the University of Nottingham. Each analysis took approximately 30 hours to run at a loading speed of 1 mm/ms. Again, mass scaling was not used as there is no strain rate effect in the materials. The loading rate was selected to ensure the inertia effect is negligible. Because both T-joint specimens are made of same materials along with the same fibre volume fraction, identical material and interface properties were used in the FE models for simulation of the tensile pull-off tests. In this section, the predicted mechanical behaviour from the proposed FE method for modelling the two types of 3D woven T-joint subjected to quasi-static tensile pull-off loading is compared to

the experimental results as first introduced in Section 2.6, in terms of initial stiffness, damage imitation, failure mode and damage propagation.

Figure 5-10 and Figure 5-11 show the predicted load-displacement responses from FE modelling for the two types of 3D woven T-joint respectively, in comparison with experimental data. Good agreement in the initial stiffness for both T-joints was obtained. After introducing the voxel-based cohesive elements in the FE models, the non-linearity in the stiffness was captured accurately, whilst a previous study based on perfect-bonding condition was found to over-predict the stiffness [132]. This good agreement in the initial stiffness between simulation and experimental data validates the necessity of scaling down the interface stiffness of voxel-based cohesive models as proposed in Section 4.5.3.

It was also observed from the comparisons of load-displacement responses that the predicted initial failure loads from the FE method are close to the experimental results, although variability from the tested specimens was found as listed in Table 2-1. It should be noted that it is difficult to determine an accurate loading displacement for damage initiation unless from the load-displacement responses, as damage initiated inside the specimens is hard to observe in the testing and also that the first failure of an element (material or interface) in the FE models could not represent the macroscopic damage in the specimens.

In the mechanical tests, the damage onset of the 3D woven type 2 specimen occurred later than that of the 3D woven type 1 specimen leading to a higher initial failure load, and this feature resulting from the difference in the reinforcement architectures was successfully captured by the FE method. From the analysis of the test results in Section 2.6, it was found that the difference in the initial failure loads was caused by different failure modes in the two types of 3D woven T-joint: delamination was the main failure event for the 3D woven type 1 specimen but it was arrested in the 3D woven type 2 specimen due to the weave variation, instead resin damage initiated in the noodle area of the 3D

woven type 2 specimen.

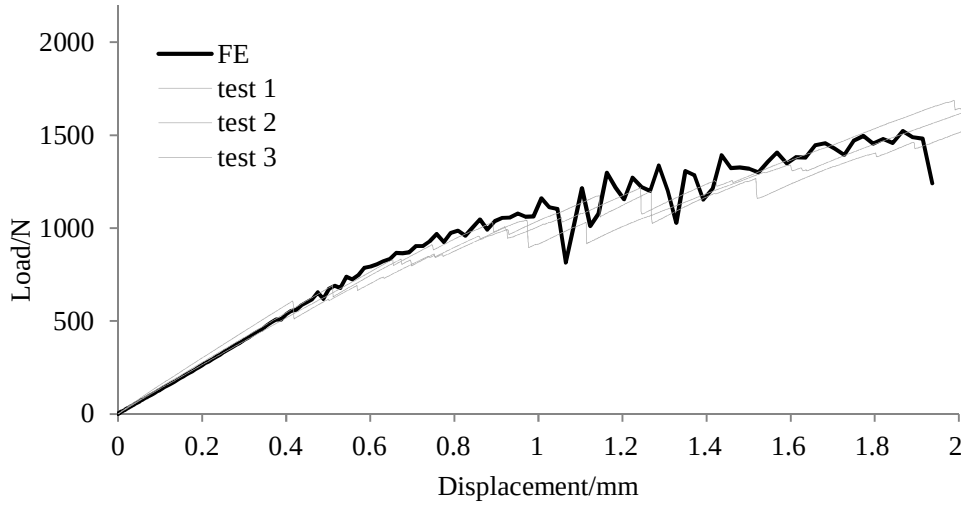


Figure 5-10 Predicted load-displacement responses for the 3D woven type 1 composite in comparison with test results

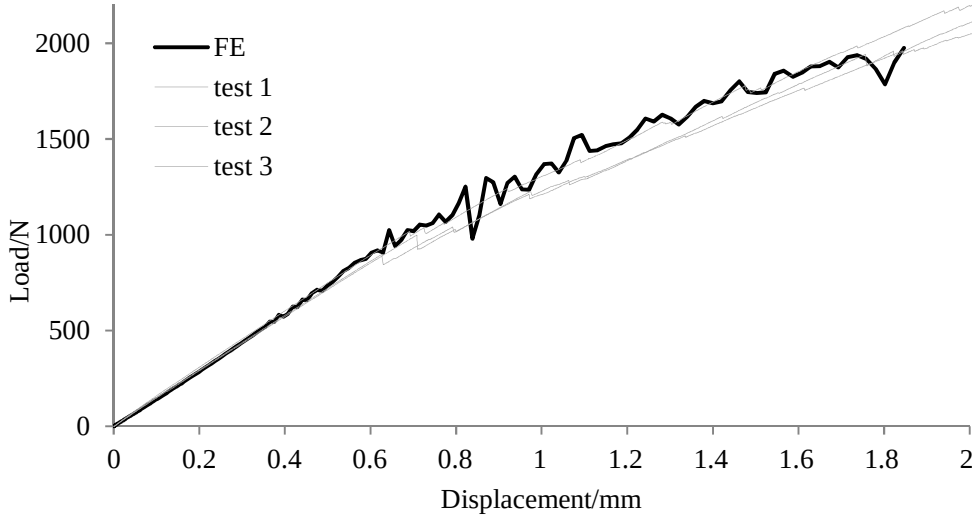


Figure 5-11 Predicted load-displacement responses for the 3D woven type 2 composite in comparison with test results

The FE models also predicted the different damage onset modes for the two T-joints. Figure 5-12 compares the evolution of the yarn/matrix interface damage in the two FE models during the loading step, which predicted that, in the simulation only the type 1 model suffered severe delamination as observed in

the experiment. Benefiting from the feature of weft yarn entanglement, the majority of interface elements in the type 2 model were subjected to compressive stresses due to the interaction between entangled yarns which would not initiate delamination. In the type 1 model, however, most of the interface elements which are away from the binder yarns were exposed to tensile stresses similar to loading a laminate in the through thickness direction. Delamination was therefore the main failure mode for the type 1 model while damage in the type 2 model initiated in the bulk matrix material.

In addition, the damage modes predicted by the FE models were compared against the images taken by DIC camera during the tests and μCT scans taken after the tests. As shown in Figure 5-13, the onset locations of delamination in the 3D woven type 1 model are in a good agreement with the locations shown in images taken at similar displacements. The propagation of delamination in the simulation was slightly faster than in the experiment but this did not significantly deviate the predicted global load-displacement response from the experimental data. The interface properties (mainly critical energy release rates) used in the FE model could affect the speed of delamination propagation, to which it seems the global load-displacement curve is relatively insensitive, provided they are comparable to the physical properties of the carbon/epoxy interface. That is why previous researchers did not apply exactly the same properties for the same material interface, e.g. carbon/epoxy, but good correlations with experimental data were still reported [133, 134].

For the 3D woven type 2 model, as shown in Figure 5-14, the predicted damage initiated in the resin-rich area of the noodle and the damage onset locations are close to those observed in the experiment. However, the adopted failure modelling method for the bulk resin is not adequate to model abrupt matrix cracks. The failure event of fibre damage in the weft yarns of the 3D woven type 2 specimens found by the μCT scans were also predicted by the FE models (Figure 5-15), but it is difficult to determine at what stage the fibre damage in the weft yarns initiated because μCT analysis for the internal damage of the

specimens during the tests was not available.

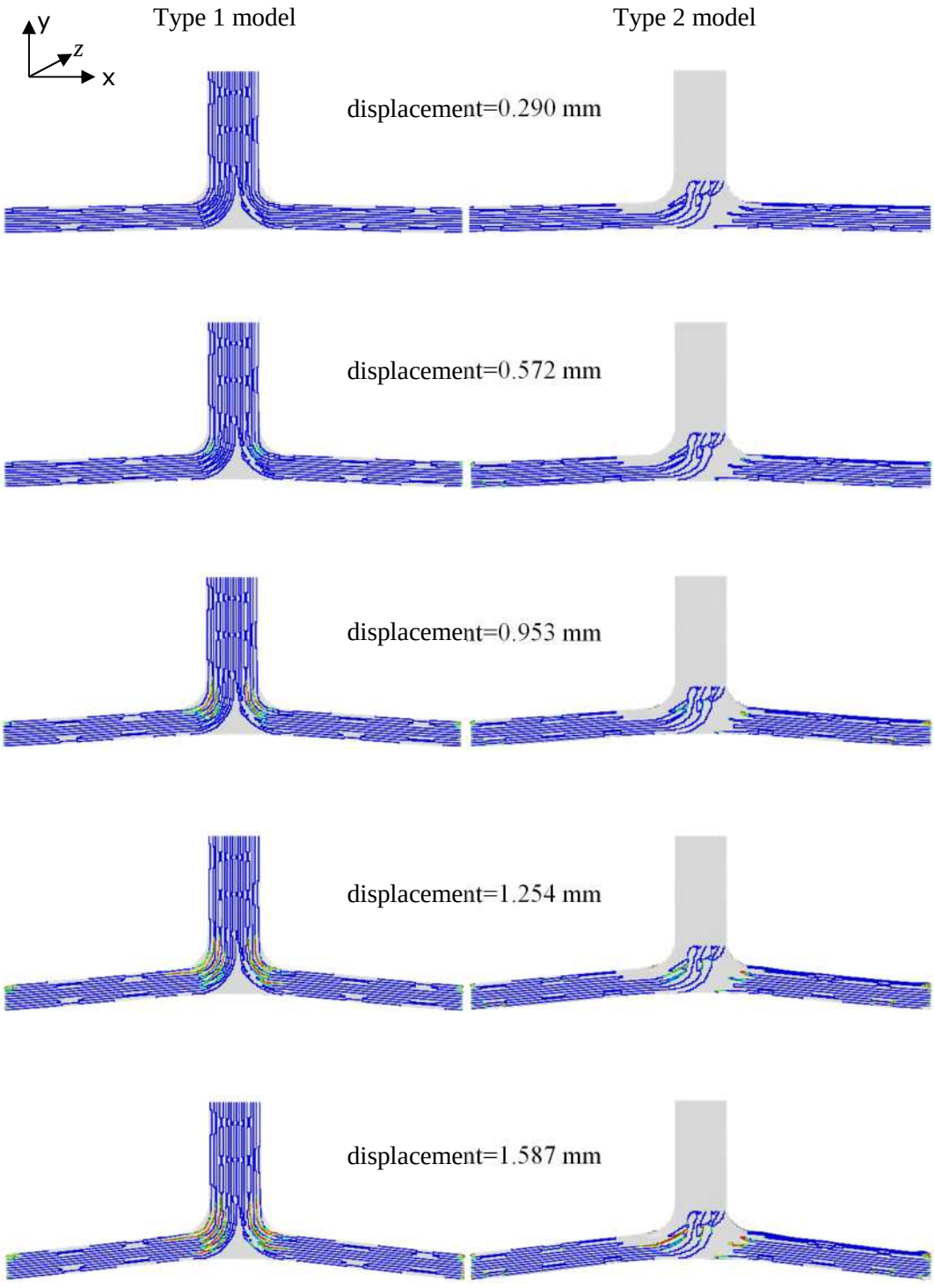


Figure 5-12 Comparison of progressive interface damage in 3D woven type 1 (left) and 3D woven type 2 (right) FE models; the failed interfaces (full failure) are shown in red and the intact interfaces are shown in blue

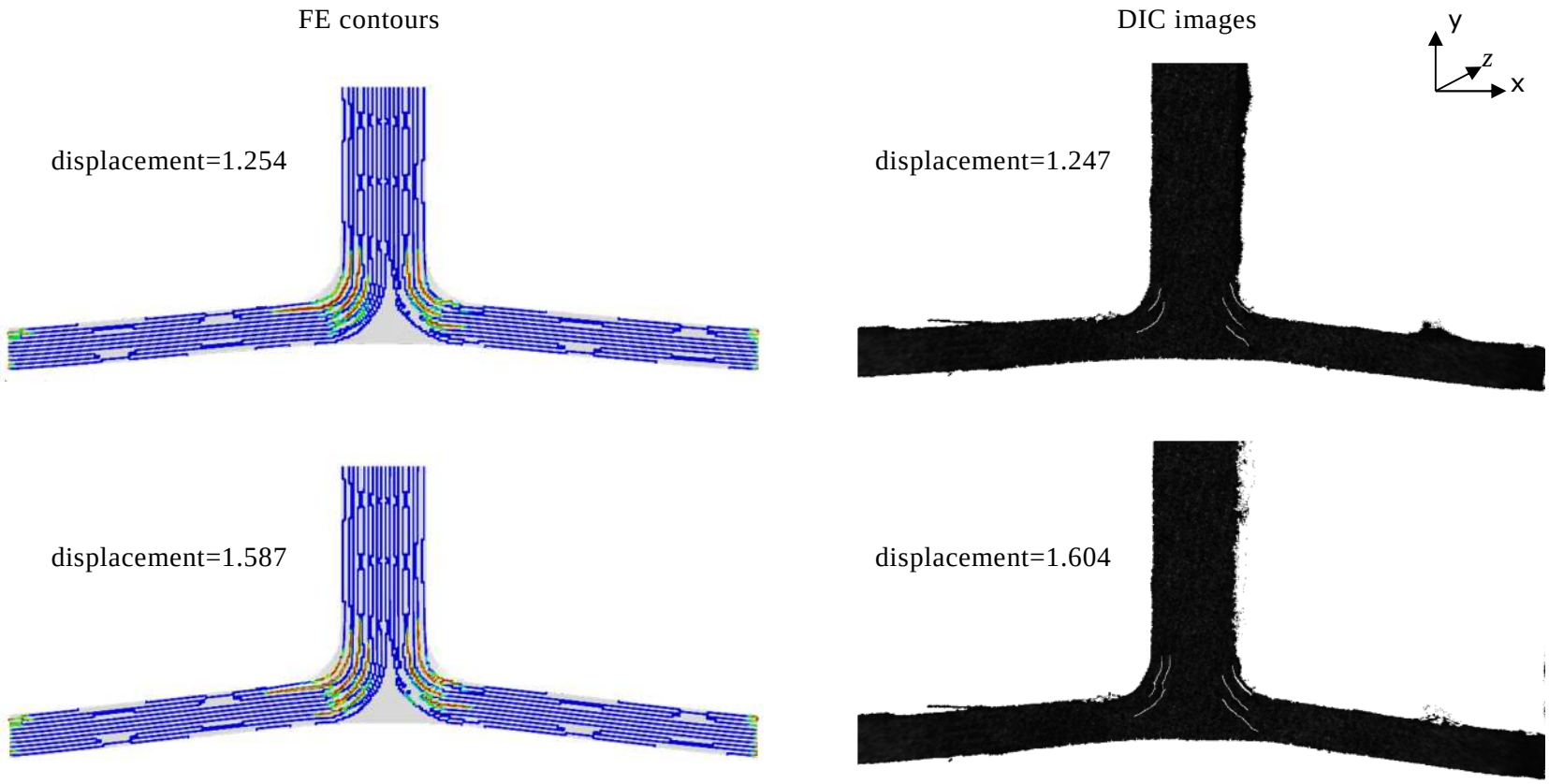


Figure 5-13 Comparison between predicted interface damage from the FE model of 3D woven type 1 specimen (left) and images taken by DIC camera showing delamination (right) during the test; the fully damaged interface elements are shown in red, the delamination locations in images taken by DIC camera are shown in white (displacement unit: mm)

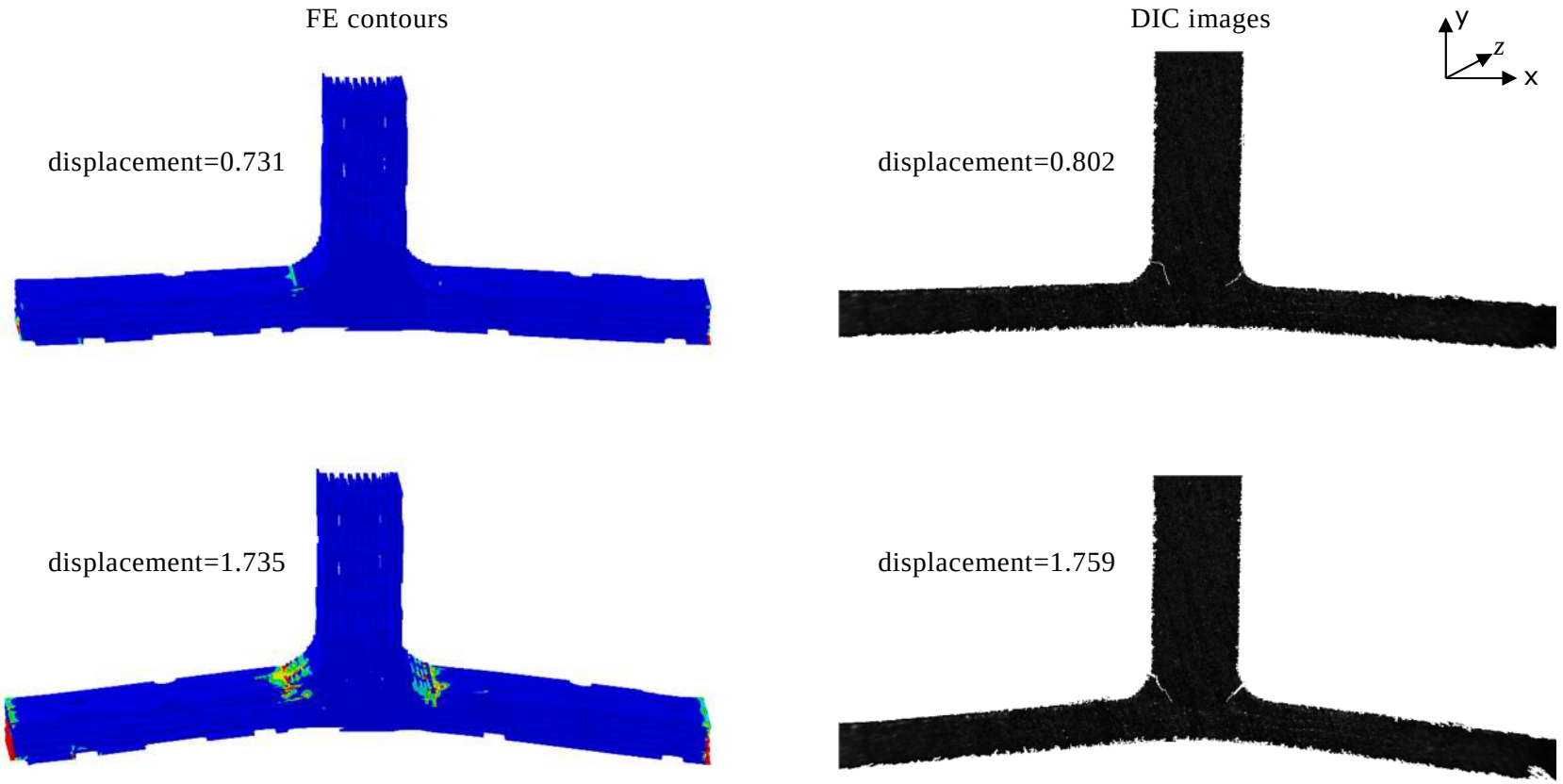


Figure 5-14 Comparison between predicted bulk matrix damage from the FE model of 3D woven type 2 specimen (left) and DIC images showing matrix cracks (right) during the test; the fully damaged matrix elements are shown in red, the matrix crack locations in DIC images are shown in white (displacement unit: mm)

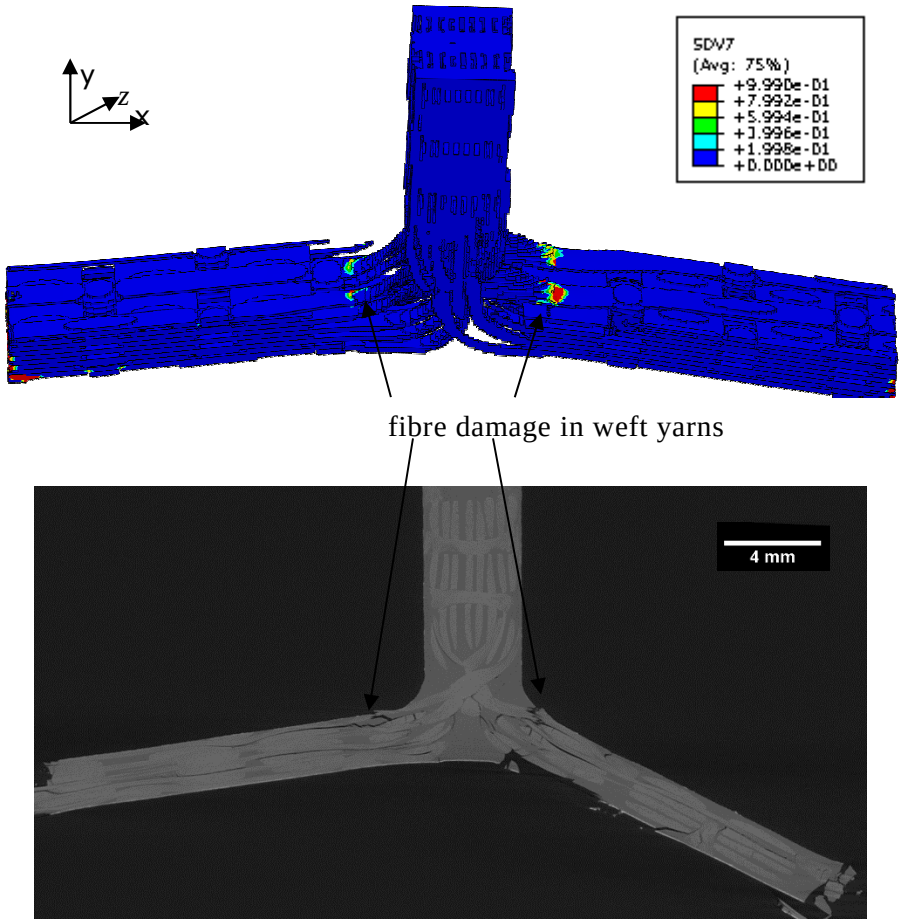


Figure 5-15 Fibre damage in the fibre direction of the weft yarns of 3D woven type 2 specimen: Top, FE prediction (matrix omitted), the fully damaged yarn elements are shown in red; bottom, µCT scan of the fractured specimen

In summary, based on the feasibility study (Chapter 4) of using a voxel mesh with a cohesive zone model (CZM), the proposed FE method successfully captured the non-linearity in the initial stiffness (Figure 2-9), and gained good agreement with the experimental load-displacement responses for the quasi-static tensile pull-off tests of the two types of 3D woven T-joint specimens. The differences in the initial failure loads and damage modes introduced by the weave variation between the two types of T-joints were predicted by the simulation. However, the proposed modelling approach could not capture the full failure process of the specimens. Catastrophic failure in FE models for

both T-joints were found at a displacement around 2 mm, which is much less than the specimens can withstand in tests (Figure 2-9). This failure was caused by fully damaged elements at the boundaries of the flange. The premature failure of the elements at the boundaries is likely to be caused by the flange boundary condition in the FE models, and further work on building the whole geometry of the flange along with contact modelling with the clamps is recommended if full failure process of the T-joints is of interest.

Besides the accurate prediction capability for the behaviour in the elastic and part of the progressive damage stages, the power of the proposed modelling method is that it does not require any model input parameter correlation with experimental results when the fibre architecture is changed at the junction. High efficiency from this voxel-based method should also be highlighted when modelling composites with complex fibre reinforcements, where conformal meshing is difficult to achieve.

5.8 Conclusions

A meso-scale modelling framework that is able to accurately predict weave architectures of 3D woven composite T-joints and the resulting mechanical behaviour under quasi-static tensile pull-off loading was proposed in this chapter. This method starts with building the meso-scale reinforcement geometries of the two types of 3D woven T-joint, based on geometric parameters of the preforms extracted from μCT analysis. Benefiting from the periodicity in the woven preform and the proposed geometric modelling strategy, construction of geometries for other weave variations is not demanding.

As modelling the physical condition in a yarn, i.e. thousands of parallel fibres impregnated with matrix, is not computationally realistic, the yarns in the woven composites were considered as homogenized UD composites with corresponding intra-yarn V_f calculated by matching the overall V_f of the

composites in each direction. The properties of the yarns were calculated by empirical methods instead of micro-scale FE analysis.

To avoid conservative or inaccurate predictions, the damage modes considered in the modelling framework should cover all the potential failure events for the composite. In this study, damage modelling incorporated yarn/matrix interface damage, governed by the CZM method, and damage in bulk matrix and homogenized yarn materials, evaluated by pressure dependent modified von Mises criterion and Hashin's failure criteria respectively. After damage initiation, the behaviour of the damaged constituent materials was modelled by a continuum damage mechanics approach, which degrades the moduli of the damaged constituent materials based on a phenomenological law.

The predicted results were in good agreement with experimental data for both 3D woven T-joints. The non-linearity in the initial stiffness was successfully captured after delamination was accounted for in the modelling framework. The differences in the initial failure loads and damage modes introduced by the weave variation between the two types of T-joints were predicted by the simulation and were consistent with experimental observations from the DIC and μCT analysis. However, premature catastrophic failure for the two models was found in elements at the boundary of the flange and this is likely to be caused by the simplification of the boundary conditions to reduce the model size in the simulation.

Based on the study from Chapter 4, the proposed method is able to model delamination based on the voxel mesh technique, which is advantageous in meshing. More significantly, it does not require any model input parameter correlation with experimental results when the fibre architecture is changed at the junction, i.e. the same material and interface properties were used in the FE models for the two types of T-joint. Consequently, new weave patterns of the 3D woven T-joints can be virtually tested under the same loading case by this modelling method to understand the effects of weave variations on the

mechanical performance.

Chapter 6 Exploration of optimum weave pattern for 3D woven T-joint reinforcements

6.1 Introduction

The design space of 3D woven composites, specifically for those with geometric features, is very large as the design is no longer only limited to ply orientations and thicknesses, but also a wide range of weave patterns in their 3D architectures. In addition, the significant differences in the resulting mechanical properties, as found between the two types of 3D woven T-joint in Chapter 2, further illustrate the challenges for designing an optimum 3D woven reinforcement.

This chapter aims to understand the effects of 3D reinforcement architecture on mechanical behaviour of 3D woven T-joints under tensile pull-off loading through a parametric study, and accordingly develop a philosophy for designing the optimum 3D woven T-joint reinforcement. Based on the prerequisite of not modifying the weaving machine for producing the two types of T-joint specimens tested in Chapter 2, it first explores other possible weave variations for the 3D woven T-joint reinforcements. Variations are restricted to the junction region of the T-joint as this was shown to be the critical region. This restriction on the weave patterns maintains a quasi-constant fibre volume fraction in the composites and new preforms can be readily woven by opening different sheds when inserting the weft yarns. Newly designed T-joint models are evaluated using the same procedure as proposed in Chapter 5 for simulating the quasi-static tensile pull-off test, and results are compared with those of the two 3D woven T-joint models in the previous chapter to relate variability of mechanical responses to weave variations. Finally, a design optimisation

philosophy for 3D woven T-joint reinforcements under tensile pull-off loading is given.

6.2 Weave pattern exploration

As introduced in Chapter 2, the two types of 3D woven T-joint preform were woven on the same weaving machine by opening different sheds when inserting the weft yarns at the junction, whilst maintaining a constant orthogonal weave pattern in the web and flange sections of the preforms, which consequently changed the path of weft yarns at the junction only. Thus, without changing any other parameters, new weave patterns for this T-joint were generated by varying the path of each of the 10 weft yarns at the junction, which is controlled by the formed sheds among the warp yarns, This restriction on the weave pattern variations does not change the fibre volume fraction of the composites and assures that no modification on the setup of the weaving machine is needed. In addition, the predicted results of the new weave pattern T-joints can be directly compared with those of the two types of 3D woven T-joint models analysed in the previous chapters to identify the influence of changes in weft yarn path on mechanical performance under tensile pull-off loading.

As there are approximately 3.6 million variations resulting from merely varying weft yarn path at the junction, finding the optimum weave pattern design for this 3D woven T-joint is challenging as it is hard to handle such a large amount of computations when evaluating the mechanical performance of the individual cases, even using a highly efficient optimisation algorithm. Inspired by the weave patterns of the two types of T-joint specimen, the problem is simplified here by grouping the weft yarn arrangement at the junction into three basic design variables: yarn path straightness, yarn path entanglement and yarn path cross-over. Yarn path straightness and yarn path entanglement are mutually exclusive, and are both independent of yarn path cross-over.

6.2.1 Basic design variables

6.2.1.1 Yarn path straightness

If a weft yarn stays in its own layer or parallel to its neighbouring weft yarn within the same weft yarn stack throughout the preform, i.e. from web through radius to flange, this is referred to as yarn path straightness. In this case, the weft yarns are stacked on each other in the form of a UD laminate, with an advantage of largely reduced crimp in the weft yarn path. For example, all the weft yarn in 3D woven type 1 model maintain yarn path straightness. Yarn path straightness can make the most of yarn axial modulus and therefore enable a higher effective modulus in the direction along the flange, which eventually might lead to a stiffer mechanical response in the tensile pull-off tests.

6.2.1.2 Yarn path entanglement

Contrary to yarn path straightness, when the neighbouring weft yarns are not parallel to each other throughout the preform, those yarns will be entangled together at the location where the yarn path changes, and this is referred to as yarn path entanglement (an example can be seen in the weft yarns of 3D woven type 2 model). Yarn path entanglement is defined between at least two neighbouring weft yarns. Yarn path entanglement changes the geometric feature of the weft yarns from a laminate-like to an inter-woven fibre architecture, which might be less vulnerable to failure when subjected to loading in the through-thickness direction.

6.2.1.3 Yarn path cross-over

The preform reinforcing the 3D woven composite T-joint was initially woven flat and then folded into a T shape with an equal number of weft yarns in each half of the preform. If a weft yarn does not always stay in the same half of the preform, i.e. it goes across to the other half of the preform when it comes to the flange, it is referred to as yarn path cross-over (an

example can be seen in the weft yarns of 3D woven type 2 model). Yarn path cross-over determines the fibre architecture and further influences the stress distribution around the noodle area.

6.2.2 Quantification of weft yarn path variations

After categorizing the arrangement of the weft yarns at the junction, new weave pattern variations for the T-joint can be quantified by the basic design variables introduced above. As yarn path straightness and yarn path entanglement are mutually exclusive, there are only two independent design variables for the preform, including yarn path cross-over. Consequently, quantification of a weave pattern variation can be addressed by specifying the proportions of weft yarns in the design variable categories through the following notation: (_%C, _%E/_%S), in which %C denotes the proportion of weft yarns that have yarn path cross-over; %E denotes the proportion of weft yarns that have yarn path entanglement; %S denotes the proportion of weft yarns that have yarn path straightness, and %S= 100 - %E according to mutual exclusivity.

For instance, the weave pattern for 3D woven type 1 T-joint does not have yarn path cross-over and entanglement, so it can be described as (0%C+0%E/100%S). Similarly, the weave pattern for 3D woven type 2 T-joint is denoted by (100%C+100%E/0%S), as all the weft yarns have crossed over to the other half and entangled among one another.

6.2.3 New weave patterns

6 new weave patterns for the 3D woven T-joint were designed, by varying the path of weft yarns around the noodle area. As the weave patterns for 3D woven type 1 (hereafter named 3Dv1) and 3D woven type 2 (hereafter named 3Dv2) specimens are the two endpoints of the proportion intervals of yarn path cross-over and entanglement (schematic weave patterns are

shown in Figure 6-1 with design variable proportions), the design of new weave patterns aims to decouple the two design variables, by varying only one design variable at a time, to determine the effects of each single variable on mechanical performance.

All variations were quantified by the proportions of yarn path entanglement (straightness) and yarn path cross-over. The 6 new weave patterns were named 3Dv3 to 3Dv8, and the schematic weave patterns showing the weave variations can be found in Figure 6-2 and Figure 6-3 in conjunction with their geometric models created in TexGen, which were built following the same strategy as in Section 5.3. Based on the yarn path defined in the weave patterns, the weft yarns at the junction of the TexGen models were assumed to have similar cross-sections to 3Dv1 or 3Dv2 models in terms of design variables. For examples, the weft yarns of 3Dv3 model have similar cross-sections to the 3Dv1 model as both of their weft yarns are considered as yarn path straightness. Note that a simple way to track the change of weft yarn path is to compare the numbering of the weft yarns (1 to 5, and 1' to 5') at the web with those at the flange of the preform.

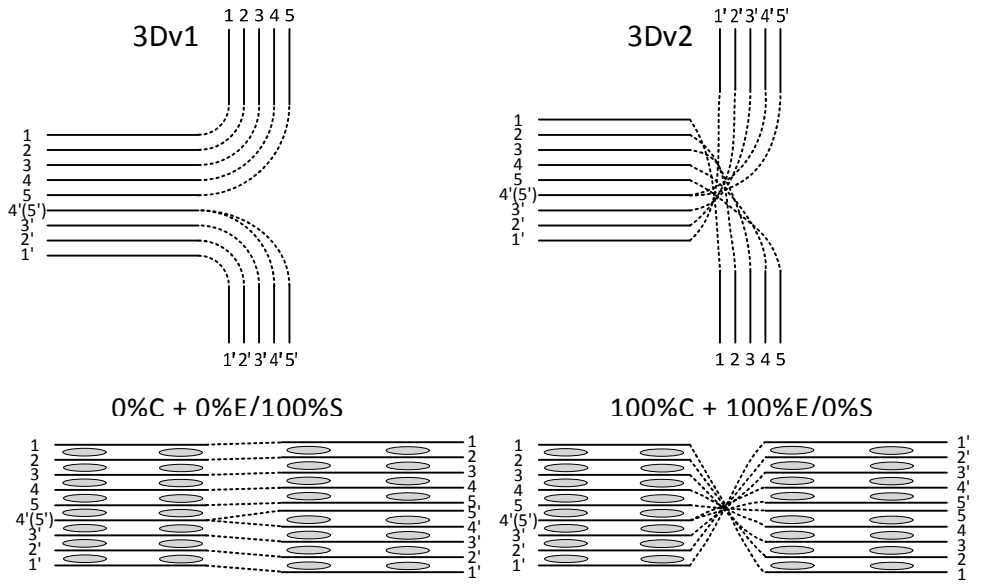


Figure 6-1 Schematic weave pattern of 3Dv1 (left), 3Dv2 (right) highlighting design variable proportions

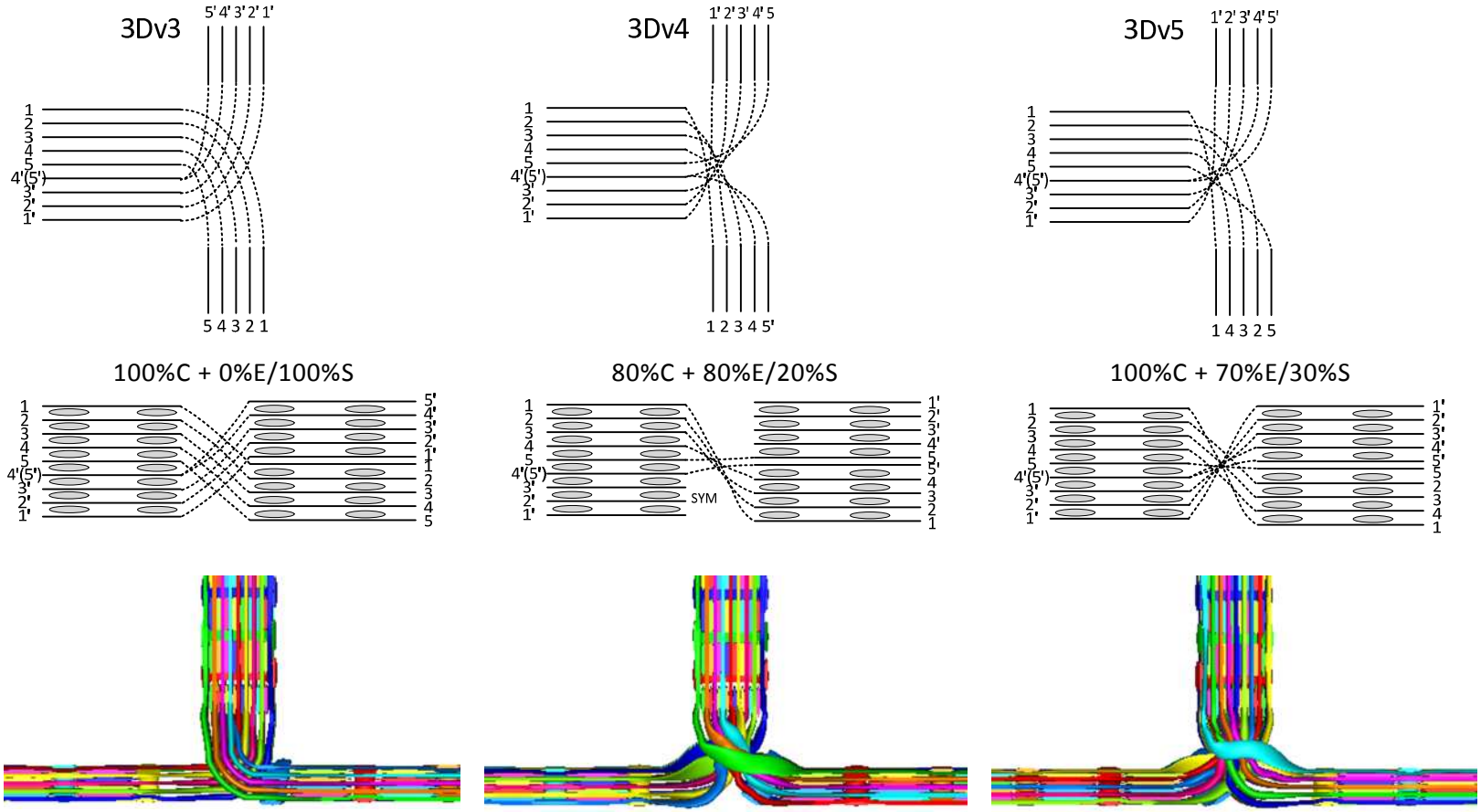


Figure 6-2 Schematic weave pattern and its geometric model of 3Dv3 (left), 3Dv4 (middle), 3Dv5 (right) T-joint models

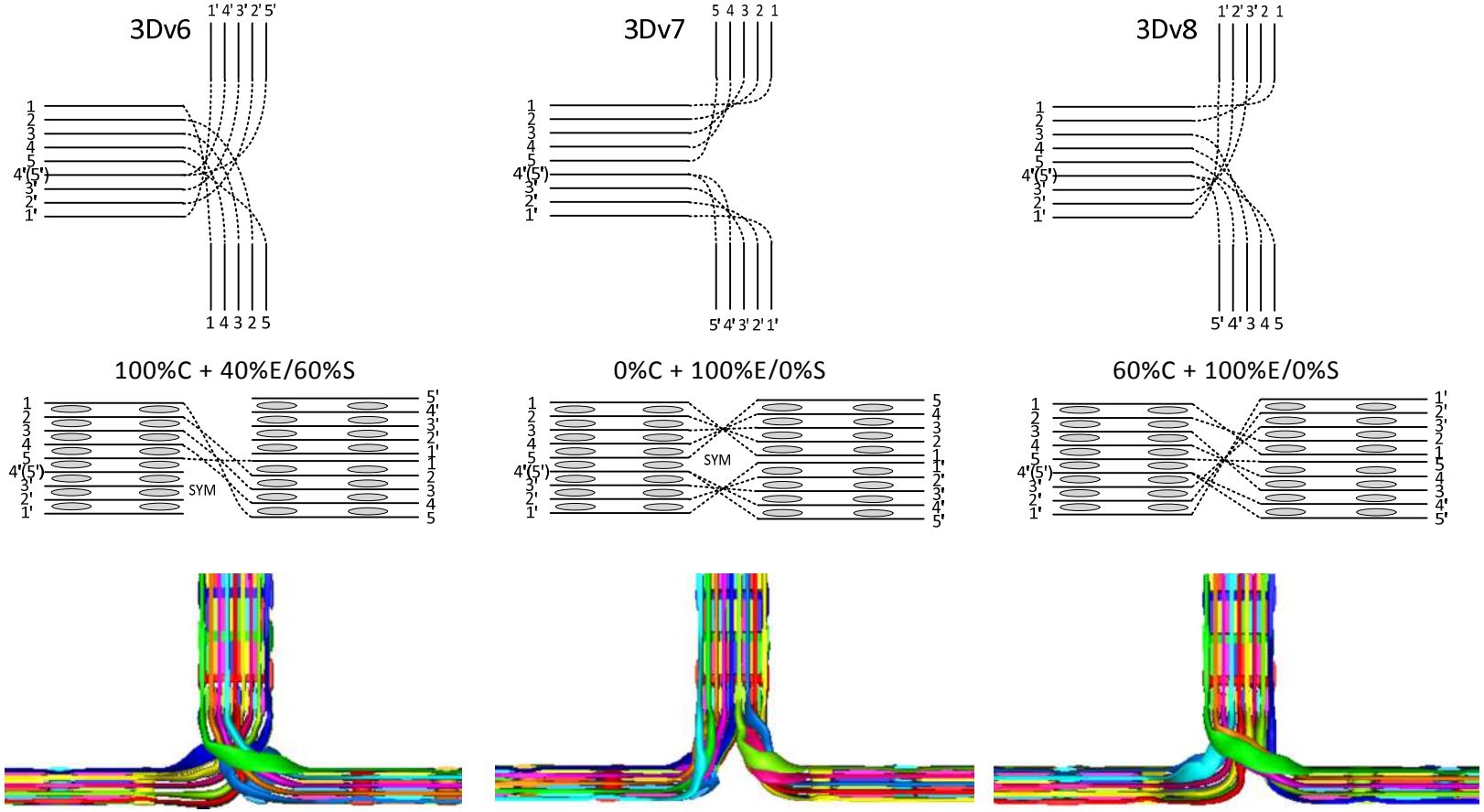


Figure 6-3 Schematic weave pattern and its geometric model of 3Dv6 (left), 3Dv7 (middle), 3Dv8 (right) T-joint models

6.3 Results

The 6 newly designed 3D woven T-joint models were numerically tested using the same procedure as proposed in Chapter 5 for simulating the quasi-static tensile pull-off test for 3Dv1 and 3Dv2 specimens, and all material properties are consistent with those used for the T-joint specimens (listed in **Error! Reference source not found.**, Table 5-4, Table 5-5; c_1=8 and c_2=13 in Eq.(5.10)). The predicted results of the 6 new 3D woven T-joint models along with those of the 3Dv1 and 3Dv2 models were compared together in terms of structural stiffness and failure load. As the proposed modelling approach could not capture the full failure process of the specimens as well as the nonlinearity in the structural stiffness, the stiffness is defined as that at a displacement of 0.35 mm, at which stage macroscopic damage has not yet initiated. The failure load is defined as an average value between 1.5 mm to 1.6 mm in displacement, to capture the effects of damage given that final failure load is likely to be unreliable as discussed in Section 5.7. An illustration for the definition of the compared structural stiffness and failure load of the T-joint models is given in Figure 6-4.

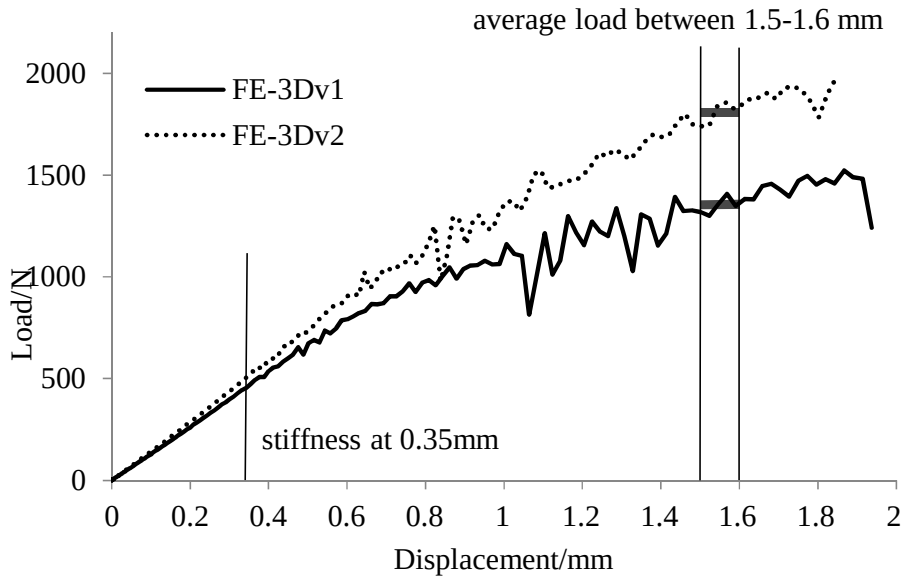


Figure 6-4 Illustration for the definition of structural stiffness and failure load for comparison of the 3D woven T-joint models

The predicted stiffnesses and failure loads of all 8 T-joint models are plotted in Figure 6-5 (Load-displacement responses for the newly design models are given in Appendix E). Distinct differences in the stiffness and failure loads are shown between these 3D woven T-joint models with only weave variations at the junction. The maximum difference in the stiffness, i.e. between 3Dv7 and 3Dv4, is 15.2%, whilst the maximum difference in the failure load, i.e. between 3Dv1 and 3Dv4, is 30%. Note that in the experiment the ultimate strength of 3Dv2 can be 100% more than that of 3Dv1. In addition, the influence of fibre architecture at the junction of the 3D woven T-joint models on stiffness is not as significant as that on failure behaviour.

The varied mechanical behaviour resulting from the variations in the fibre architectures of the 3D woven T-joint models show the performance characteristic of 3D woven composites can be tailored, which is an advantage of such materials but analysis techniques that are able to accurately predict the resulting structural performance for the 3D fibre architectures are also needed at the design stage for composite structures.

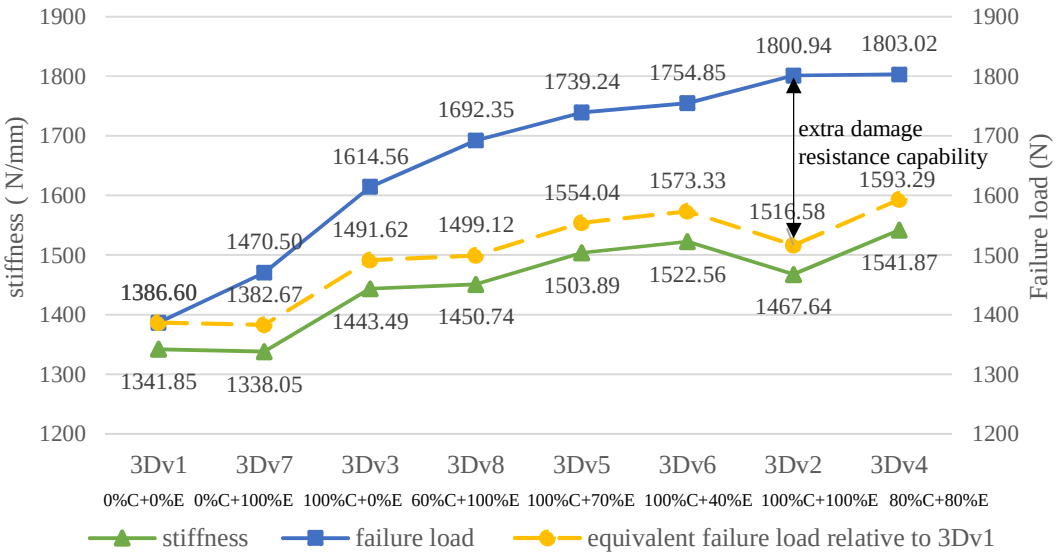


Figure 6-5 Comparison of structural stiffness and failure load of the 3D woven T-joint models

6.3.1 Damage resistance capability of the 3D woven T-joint models

As the compared failure load of each T-joint model is defined at a displacement between 1.5 mm and 1.6 mm, it thus could not accurately represent the ultimate strength of the T-joints, which is mostly dominated by the damage resistance capability as there is only a minor difference in the initial stiffness of the T-joints. At a displacement of around 1.5 mm, which is not close to that for the ultimate strength as observed in the experiments for 3Dv1 and 3Dv2, the defined failure load is still partially affected by the inherent stiffness, rather than solely reflecting the damage resistance capability. If a T-joint model is inherently stiffer but weaker (in terms of ultimate strength) than another T-joint because of the variation in the fibre architectures, the defined failure load for the stiffer but weaker T-joint model could also be higher if no catastrophic damage has occurred at the displacement between 1.5 mm and 1.6 mm, due to the elastic contribution to the failure load. In order to decouple this contribution from the defined failure load, the equivalent failure loads relative to 3Dv1 are computed for the other 7 T-joint models (Figure 6-5), which are defined by assuming they have the same damage resistance capability as 3Dv1 but retain their own stiffness as below:

$$FL_i^{equi} = \frac{ST_i}{ST_{3Dv1}} FL_{3Dv1} \tag{6.1}$$

where *FL* represents the failure load; *ST* denotes the stiffness; subscript *i* ranges from 3Dv1 to 3Dv8 denoting each T-joint model, and superscript *equi* denotes equivalent failure load to 3Dv1.

Therefore the difference between the failure load and equivalent failure load relative to 3Dv1, as illustrated in Figure 6-5, is the extra damage resistance capability with respect to 3Dv1 that the specific fibre architecture of each T-joint model offers.

It is noted that the distribution of the extra damage resistance capability of the T-joint models is roughly consistent with trend for the defined failure load, except 3Dv4 which shows a lower extra damage resistance capability than 3Dv2, after decoupling the stiffness contribution. This means that the slightly higher failure load of 3Dv4 is mostly due to its higher stiffness, and in fact it may have accumulated more damage than 3Dv2, which is likely to achieve a higher ultimate strength. Therefore, the extent of damage in terms of interface and constituent materials of each T-joint model was investigated. The interface damage is quantified by the ratio of the damaged nodes, whose damage parameter (Abaqus notation: CSDMG) is greater than 0 (Eq.(4.2)), to the total number of nodes at the interface. In addition, an interface damage ratio for damage parameter (Abaqus notation: CSDMG) greater than or equal to 0.9 (full damage occurs at the value of 1, Eq.(4.2)) is used to characterise the proportion of severely damaged interface. Meanwhile, the constituent material damage ratio is defined as the ratio of damaged matrix and yarn elements with stiffness penalty factor P (Eq.(5.10), full damage occurs at the value of 0.001) less than 1 in terms of all types of failure modes, to the total number of elements in the model. Similarly, an additional material damage ratio for P less than or equal to 0.7 is employed to evaluate the proportion of the damaged materials whose moduli have be degraded to less than or equal to 70% of the values of the intact materials. Figure 6-6 and Figure 6-7 show the comparisons of interface damage ratios and the constituent material damage ratios of the T-joint models respectively, at the same displacement of 1.57 mm (in-between 1.5 mm to 1.6 mm for the defined failure load in Figure 6-4).

Based on Figure 6-6 and Figure 6-7, the damage extent within the T-joint model appears to be able to represent the extra damage resistance capability deduced in Figure 6-5. In general, a T-joint model with lower extra damage resistance capability was shown to have higher material damage ratios and vice versa. It is also found that the damage resistance capability is collectively affected by damage at the interface and constituent materials.

For instance, although 3Dv3 had a low percentage of interfacial damage, it did not achieve a high failure load due to its high damage ratio in the constituent materials. The observation that more damage accumulated in 3Dv4 than 3Dv2 as implied from the above damage resistance analysis is validated by the damage ratios.

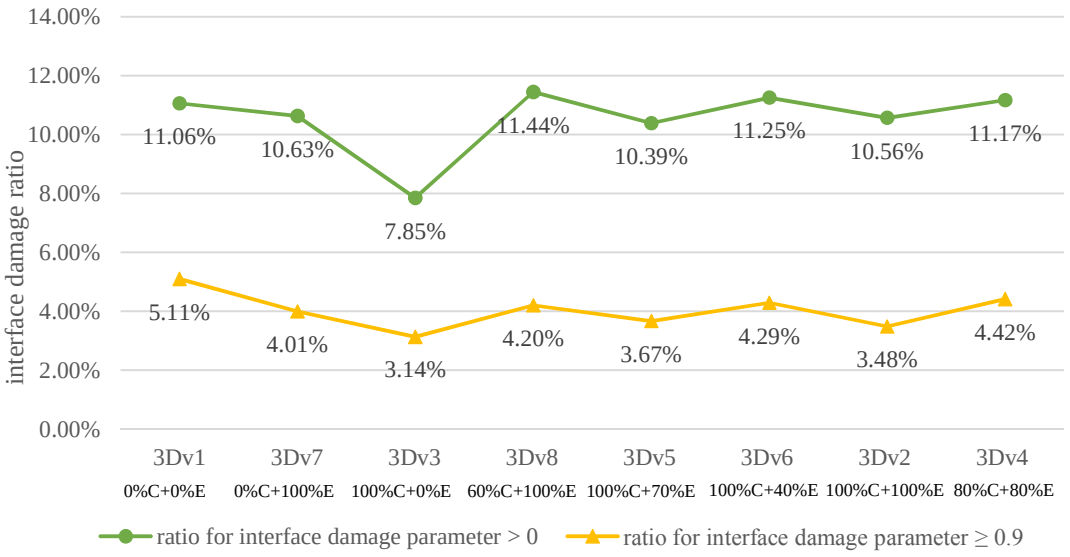


Figure 6-6 Comparison of interface damage ratios in the 3D woven T-joint models at displacement of 1.57 mm

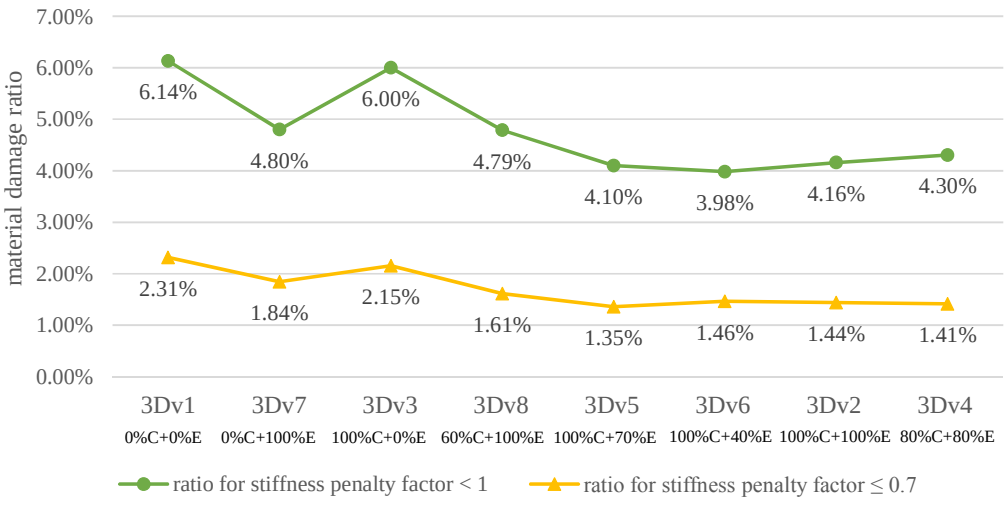


Figure 6-7 Comparison of constituent material damage ratios in the 3D woven T-joint models at displacement of 1.57 mm

It should be noted that the use of the specific damage ratios is only a method to sample the extent of damage in the T-joint models, which is difficult to quantify accurately due to the complex damage behaviour of 3D woven composites.

6.3.2 Effects of yarn path crossover on stiffness and failure load

In order to determine the effects of each single design variable on mechanical performance of the T-joint models, some of the new weave patterns were designed to have the same percentage in either of the two design variables. Through analysing the results of the T-joint models which have the same proportion of yarn path entanglement but varied proportions in yarn path cross-over, the effects of yarn path entanglement can be decoupled. Based on all 8 T-joint models, direct comparisons can be made at the yarn path entanglement proportions of 0% and 100%.

By comparing the results of 3Dv7, 3Dv8 and 3Dv2 as reproduced in Figure 6-8, which have the same proportion of yarn path entanglement at 100% but different proportions of yarn path cross-over at 0%, 60% and 100% respectively, it is found that there is a monotonic improvement in the stiffness and failure load with the increase of yarn path cross-over proportion.

Similarly, by comparing the results of 3Dv1 and 3Dv3 as reproduced in Figure 6-9, which have the same proportion of yarn path entanglement at 0%, but different proportions of yarn path cross-over at 0% and 100% respectively, an increasing trend is shown in the stiffness and failure load after improving the yarn path cross-over proportion from 0% to 100%.

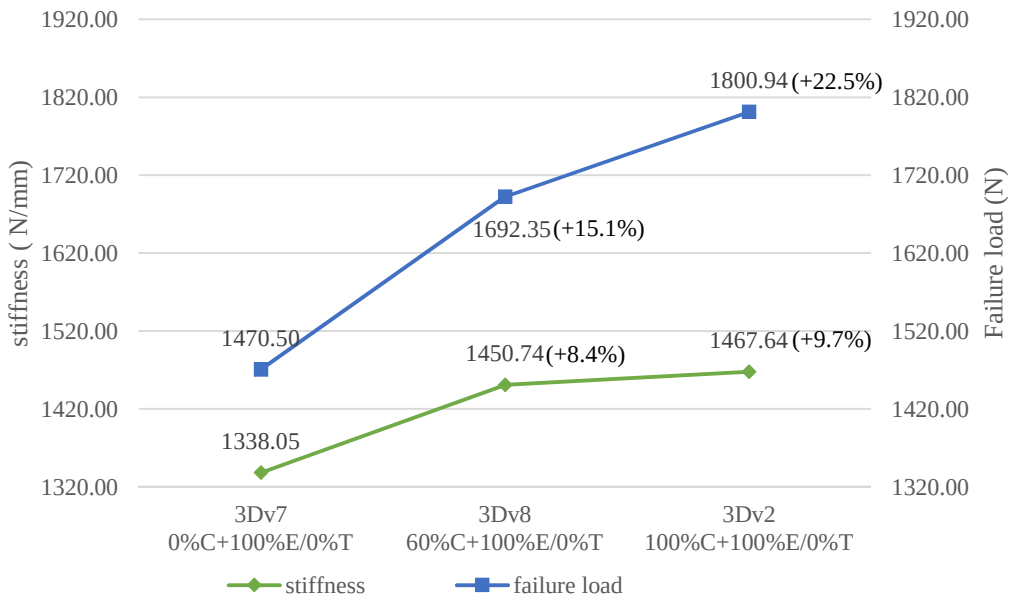


Figure 6-8 Comparison of stiffness and failure load of 3Dv7, 3Dv8 and 3Dv2 T-joint models to see the effects of yarn path cross-over at a yarn path entanglement proportion of 100%

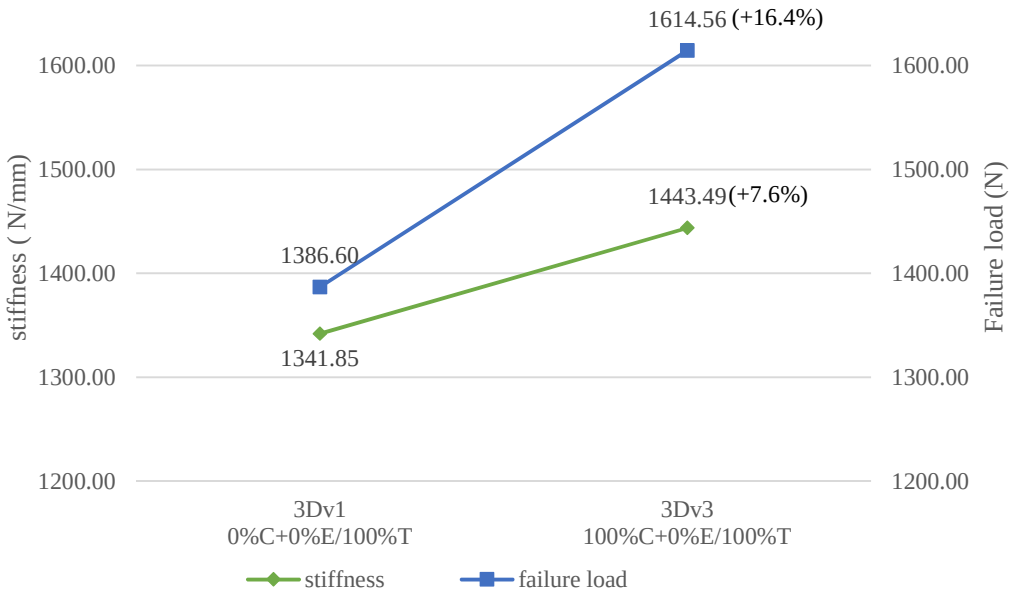


Figure 6-9 Comparison of structural stiffness and failure loads of 3Dv1 and 3Dv3 T-joint models to see the effects of yarn path cross-over at a yarn path entanglement proportion of 0%

In summary, increasing the yarn path cross-over proportion of the preforms in the 3D woven T-joints was shown to improve both stiffness and failure load under quasi-static tensile pull-off loading, when the yarn entanglement proportion is fixed at either 0% or 100%. This is because yarn path cross-over reduces the size of the noodle as seen in those models without yarn cross-over, by reinforcing it with the crossed weft yarns, which subsequently influences the stress distribution in this area so that delamination is difficult to propagate around the noodle.

6.3.3 Effects of yarn path entanglement on stiffness and failure load

Similarly, the effects of yarn path entanglement on stiffness and failure load can be found by analysing the results of the T-joint models which have the same proportion of yarn path cross-over but varied proportions in yarn path entanglement. Based on all 8 T-joint models, direct comparisons can be made at yarn path entanglement proportions of 0% and 100%.

By comparing the results of 3Dv3, 3Dv6, 3Dv5 and 3Dv2 as reproduced in Figure 6-10, which have the same proportion of yarn path cross-over at 100% but different proportions of yarn path entanglement at 0%, 40%, 70% and 100% respectively, it is shown that increasing the proportion of yarn path entanglement leads to an increase and then a decrease of stiffness, and increasing yarn path entanglement proportion leads to a quasi-monotonic increase in failure load.

By comparing the results of 3Dv1 and 3Dv7 as reproduced in Figure 6-11, which have the same proportion of yarn path cross-over at 0% but different proportions of yarn path entanglement at 0% and 100% respectively, it is observed that there is a minor decrease in the stiffness but a slight increase in the failure load after improving the yarn path entanglement proportion from 0% to 100%.

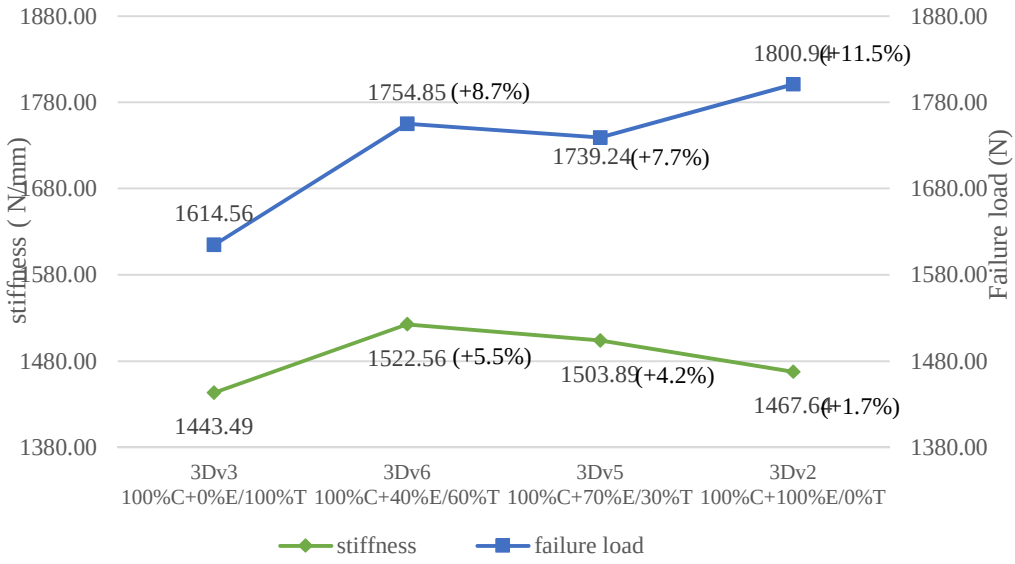


Figure 6-10 Comparison of stiffness and failure load of 3Dv3, 3Dv6, 3Dv5 and 3Dv2 T-joint models to see the effects of yarn path entanglement at a yarn path cross-over proportion of 100%

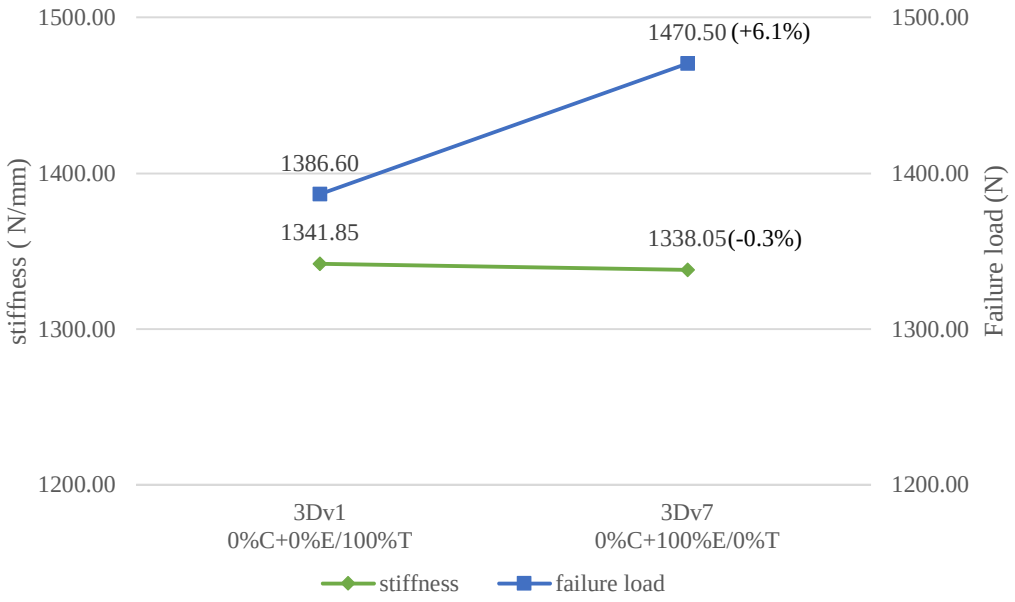


Figure 6-11 Comparison of stiffness and failure load of 3Dv1 and 3Dv7 T-joint models to see the effects of yarn path entanglement at a yarn path cross-over proportion of 0%

To conclude, a quasi-monotonic increase in the failure load was observed with the increase of the yarn path entanglement proportion, due to the entangled fibre architecture of weft yarns, in which delamination is more difficult to propagate than in a laminated structure. However, the noodle is still a critical failure area as yarn path entanglement does not reinforce the noodle, so the improvement in strength is not as significant as that obtained by increasing yarn path cross-over proportion. For instance, there was only a 6.1% increase in failure load when yarn path entanglement proportion was improved changed 0% to 100% (Figure 6-11), versus a 16.4% increase for an equivalent change in yarn path cross-over proportion (Figure 6-9). It was found that the stiffness did not always follow the increasing trend of failure load when increasing the yarn path entanglement proportion, as an optimum pattern for higher stiffness was found at a yarn entanglement ratio of about 40%, which is likely to be caused by yarn crimp introduced by further entanglement. This is supported by the fact that 3Dv4 had a higher stiffness than 3Dv2 after slightly reducing its yarn path entanglement proportion (by 20%) without a significant change in the proportion of the yarn path cross-over in the fibre architecture.

6.4 Design philosophy for 3D woven T-joint reinforcement under tensile pull-off loading

The deformation of the T-joint under quasi-static tensile pull-off loading is comprised of the tensile deformation in the web and the deflection from bending of the flange. Due to the high effective modulus in the web along its loading direction, the contribution to the deformation of the T-joint from tension in the web is negligible when compared with that from bending. The initial stiffness of the T-joint is thus largely determined by the T-joint flange in bending, and fibre architecture at the junction could have a minor impact on it. This is supported by the fact that a maximum difference of 15.2% was observed in stiffness among the 8 T-joint models, which have the same fibre architecture in the flange but varied pattern at the junction.

Conversely, the fibre architecture at the junction dominates the failure behaviour of the T-joint under the tensile pull-off testing and could lead to a step-change in the ultimate failure load by changing the failure mode, i.e. a more than 100% increase between the two different T-joint specimens tested experimentally, resulting only from the fibre architecture difference at the junction. Similar to laminated composites, the primary damage mechanism in the 3D woven composite T-joints is delamination between the bulk matrix and yarns. A typical orthogonal weave pattern for the composite T-joint, as seen in 3Dv1, can alleviate delamination by the presence of binder yarns when compared to the equivalent laminated specimen. However, if the delamination propagation is mostly arrested by further varying the fibre architecture at the junction rather than solely relying on the binders, the damage tolerance of the composites would be significantly improved.

The weft yarns take most of the loads under this specific tensile pull-off loading case. Using yarn path cross-over in the weft yarns was found to be an effective way to improve both the stiffness and failure load. It appears that the more yarn path cross-over that is introduced, the better damage resistance capability the T-joint can gain, as the noodle would be reinforced by the crossed weft yarns. The T-joint models without yarn path cross-over end up with a large noodle in the centre (e.g. 3Dv1, 3Dv7) and subsequently both performed badly in the analysis, which is consistent with a previous study showing that the noodle is a critical damage area for composite T-joints under the same loading scenario [34].

Increasing the proportion of yarn path entanglement can also improve the damage resistance capability. However, the noodle is still a critical failure region as yarn path entanglement does not change the noodle, so the damage resistance capability would not be enhanced as much as can be achieved by yarn path cross-over. On the contrary, increasing yarn path entanglement proportion leads to the reduction in the proportion of yarn path straightness

and therefore the structural stiffness would be compromised due to crimp introduced by the entangled weft yarns. Slightly reducing the yarn entanglement proportion was found to improve the stiffness of the T-joint whilst maintaining a similar failure load, which might be preferred in engineering applications.

6.5 Conclusions

To facilitate the design of 3D woven composite T-joint preforms, the effects of fibre architecture variations on mechanical performance under tensile pull-off loading were studied, based on the FE modelling framework proposed in Chapter 5. In search of the optimum fibre architecture, the study was restricted to only vary the path of weft yarns at the junction of the T-joints, as this maintains quasi-constant fibre volume fraction for the composites and does not require any modification on the weaving machine producing the preforms from that used for the two types of T-joint specimens tested in Chapter 2. A comprehensive search for the optimum preform design for the T-joint composite would require a tremendous amount of computational resources when evaluating the mechanical performance of the individuals, even using a highly efficient optimisation algorithm. Inspired by the weave patterns of the two types of T-joint specimen from earlier chapter, the problem was simplified by grouping the weft yarn arrangements into three basic design variables: yarn path straightness, yarn path entanglement and yarn path cross-over. Yarn path straightness and yarn path entanglement are mutually exclusive, hence there are only two independent design variables. Quantified by the proportions of yarn path entanglement/straightness and yarn path cross-over at the junction of the 3D woven T-joints, 6 new weave pattern variations were designed and analysed in exactly the same way as proposed in Chapter 5. By comparing the results of the new T-joint models along with those of the two types of T-joint specimens, distinct differences in the stiffness and failure loads were found resulting from the weave variations at the junction

of the T-joint.

Using yarn path cross-over in the weft yarns was found to be an effective way to improve both stiffness and failure load. It appears that the more yarn path cross-over that is introduced, the better the load carrying capability, as the noodle would be reinforced by the crossed weft yarns. A quasi-monotonic increase in the failure load was observed with the increase of yarn path entanglement proportion, due to the entangled fibre architecture of the weft yarns, in which delamination is more difficult to propagate than in a laminated structure. However, the noodle is still a critical failure area as yarn path entanglement does not change the noodle, so the improvement in strength is not as significant as that from increasing yarn path cross-over proportion. Increasing yarn path entanglement proportion leads to a reduction in the proportion of yarn path straightness and therefore the structural stiffness would be compromised due to crimp introduced by the entangled weft yarns. Following the above principles, a T-joint model, 3Dv4, with slightly reduced yarn entanglement proportion was found to achieve a higher initial stiffness whilst maintaining a similar failure load as 3Dv2 up to a displacement of around 1.5 mm, which might be preferred in engineering applications, although it might be less competitive in terms of ultimate strength.

Chapter 7 Discussion and conclusions

7.1 Introduction

This thesis is concerned with the development of modelling and design techniques for 3D woven composite T-joints, whose preforms were woven flat on a Jacquard machine with pre-positioned bifurcations, to accurately predict the resulting structural performance for 3D weave architectures, with the desire to promote the application of such structural elements in aerostructures.

The work presented can be divided into five stages: experimental testing of 3D woven composite T-joints (Chapter 2); geometric modelling of the 3D woven preform (Chapter 3); modelling approach for yarn/matrix delamination based on meso-scale voxel method (Chapter 4); development of FE modelling framework for the 3D woven composite mechanical properties (Chapter 5); weave pattern optimisation for the 3D woven T-joint preform (Chapter 6).

The experimental testing in Chapter 2 identified the effects of fibre architecture of the 3D woven T-joints on mechanical properties, and provided experimental data for validation of the FE models proposed in Chapter 5. The proposed geometric models in Chapter 3 aimed to improve the accuracy of the preform geometry in meso-scale models, and the methodology in Chapter 4 overcame the current meshing problem in delamination modelling for composites with complex fibre architecture, both of which laid the foundation for the meso-scale FE modelling framework in Chapter 5. Based on the proposed predictive modelling method, Chapter 6 investigated the effect of fibre architecture on mechanical performance and subsequently proposed a design philosophy

for 3D woven T-joint reinforcements.

This chapter discusses the essential findings of the work in this thesis, draws major conclusions and makes recommendations for future work.

7.2 Discussion

Experimental testing of 3D woven T-joints

The mechanical behaviour of two types of 3D woven T-joint with only weave variation at the junction were evaluated under a quasi-static tensile pull-off test, along with one type of 2D woven T-joint for comparison. The advantages of 3D woven composite T-joints in terms of ultimate strength and damage tolerance over the 2D alternative were shown in the testing. More importantly, this work showed that variation in the fibre architecture can change the failure mechanisms of the T-joint and can considerably enhance properties such as delamination resistance, damage tolerance and total energy absorption to failure, as well as increasing slightly in the stiffness and initial failure load. This experimental assessment has demonstrated that using 3D woven reinforcements is an effective way to improve the load bearing capability of composite T-joints over laminates, and also that this improvement could be optimised with regard to fibre architecture.

Geometric modelling for preform deformation

The prediction accuracy of the mechanical properties depends on how accurate the preform geometry is in the meso-scale models. The bifurcation process of a 3D flat woven preform for composite T-joints introduced deformation in the fibre architecture and three geometric features, yarn shifting, cross-section bending and flattening were identified by x-ray micro computed tomography (μCT) analysis. Geometric models were

proposed to approximate these deformations analytically. A simple model based on rigid body movement was used to model warp yarn shifting but the experimentally observed trend does not always agree closely with the model. The model would benefit from considering the influence of binder yarns on movement of warp yarns as well as yarn sliding induced by the weaving process, but this would complicate the model significantly. Yarn cross-section bending was modelled by a transformation of the existing parameterized description of cross-section shape instead of proposing a new shape function, and good agreement was obtained when compared with μCT results. Lastly, weft yarn flattening was described in detail and a semi-empirical model was developed to predict the flattened yarn width and satisfactory agreement with experiments was observed. However, it is worthwhile to further study the preform compaction behaviour and form a fully predictive model for yarn flattening. The proposed geometric modelling methods could be used in generating fibre architectures after forming without the need for experimental measurements, and will be implemented in TexGen for automated generation of T-joint geometries in the future.

Modelling approach for composite delamination based on voxel meshing

Based on a reduced model for the tested 3D woven composite T-joint, the use of a voxel mesh in a cohesive zone model (CZM) to model composite delamination was justified, in comparison with results from a conformal mesh, which was an open question in the previous research. The reduced T-joint composite which is only reinforced by non-crimp fabric can represent the problem of the step-like interface between the matrix and yarns in the 3D woven T-joint models whilst enabling the conformal meshing of the geometry.

An analytical expression based on conformal interface for estimating the

minimum interface stiffness applicable in textile composites was developed, based on mode I delamination, whose selection was initially empirical or based on correlation with experimental results. This work is an extension to a previous empirical method which is only applicable in laminated composites. Through analytical investigation of the effect of voxel mesh interface on structural stiffness in terms of elastic loading and damage initiation, it was found that the voxel discretisation would change the stress state at the interface and consequently the voxel model would show a stiffer behaviour than the conformal model. Numerical investigation showed that the voxel model was able to capture the peak failure load in the mixed-mode delamination analysis but overestimated the structural stiffness, compared with the results from the equivalent conformal model, which is consistent with the analytical analysis. Benefiting from the approach for estimating interface stiffness, a solution of interface stiffness scaling that enables the voxel model to have comparable accuracy with a conformal model was proposed. Through a parametric study on interface stiffness, the level of reduction in interface stiffness of the voxel model to compensate the overestimation in structural stiffness was found and was validated against experimental data in Chapter 5. The novelty of this part of work lies in the proposed interface scaling method to enable the use of a voxel mesh in a cohesive zone model, which is beneficial for modelling delamination in textile composites.

FE modelling of mechanical behaviour of 3D woven composite T-joints

Understanding the influence of the fibre architecture of 3D woven composites on their mechanical properties is fundamental to the material design phase. However, at present this is mainly dependent on experimental testing. A meso-scale modelling framework that predicts fibre architectures of 3D woven composite T-joints and the resulting mechanical behaviour under quasi-static tensile pull-off loading was proposed. Realistic meso-scale reinforcement geometries of the two types of 3D woven T-joint were

built after considering the preform deformation introduced in Chapter 2 and the yarns were considered as homogenized unidirectional (UD) composites with corresponding intra-yarn fibre volume fraction calculated by matching the overall fibre volume fraction of the composites in each direction. Note that variability in intra-yarn fibre volume fraction exists but this was not considered in the models. Micromechanical methods were used to calculate the properties of the yarns. Damage modelling incorporated yarn/matrix interface damage, governed by the CZM method, and damage in bulk matrix and homogenized yarn materials, evaluated by pressure dependent modified von Mises criterion and Hashin's failure criteria respectively. After damage initiation, the behaviour of the damaged constituent materials was modelled by a continuum damage mechanics approach, which degrades the moduli of the damaged constituent materials based on a phenomenological law.

The predicted results were in good agreement with the experimental data for both 3D woven T-joints. The non-linearity in the initial stiffness was successfully captured after delamination was accounted for in the modelling framework and interface stiffness scaling proposed in the previous chapter was employed. The differences in the initial failure loads and damage modes introduced by the weave variation between the two types of T-joints were predicted by the simulation and were consistent with experimental observations from Digital Image correlation (DIC) and μCT analyses. However, premature catastrophic failure for the two models was found in elements at the boundary of the flange and this is likely to be caused by the simplification of the boundary conditions to reduce the model size in the simulation. Being able to model delamination based on the voxel mesh technique, the proposed method is efficient. More importantly, besides the accurate prediction capability for the behaviour in the elastic and part of the progressive damage stages, the power of the proposed modelling method is that it does not require any model input parameter correlation with experimental results when the fibre architecture is changed at the junction. However, it is recommended validating the proposed model under

other loading cases to cover a full range of failure modes of the composites.

Exploration of optimum weave pattern for 3D woven T-joint reinforcements

In seeking the optimum fibre architecture, this analysis was restricted to variations to the weft yarn paths at the junction of the T-joints, as this maintains quasi-constant fibre volume fraction and does not require any modification to the weaving machine producing the preforms for T-joint specimens. This computationally demanding problem was simplified by grouping the weft yarn arrangement into three basic design variables: yarn path straightness, yarn path entanglement and yarn path cross-over, where yarn path straightness and yarn path entanglement are mutually exclusive. Six new weave pattern variations quantified by the design variable proportions were designed and analysed based on the FE modelling framework proposed and validated in Chapter 5.

Using yarn path cross-over in the weft yarns was found to be an effective way to improve both stiffness and failure load, as the noodle (resin-rich area at the junction) would be reinforced by the crossed weft yarns. A quasi-monotonic increase in the failure load was observed with increase in yarn path entanglement proportion, due to the entangled fibre architecture of the weft yarns, in which delamination is more difficult to propagate than in a laminated structure. However, the noodle is still a critical failure area as yarn path entanglement does not change this feature in the way that yarn cross-over does, so the improvement in strength is not as significant as from increasing yarn path cross-over proportion. Increasing yarn path entanglement proportion leads to a reduction in the proportion of yarn path straightness and therefore the structural stiffness would be compromised due to the crimp introduced by the entangled weft yarns. Following the above principles, a T-joint model, with slightly reduced yarn entanglement proportion was found to achieve a higher initial stiffness whilst maintaining

a similar failure load as the stronger T-joint tested experimentally up to a displacement of around 1.5 mm, which might be preferred in engineering applications, although it might be less competitive in terms of ultimate strength. However, due to the large design space for 3D woven composites, introducing an automated optimisation tool in conjunction with the proposed FE modelling framework to facilitate the design is recommended.

7.3 Conclusions

The major conclusions drawn from this thesis are summarised below:

- The mechanical performance of 3D woven composites, especially those with geometric features, was shown experimentally to be largely tailorable in terms of their fibre architecture. Limited weave variation at the junction could lead to a significant difference in mechanical performance, e.g. a more than 100% improvement in the ultimate strength, through tensile pull-off tests on two types of 3D woven composite T-joint.

- The advantages of 3D woven composites over the 2D alternative in terms of delamination resistance were demonstrated. Similar to laminated composites, delamination is still a critical failure mechanism for 3D woven composites, but it can be alleviated by the presence of through-thickness reinforcement or variation in fibre architecture.

- Three geometric features, yarn shifting, cross-section bending and flattening, caused by the bifurcation of the 3D flat woven preform for composite T-joints, were identified by μCT analysis and approximated analytically.

- It was found that voxel meshing can be used in modelling of

composite delamination in conjunction with the CZM method, but with limitation in overestimating the structural stiffness. This limitation is caused by the changed stress state at the voxel interface and it can be improved by scaling down the interface stiffness of the voxel model.

.

- Good agreement with experimental data showed that the proposed FE modelling framework offered an efficient way for predicting the mechanical performance of 3D woven composites with complex fibre architecture. It does not require any model input parameter correlation with experimental results when the fibre architecture is changed at the junction.

- Three basic design variables, i.e. weft yarn path straightness, weft yarn path entanglement and weft yarn path cross-over were adopted to simplify the large design space of 3D woven composite T-joints. Using yarn path cross-over was found to be an effective way to improve both stiffness and failure load. Increasing the proportion of yarn path entanglement can also improve the damage resistance capability. However, a high level of yarn path entanglement leads to a reduction in yarn path straightness and therefore the structural stiffness would be compromised due to the crimp introduced by the entangled weft yarns. Based on the above findings, a design optimisation philosophy for 3D woven T-joint reinforcements under tensile pull-off loading was proposed.

7.4 Recommendations for future work

A number of areas summarised below are recommended for future investigations:

- A method and algorithm for automated generation of a bifurcated T-

shaped preform geometry directly from pattern files for the weaving machine should be developed as it is required for the automated optimisation process. Preliminary work on modelling of this bifurcation process has been carried out [135].

- It would be beneficial if the developed semi-empirical geometric model for weft yarn flattening could be expanded to a predictive model, through incorporating the method for predicting yarn height under compaction and cross-section transition length.

- Variability in intra-yarn fibre volume fraction was not considered in the FE modelling framework, however, it is worthwhile to evaluate how this variability affects the accuracy of the predicted results. It should also be noted that assigning different properties to the yarn elements based on their intra-yarn fibre volume fraction would increase the computation cost.

- Catastrophic failure in FE models for both T-joints were found at a displacement of around 2 mm, which is much less than that the specimens can withstand in tests. This failure was caused by fully damaged elements at the boundaries of the flange. Premature failure of the elements at the boundaries is likely to be caused by the flange boundary condition used in the FE models, and further work on building the whole geometry of the flange in conjunction with contact modelling with the clamps is recommended if the full failure process of the T-joints is of interest.

- In seeking the optimum fibre architecture, this work simplified the design space of the weave pattern by introducing three basic design variables. New weave patterns were only quantified by the proportions of each variable. However, with the same design variable proportions, there are still a large number of possible weave

patterns, so whether the trends observed apply to other fibre architectures with similar characteristics remains unclear.

- This work tested the 3D woven T-joint specimens under tensile pull-off loading, which is one of the in-service loading conditions for such structures as discussed in Section 2.2. However, the T-joints should also be evaluated under other possible loading conditions before application.

- As the design space for 3D woven composites, especially those with geometric features, is extremely large, introducing an automated optimisation tool in conjunction with the proposed FE modelling framework to facilitate the design is recommended, which would promote large volume applications of such materials. This should be applied to other geometric features to enable their design optimisation.

References

[1] A.C. Long, *Design and manufacture of textile composites*. 2005: Elsevier.

[2] K. Bilisik, Multiaxis three-dimensional weaving for composites: A review. *Textile Research Journal*, **82**, 2012, pp. 725-743.

[3] L. Tong, A.P. Mouritz and M. Bannister, *3D fibre reinforced polymer composites*. 2002: Elsevier.

[4] *Breakthrough Aerospace Material - BAM*. [cited 2016 Dec 20]; Available from: http://gtr.rcuk.ac.uk/projects?ref=102368.

[5] *First 3D woven composite for NASA thermal protection systems*. [cited 2016 Dec 20]; Available from: https://www.nasa.gov/feature/first-3d-woven-composite-for-nasa-thermal-protection-systems.

[6] *LEAP Fan Blade*. [cited 2016 Dec 20]; Available from: http://www.albint.com /business/aec/en-us/aerospace/Pages/LEAP-Fan-Blade.aspx.

[7] *3-Dimensional Multifunctional Ablative Thermal Protection System (3DMAT)*. [cited 2016 Dec 20]; Available from: https://www.nasa.gov/ames-partnerships/technology/ technology-opportunity-multifunctional-ablative-thermal-protection-system.

[8] *787 Dreamliner Main Landing Gear Brace*. [cited 2016 Dec 20]; Available from: http://www.albint.com/business/aec/en-us/aerospace/Pages/787-Dreamliner-Main-Landing-Gear-Brace.aspx.

[9] *F35 Rolls Royce LiftFan®*. [cited 2016 Dec 20]; Available from: http://www.albint.com/business/aec/en-us/aerospace/Pages/Rolls-Royce%20LiftFan%C2%AE%20for%20F-35%20Aircraft.aspx.

[10] P. Boisse, *Composite reinforcements for optimum performance*. 2011: Elsevier.

[11] K. Sharp, A. Bogdanovich, R. Boyle, J. Brown and D. Mungalov, Wind blade joints based on non-crimp 3D orthogonal woven Pi shaped preforms. *Composites Part A: Applied Science and Manufacturing*, **49**, 2013, pp. 9-17.

[12] I. Amirul. 3D woven structures and an overview of manufacturing techniques. *4th World Conference on 3D Fabrics and Their Applications. Aachen, Germany,2012*.

[13] M. McClain and J. Goering. Overview of recent developments in 3D structures. *SME Composites manufacturing.2012*.

[14] C. McHugh. The use of recent developments in conventional weaving & shedding technology to create 3D one piece woven carbon preforms. *SAMPE conference. Baltimore MD, USA,2009.*

[15] J.A. Soden, G. Weissenbach and B.J. Hill, The design and fabrication of 3D multi-layer woven T-section reinforcements. *Composites Part A: Applied Science and Manufacturing*, **30**, 1999, pp. 213-220.

[16] S. Dai, P.R. Cunningham, S. Marshall and C. Silva, Influence of fibre architecture on the tensile, compressive and flexural behaviour of 3D woven composites. *Composites Part A: Applied Science and Manufacturing*, **69**, 2015, pp. 195-207.

[17] J. Brandt, K. Drechsler and F.J. Arendts, Mechanical performance of composites based on various three-dimensional woven-fibre preforms. *Composites Science and Technology*, **56**, 1996, pp. 381-386.

[18] B.K. Behera and B.P. Dash, Mechanical behavior of 3D woven composites. *Materials & Design*, **67**, 2015, pp. 261-271.

[19] M. Sherburn, *Geometric and Mechanical Modelling of Textiles*. 2007, University of Nottingham.

[20] F. Hélénon, M.R. Wisnom, S.R. Hallett and R.S. Trask, Numerical investigation into failure of laminated composite T-piece specimens under tensile loading. *Composites Part A: Applied Science and Manufacturing*, **43**, 2012, pp. 1017-1027.

[21] P. Stickler and M. Ramulu, Investigation of mechanical behavior of transverse stitched T-joints with PR520 resin in flexure and tension. *Composite structures*, **52**, 2001, pp. 307-314.

[22] Q.D. Yang, K.L. Rugg, B.N. Cox and M.C. Shaw, Failure in the junction region of T-stiffeners: 3D-braided vs. 2D tape laminate stiffeners. *International Journal of Solids and Structures*, **40**, 2003, pp. 1653-1668.

[23] P.B. Stickler, M. Ramulu and P.S. Johnson, Experimental and numerical analysis of transverse stitched T-joints in bending. *Composite Structures*, **50**, 2000, pp. 17-27.

[24] R.S. Thomson, P.J. Falzon, A. Nicolaidis, K.H. Leong and T. Ishikawa, The bending properties of integrally woven and unidirectional prepreg T-sections. *Composite Structures*, **47**, 1999, pp. 781-787.

[25] H.J. Phillips and R.A. Shenoi, Damage tolerance of laminated tee joints in FRP structures. *Composites Part A: Applied Science and Manufacturing*, **29**, 1998, pp. 465-

478.

[26] F. Hélénon, M.R. Wisnom, S.R. Hallett and R.S. Trask, Investigation into failure of laminated composite T-piece specimens under bending loading. *Composites Part A: Applied Science and Manufacturing*, **54**, 2013, pp. 182-189.

[27] T.M. Koh, S. Feih and A.P. Mouritz, Experimental determination of the structural properties and strengthening mechanisms of z-pinned composite T-joints. *Composite Structures*, **93**, 2011, pp. 2222-2230.

[28] T.M. Koh, S. Feih and A.P. Mouritz, Strengthening mechanics of thin and thick composite T-joints reinforced with z-pins. *Composites Part A: Applied Science and Manufacturing*, **43**, 2012, pp. 1308-1317.

[29] T.M. Koh, M.D. Isa, S. Feih and A.P. Mouritz, Experimental assessment of the damage tolerance of z-pinned T-stiffened composite panels. *Composites Part B: Engineering*, **44**, 2013, pp. 620-627.

[30] F. Bianchi, T.M. Koh, X. Zhang, I.K. Partridge and A.P. Mouritz, Finite element modelling of z-pinned composite T-joints. *Composites Science and Technology*, **73**, 2012, pp. 48-56.

[31] J.T. Vazquez, B. Castanie, J.J. Barrau and N. Swiergiel, Multi-level analysis of low-cost Z-pinned composite joints Part 2: Joint behaviour. *Composites Part A-Applied Science and Manufacturing*, **42**, 2011, pp. 2082-2092.

[32] Y.B. Park, B.H. Lee, J.H. Kweon, J.H. Choi and I.H. Choi, The strength of composite bonded T-joints transversely reinforced by carbon pins. *Composite Structures*, **94**, 2012, pp. 625-634.

[33] A.P. Mouritz, Review of z-pinned composite laminates. *Composites Part A: Applied Science and Manufacturing*, **38**, 2007, pp. 2383-2397.

[34] D.D.R. Cartié, G. Dell'Anno, E. Poulin and I.K. Partridge, 3D reinforcement of stiffener-to-skin T-joints by Z-pinning and tufting. *Engineering Fracture Mechanics*, **73**, 2006, pp. 2532-2540.

[35] R.S. Trask, S.R. Hallett, F.M.M. Helenon and M.R. Wisnom, Influence of process induced defects on the failure of composite T-joint specimens. *Composites Part A: Applied Science and Manufacturing*, **43**, 2012, pp. 748-757.

[36] A. Endruweit, P. McGregor, A.C. Long and M.S. Johnson, Influence of the fabric architecture on the variations in experimentally determined in-plane permeability

values. *Composites Science and Technology*, **66**, 2006, pp. 1778-1792.

[37] A.A. Skordos and M.P.F. Sutcliffe, Stochastic simulation of woven composites forming. *Composites Science and Technology*, **68**, 2008, pp. 283-296.

[38] S.D. Green, M.Y. Matveev, A.C. Long, D. Ivanov and S.R. Hallett, Mechanical modelling of 3D woven composites considering realistic unit cell geometry. *Composite Structures*, **118**, 2014, pp. 284-293.

[39] C.-H. Chiu and C.-C. Cheng, Weaving Method of 3D Woven Preforms for Advanced Composite Materials. *Textile Research Journal*, **73**, 2003, pp. 37-41.

[40] M. Fazeli, M. Hu bner, T. Lehmann, U. Gebhardt, G. Hoffmann, and C. Cherif, Development of seamless woven node element structures for application in integral constructions. *Textile Research Journal*, **86**, 2015, pp. 1220-1227.

[41] M. Fazeli, M. Kern, G. Hoffmann and C. Cherif, Development of three-dimensional profiled woven fabrics on narrow fabric looms. *Textile Research Journal*, **86**, 2015, pp. 1328-1340.

[42] N. Khokar, 3D-weaving: Theory and practice. *Journal of the Textile Institute*, **92**, 2001, pp. 193-207.

[43] X. Chen, L.W. Taylor and L.-J. Tsai, An overview on fabrication of three-dimensional woven textile preforms for composites. *Textile Research Journal*, **81**, 2011, pp. 932-944.

[44] A.P. Mouritz and B.N. Cox, A mechanistic interpretation of the comparative in-plane mechanical properties of 3D woven, stitched and pinned composites. *Composites Part A: Applied Science and Manufacturing*, **41**, 2010, pp. 709-728.

[45] N. Isart, B. El Said, D.S. Ivanov, S.R. Hallett, J.A. Mayugo, and N. Blanco, Internal geometric modelling of 3D woven composites: A comparison between different approaches. *Composite Structures*, **132**, 2015, pp. 1219-1230.

[46] F. Desplentere, S.V. Lomov, D.L. Woerdeman, I. Verpoest, M. Wevers, and A. Bogdanovich, Micro-CT characterization of variability in 3D textile architecture. *Composites Science and Technology*, **65**, 2005, pp. 1920-1930.

[47] M. Karahan, S.V. Lomov, A.E. Bogdanovich, D. Mungalov and I. Verpoest, Internal geometry evaluation of non-crimp 3D orthogonal woven carbon fabric composite. *Composites Part A: Applied Science and Manufacturing*, **41**, 2010, pp. 1301-1311.

[48] H. Lin, L.P. Brown and A.C. Long, Modelling and Simulating Textile Structures Using

TexGen. *Advanced Materials Research*, **331**, 2011, pp. 44-47.

[49] F. Stig and S. Hallstrom, Spatial modelling of 3D-woven textiles. *Composite Structures*, **94**, 2012, pp. 1495-1502.

[50] S.V. Lomov, A.V. Gusakov, G. Huysmans, A. Prodromou and I. Verpoest, Textile geometry preprocessor for meso-mechanical models of woven composites. *Composites Science and Technology*, **60**, 2000, pp. 2083-2095.

[51] Y. Mahadik and S.R. Hallett, Finite element modelling of tow geometry in 3D woven fabrics. *Composites Part A: Applied Science and Manufacturing*, **41**, 2010, pp. 1192-1200.

[52] G. Zhou, X. Sun and Y. Wang, Multi-chain digital element analysis in textile mechanics. *Composites science and Technology*, **64**, 2004, pp. 239-244.

[53] S.V. Lomov and I. Verpoest, Compression of woven reinforcements: A mathematical model. *Journal of Reinforced Plastics and Composites*, **19**, 2000, pp. 1329-1350.

[54] Z.-R. Chen and L. Ye, A micromechanical compaction model for woven fabric preforms. Part II: Multilayer. *Composites Science and Technology*, **66**, 2006, pp. 3263-3272.

[55] Z.-R. Chen, L. Ye and T. Kruckenberg, A micromechanical compaction model for woven fabric preforms. Part I: Single layer. *Composites Science and Technology*, **66**, 2006, pp. 3254-3262.

[56] B. Cornelissen and R. Akkerman. Analysis of yarn bending behaviour. *17th International Conference on Composite Materials (ICCM 17). Edinburgh, Scotland,2009.*

[57] T. Fast, A.E. Scott, H.A. Bale and B.N. Cox, Topological and Euclidean metrics reveal spatially nonuniform structure in the entanglement of stochastic fiber bundles. *Journal of Materials Science*, **50**, 2015, pp. 2370-2398.

[58] S.V. Lomov, D.S. Ivanov, I. Verpoest, M. Zako, T. Kurashiki, H. Nakai, and S. Hirosawa, Meso-FE modelling of textile composites: Road map, data flow and algorithms. *Composites Science and Technology*, **67**, 2007, pp. 1870-1891.

[59] E.V. Iarve, D.H. Mollenhauer, E.G. Zhou, T. Breitzman and T.J. Whitney, Independent mesh method-based prediction of local and volume average fields in textile composites. *Composites Part A: Applied Science and Manufacturing*, **40**, 2009, pp. 1880-1890.

[60] S. Nehme, A. Hallal, F. Fardoun, R. Younes, B. Hagege, Z. Aboura, M. Benzeggagh,

and F.H. Chehade, Numerical/analytical methods to evaluate the mechanical behavior of interlock composites. *Journal of Composite Materials*, **45**, 2011, pp. 1699-1716.

[61] W.-G. Jiang, S.R. Hallett and M.R. Wisnom, *Development of Domain Superposition Technique for the Modelling of Woven Fabric Composites*, in *Mechanical Response of Composites*. 2008, Springer Netherlands: Dordrecht. p. 281-291.

[62] A. Doitrand, C. Fagiano, F.X. Irisarri and M. Hirsekorn, Comparison between voxel and consistent meso-scale models of woven composites. *Composites Part A: Applied Science and Manufacturing*, **73**, 2015, pp. 143-154.

[63] C. Zhang, N. Li, W. Wang, W.K. Binienda and H. Fang, Progressive damage simulation of triaxially braided composite using a 3D meso-scale finite element model. *Composite Structures*, **125**, 2015, pp. 104-116.

[64] G. Ernst, M. Vogler, C. Hühne and R. Rolfes, Multiscale progressive failure analysis of textile composites. *Composites Science and Technology*, **70**, 2010, pp. 61-72.

[65] G. Fang, B. El Said, D. Ivanov and S.R. Hallett, Smoothing artificial stress concentrations in voxel-based models of textile composites. *Composites Part A: Applied Science and Manufacturing*, **80**, 2016, pp. 270-284.

[66] H.J. Kim and C.C. Swan, Voxel-based meshing and unit-cell analysis of textile composites. *International Journal for Numerical Methods in Engineering*, **56**, 2003, pp. 977-1006.

[67] S.K. Boyd and R. Müller, Smooth surface meshing for automated finite element model generation from 3D image data. *Journal of Biomechanics*, **39**, 2006, pp. 1287-1295.

[68] E. Potter, S.T. Pinho, P. Robinson, L. Iannucci and A.J. McMillan, Mesh generation and geometrical modelling of 3D woven composites with variable tow cross-sections. *Computational Materials Science*, **51**, 2012, pp. 103-111.

[69] S.Y. Hsu and R.B. Cheng, Modeling geometry and progressive interfacial damage in textile composites. *Journal of Composite Materials*, **47**, 2012, pp. 1343-1356.

[70] J. Chen, E. Ravey, S. Hallett, M. Wisnom and M. Grassi, Prediction of delamination in braided composite T-piece specimens. *Composites Science and Technology*, **69**, 2009, pp. 2363-2367.

[71] C.C. Chamis. Simplified composite micromechanics equations for hygral, thermal and mechanical properties. *38th Annual Conference of the Society of the Plastics Industry Reinforced Plastics/Composites. Houston, United States 1983*.

[72] *ABAQUS 6.14 Documentation*. Dassault Systèmes.

[73] X. Zeng, P. Schubel and J. Lorrillard, Modelling VARTM process induced variations on bending performance of composite Omega beams. *Composites Part A: Applied Science and Manufacturing*, **90**, 2016, pp. 371-379.

[74] E.J. Barbero, *Finite Element Analysis of Composite Materials Using Abaqus*. 2013: CRC press.

[75] A. Turon, C.G. Dávila, P.P. Camanho and J. Costa, An engineering solution for mesh size effects in the simulation of delamination using cohesive zone models. *Engineering Fracture Mechanics*, **74**, 2007, pp. 1665-1682.

[76] B. Kim and J. Nairn, Experimental verification of the effects of friction and residual stress on the analysis of interfacial debonding and toughness in single fiber composites. *Journal of Materials Science*, **37**, 2002, pp. 3965-3972.

[77] P.W. Harper and S.R. Hallett, Cohesive zone length in numerical simulations of composite delamination. *Engineering Fracture Mechanics*, **75**, 2008, pp. 4774-4792.

[78] B. Cox and Q. Yang, In Quest of Virtual Tests for Structural Composites. *Science*, **314**, 2006, pp. 1102-1107.

[79] J. Crookston, A. Long and I. Jones, A summary review of mechanical properties prediction methods for textile reinforced polymer composites. *Proceedings of the Institution of Mechanical Engineers, Part L: Journal of Materials Design and Applications*, **219**, 2005, pp. 91-109.

[80] J. Llorca, C. González, J.M. Molina-Aldareguía, J. Segurado, R. Seltzer, F. Sket, M. Rodríguez, S. Sádaba, R. Muñoz, and L.P. Canal, Multiscale Modeling of Composite Materials: a Roadmap Towards Virtual Testing. *Advanced Materials*, **23**, 2011, pp. 5130-5147.

[81] S. Li, General unit cells for micromechanical analyses of unidirectional composites. *Composites Part A: Applied Science and Manufacturing*, **32**, 2001, pp. 815-826.

[82] J.D. Whitcomb, C.D. Chapman and X. Tang, Derivation of Boundary Conditions for Micromechanics Analyses of Plain and Satin Weave Composites. *Journal of Composite Materials*, **34**, 2000, pp. 724-747.

[83] S. Li, N. Warrior, Z. Zou and F. Almaskari, A unit cell for FE analysis of materials with the microstructure of a staggered pattern. *Composites Part A: Applied Science and Manufacturing*, **42**, 2011, pp. 801-811.

[84] N.V. De Carvalho, S.T. Pinho and P. Robinson, Reducing the domain in the mechanical analysis of periodic structures, with application to woven composites. *Composites Science and Technology*, **71**, 2011, pp. 969-979.

[85] E. Obert, F. Daghia, P. Ladevèze and L. Ballere, Micro and meso modeling of woven composites: Transverse cracking kinetics and homogenization. *Composite Structures*, **117**, 2014, pp. 212-221.

[86] S. Dai and P.R. Cunningham, Multi-scale damage modelling of 3D woven composites under uni-axial tension. *Composite Structures*, **142**, 2016, pp. 298-312.

[87] P. Badel, E. Vidal-Sallé, E. Maire and P. Boisse, Simulation and tomography analysis of textile composite reinforcement deformation at the mesoscopic scale. *Composites Science and Technology*, **68**, 2008, pp. 2433-2440.

[88] N. Naouar, E. Vidal-Sallé, J. Schneider, E. Maire and P. Boisse, Meso-scale FE analyses of textile composite reinforcement deformation based on X-ray computed tomography. *Composite Structures*, **116**, 2014, pp. 165-176.

[89] N. Isart, J.A. Mayugo, N. Blanco, L. Ripoll, A. Solà, and M. Soler, Geometric model for 3D through-thickness orthogonal interlock composites. *Composite Structures*, **119**, 2015, pp. 787-798.

[90] A. Drach, B. Drach and I. Tsukrov, Processing of fiber architecture data for finite element modeling of 3D woven composites. *Advances in Engineering Software*, **72**, 2014, pp. 18-27.

[91] Z. Hashin, *The elastic moduli of heterogeneous materials*. 1960: US Department of Commerce, Office of Technical Services.

[92] V. Carvelli and C. Poggi, A homogenization procedure for the numerical analysis of woven fabric composites. *Composites Part A: Applied Science and Manufacturing*, **32**, 2001, pp. 1425-1432.

[93] P. Turner, T. Liu and X. Zeng, Collapse of 3D orthogonal woven carbon fibre composites under in-plane tension/compression and out-of-plane bending. *Composite Structures*, **142**, 2016, pp. 286-297.

[94] V. Azzi and S. Tsai, Anisotropic strength of composites. *Experimental mechanics*, **5**, 1965, pp. 283-288.

[95] O. Hoffman, The brittle strength of orthotropic materials. *Journal of Composite Materials*, **1**, 1967, pp. 200-206.

[96] S.W. Tsai and E.M. Wu, A general theory of strength for anisotropic materials. *Journal of composite materials*, **5**, 1971, pp. 58-80.

[97] A.C. Orifici, I. Herszberg and R.S. Thomson, Review of methodologies for composite material modelling incorporating failure. *Composite Structures*, **86**, 2008, pp. 194-210.

[98] A. Puck and H. Schürmann, Failure Analysis of Frp Laminates by Means of Physically Based Phenomenological Models. *Composites Science and Technology*, **58**, 1998, pp. 1045-1067.

[99] Z. Hashin, Failure criteria for unidirectional fiber composites. *Journal of Applied Mechanics-Transactions of the Asme*, **47**, 1980, pp. 329-334.

[100] C.-S. Lee, J.-H. Kim, S.-k. Kim, D.-M. Ryu and J.-M. Lee, Initial and progressive failure analyses for composite laminates using Puck failure criterion and damage-coupled finite element method. *Composite Structures*, **121**, 2015, pp. 406-419.

[101] I. Lapczyk and J.A. Hurtado, Progressive damage modeling in fiber-reinforced materials. *Composites Part A: Applied Science and Manufacturing*, **38**, 2007, pp. 2333-2341.

[102] J. Zhang, L. Zhou, Y. Chen, L. Zhao and B. Fei, A micromechanics-based degradation model for composite progressive damage analysis. *Journal of Composite Materials*, **50**, 2016, pp. 2271-2287.

[103] S. Zhong, L. Guo, G. liu, H. Lu and T. Zeng, A continuum damage model for three-dimensional woven composites and finite element implementation. *Composite Structures*, **128**, 2015, pp. 1-9.

[104] D.S. Ivanov, F. Baudry, B. Van Den Broucke, S.V. Lomov, H. Xie, and I. Verpoest, Failure analysis of triaxial braided composite. *Composites Science and Technology*, **69**, 2009, pp. 1372-1380.

[105] L. Greve and A.K. Pickett, Modelling damage and failure in carbon/epoxy non-crimp fabric composites including effects of fabric pre-shear. *Composites Part A: Applied Science and Manufacturing*, **37**, 2006, pp. 1983-2001.

[106] L.D. Zhou and Z. Zhuang, Strength analysis of three-dimensional braided T-shaped composite structures. *Composite Structures*, **104**, 2013, pp. 162-168.

[107] H. Kang, Z. Shan, Y. Zang and F. Liu, Progressive damage analysis and strength properties of fiber-bar composites reinforced by three-dimensional weaving under uniaxial tension. *Composite Structures*, **141**, 2016, pp. 264-281.

[108] C. Wang, Y. Zhong, P.F. Bernad Adaikalaraj, X. Ji, A. Roy, V.V. Silberschmidt, and Z. Chen, Strength prediction for bi-axial braided composites by a multi-scale modelling approach. *Journal of Materials Science*, **51**, 2016, pp. 6002-6018.

[109] M.J. Hinton, A.S. Kaddour and P.D. Soden, *Failure criteria in fibre reinforced polymer composites: the world-wide failure exercise*. 2004: Elsevier.

[110] A.S. Kaddour and M.J. Hinton, Benchmarking of triaxial failure criteria for composite laminates: Comparison between models of 'Part (A)' of 'WWFE-II'. *Journal of Composite Materials*, **46**, 2012, pp. 2595-2634.

[111] A.S. Kaddour and M.J. Hinton, Maturity of 3D failure criteria for fibre-reinforced composites: Comparison between theories and experiments: Part B of WWFE-II. *Journal of Composite Materials*, **47**, 2013, pp. 925-966.

[112] A.S. Kaddour, M.J. Hinton, P.A. Smith and S. Li, The background to the third world-wide failure exercise. *Journal of Composite Materials*, **47**, 2013, pp. 2417-2426.

[113] N.S. Nobeen, Y. Zhong, B.A.P. Francis, X. Ji, E.S.M. Chia, S.C. Joshi, and Z. Chen, Constituent materials micro-damage modeling in predicting progressive failure of braided fiber composites. *Composite Structures*, **145**, 2016, pp. 194-202.

[114] D. Blackketter, D. Walrath and A. Hansen, Modeling damage in a plain weave fabric-reinforced composite material. *Journal of Composites, Technology and Research*, **15**, 1993, pp. 136-142.

[115] X. Tang and J.D. Whitcomb, Progressive failure behaviors of 2D woven composites. *Journal of composite materials*, **37**, 2003, pp. 1239-1259.

[116] M. Zako, Y. Uetsuji and T. Kurashiki, Finite element analysis of damaged woven fabric composite materials. *Composites Science and Technology*, **63**, 2003, pp. 507-516.

[117] S. Murakami, Mechanical Modeling of Material Damage. *Journal of Applied Mechanics*, **55**, 1988, pp. 280-286.

[118] A. Puck and H. Schürmann, Failure analysis of FRP laminates by means of physically based phenomenological models. *Composites Science and Technology*, **62**, 2002, pp. 1633-1662.

[119] W. Ruijter, *Analysis of mechanical properties of woven textile composites as a function of textile geometry*. 2008, University of Nottingham.

[120] P. Ladèveze and G. Lubineau, An enhanced mesomodel for laminates based on micromechanics. *Composites Science and Technology*, **62**, 2002, pp. 533-541.

[121] P. Maimi, J.A. Mayugo and P.P. Camanho, A Three-dimensional Damage Model for Transversely Isotropic Composite Laminates. *Journal of Composite Materials*, **42**, 2008, pp. 2717-2745.

[122] D. Zhang, A.M. Waas and C.-F. Yen, Progressive damage and failure response of hybrid 3D textile composites subjected to flexural loading, part II: Mechanics based multiscale computational modeling of progressive damage and failure. *International Journal of Solids and Structures*, **75–76**, 2015, pp. 321-335.

[123] S. Dhiman, P. Potluri and C. Silva, Influence of binder configuration on 3D woven composites. *Composite Structures*, **134**, 2015, pp. 862-868.

[124] X.S. Zeng, L.P. Brown, A. Endruweit, M. Matveev and A.C. Long, Geometrical modelling of 3D woven reinforcements for polymer composites: Prediction of fabric permeability and composite mechanical properties. *Composites Part A: Applied Science and Manufacturing*, **56**, 2014, pp. 150-160.

[125] S. Song, A.M. Waas, K.W. Shahwan, X.R. Xiao and O. Faruque, Braided textile composites under compressive loads: Modeling the response, strength and degradation. *Composites Science and Technology*, **67**, 2007, pp. 3059-3070.

[126] M. Pankow, A. Waas, C. Yen and S. Ghiorse, Modeling the response, strength and degradation of 3D woven composites subjected to high rate loading. *Composite Structures*, **94**, 2012, pp. 1590-1604.

[127] *TexGen scripting Guide*. Available from: http://texgen.sourceforge.net/index.php/Scripting_Guide.

[128] *Altair HyperMesh 13.0*. Available from: http://www.altairhyperworks.com/product/hypermesh.

[129] *PRIME™ 20LV - EPOXY INFUSION SYSTEM*. Available from: http://www.gurit.com/prime-20lv-1.aspx.

[130] *HexTow IM7 Carbon Fiber*. [cited 2014 Jun 20]; Available from: http://www.hexcel.com/user_area/content_media/raw/IM7_HexTow_DataSheet.pdf.

[131] R.M. Caddell, R.S. Raghava and A.G. Atkins, Pressure dependent yield criteria for polymers. *Materials Science and Engineering*, **13**, 1974, pp. 113-120.

[132] S. Yan, A. Long and X. Zeng. Experimental assessment and numerical analysis of 3D woven composite T-joints under tensile loading. *20th International Conference on Composite Materials (ICCM 20). Copenhagen, Denmark,2015*.

[133] Q. Yang and B. Cox, Cohesive models for damage evolution in laminated composites. *International Journal of Fracture*, **133**, 2005, pp. 107-137.

[134] S.R. Hallett, B.G. Green, W.G. Jiang and M.R. Wisnom, An experimental and numerical investigation into the damage mechanisms in notched composites. *Composites Part A: Applied Science and Manufacturing*, **40**, 2009, pp. 613-624.

[135] L.P. Brown, S. Yan, X. Zeng and A.C. Long. Mesoscale geometric modelling of bifurcation in 3D woven T-beam preforms. *12th International Conference on Textile Composites*. *Raleigh, NC, USA,2015*.

Appendix A. The design of RTM mould for the T-joint specimens

As shown in Figure A-1, the mould consists of two aluminium angles, one plate, two spacers, one picture frame and six fasteners. One resin inlet is on the top of the mould and two outlets are located at each side of the aluminium angle.

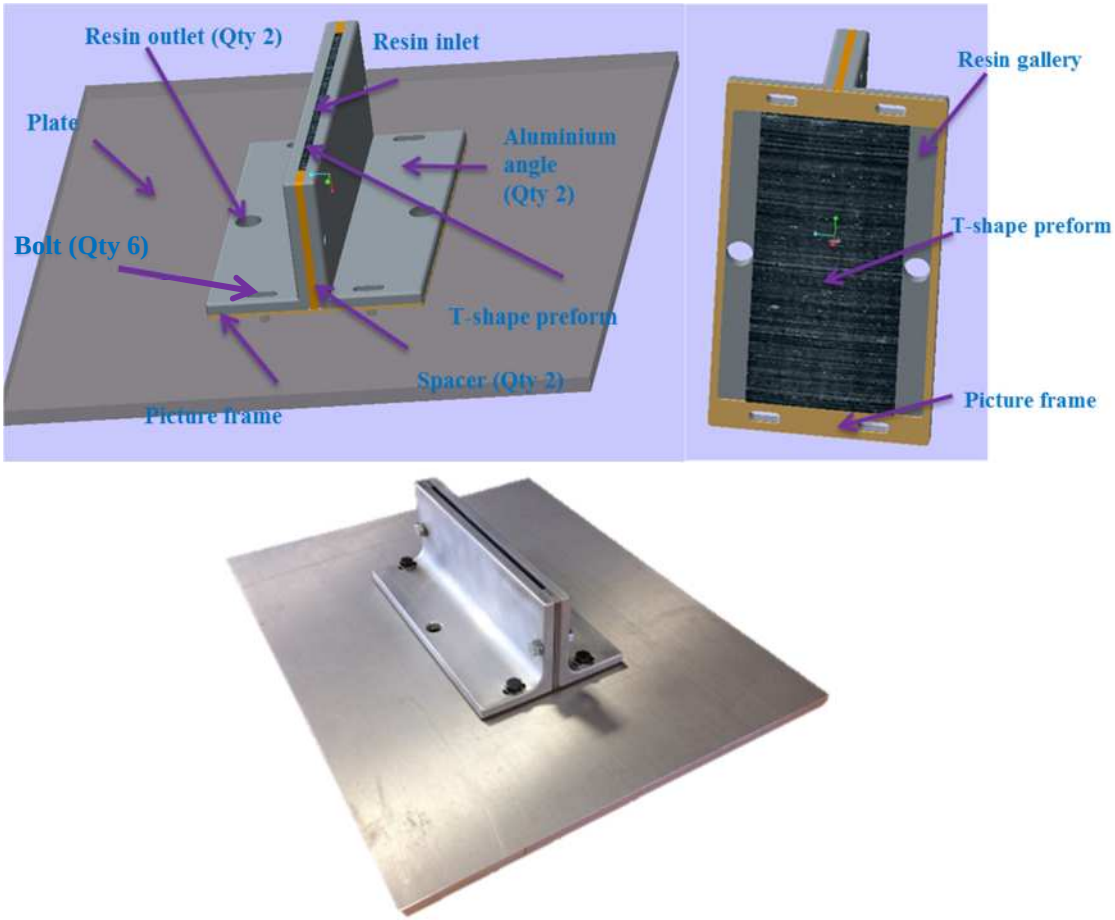


Figure A-1 Vacuum-assisted RTM mould for T-joint specimens: top, CAD model; bottom. mould assembly

In addition, the 2D drawings for the mould components are presented in Figure A-2 to Figure A-5.

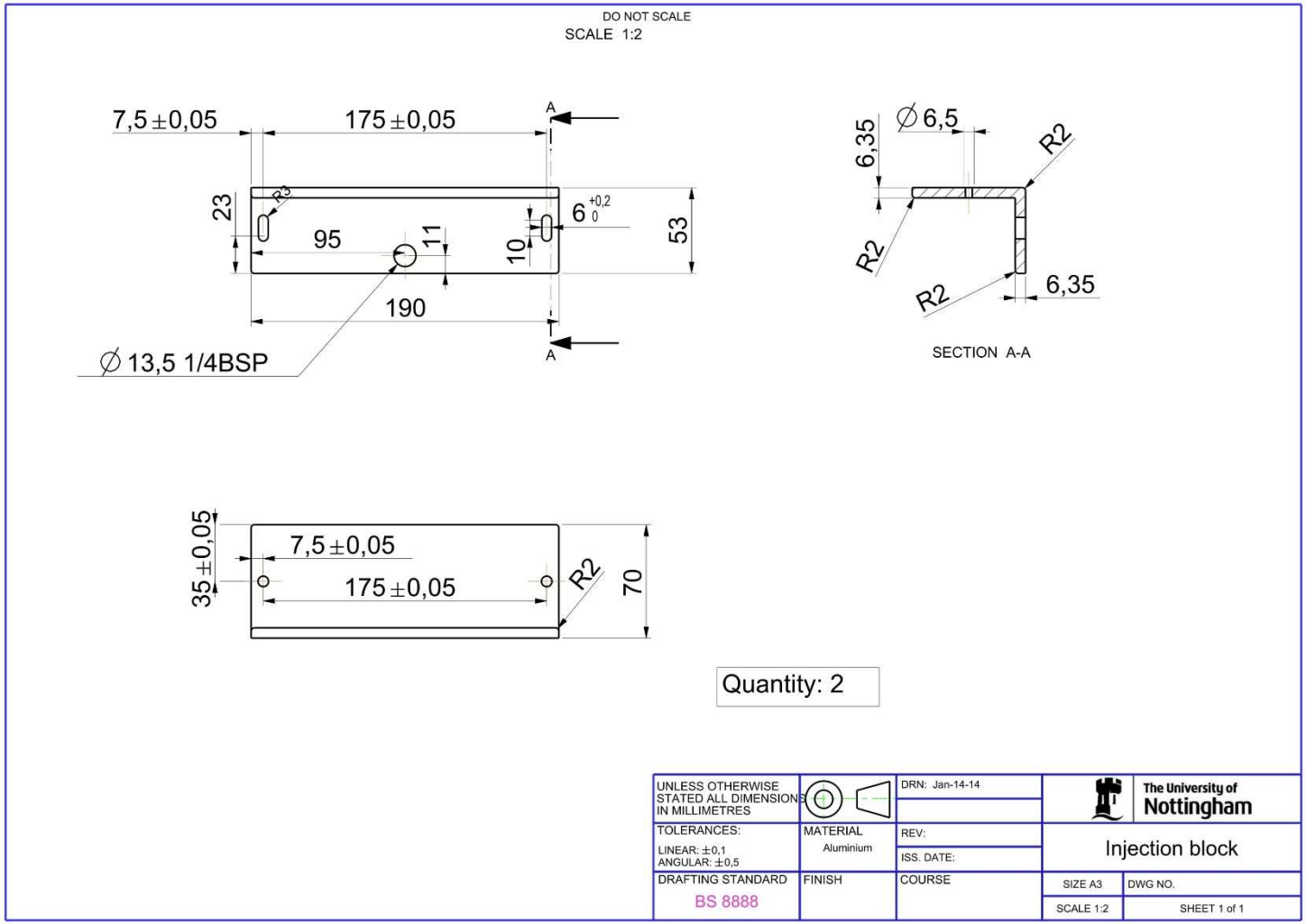


Figure A-2 2D drawing for the T-joint mould (aluminium angle)

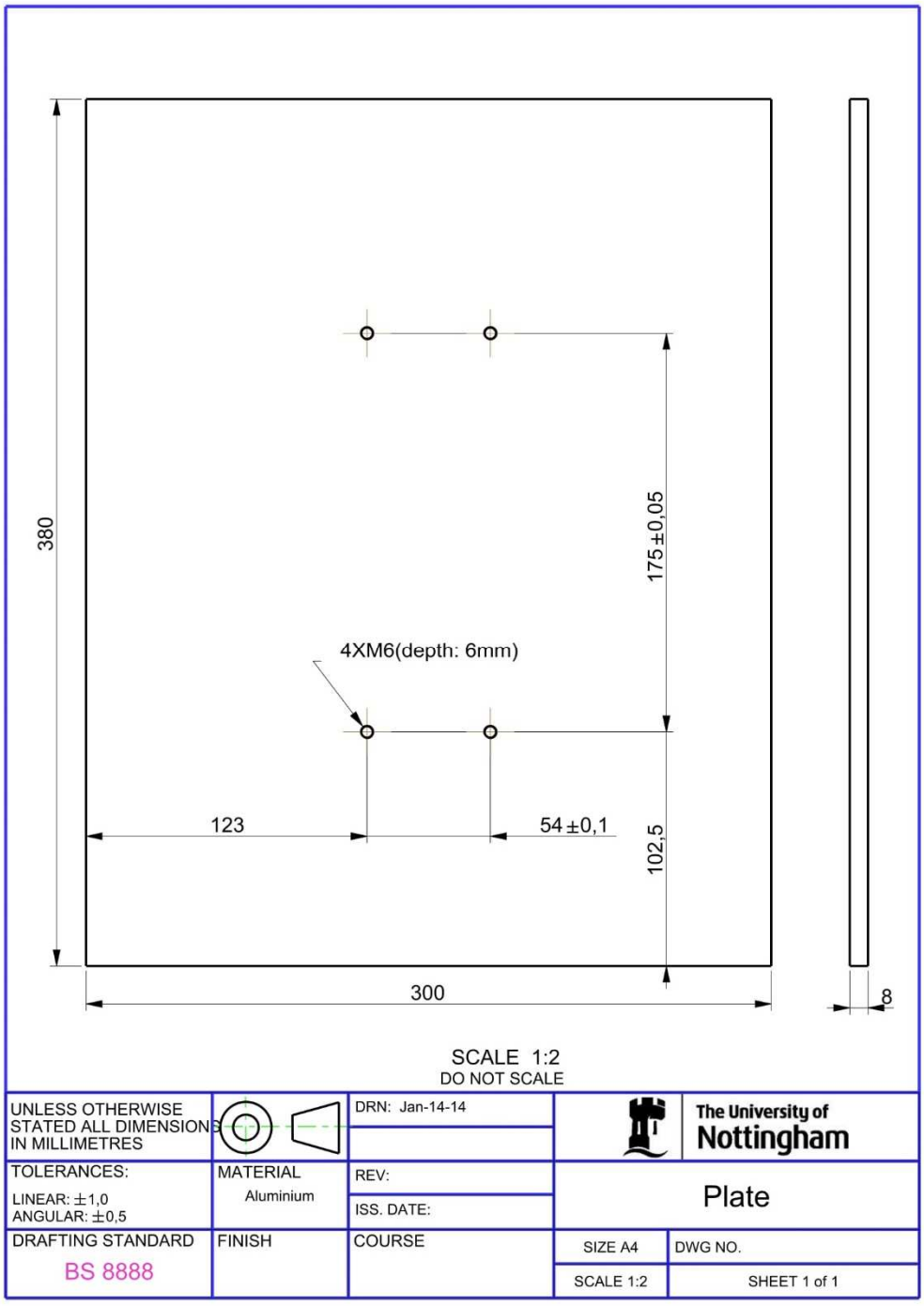


Figure A-3 2D drawing for the T-joint mould (plate)

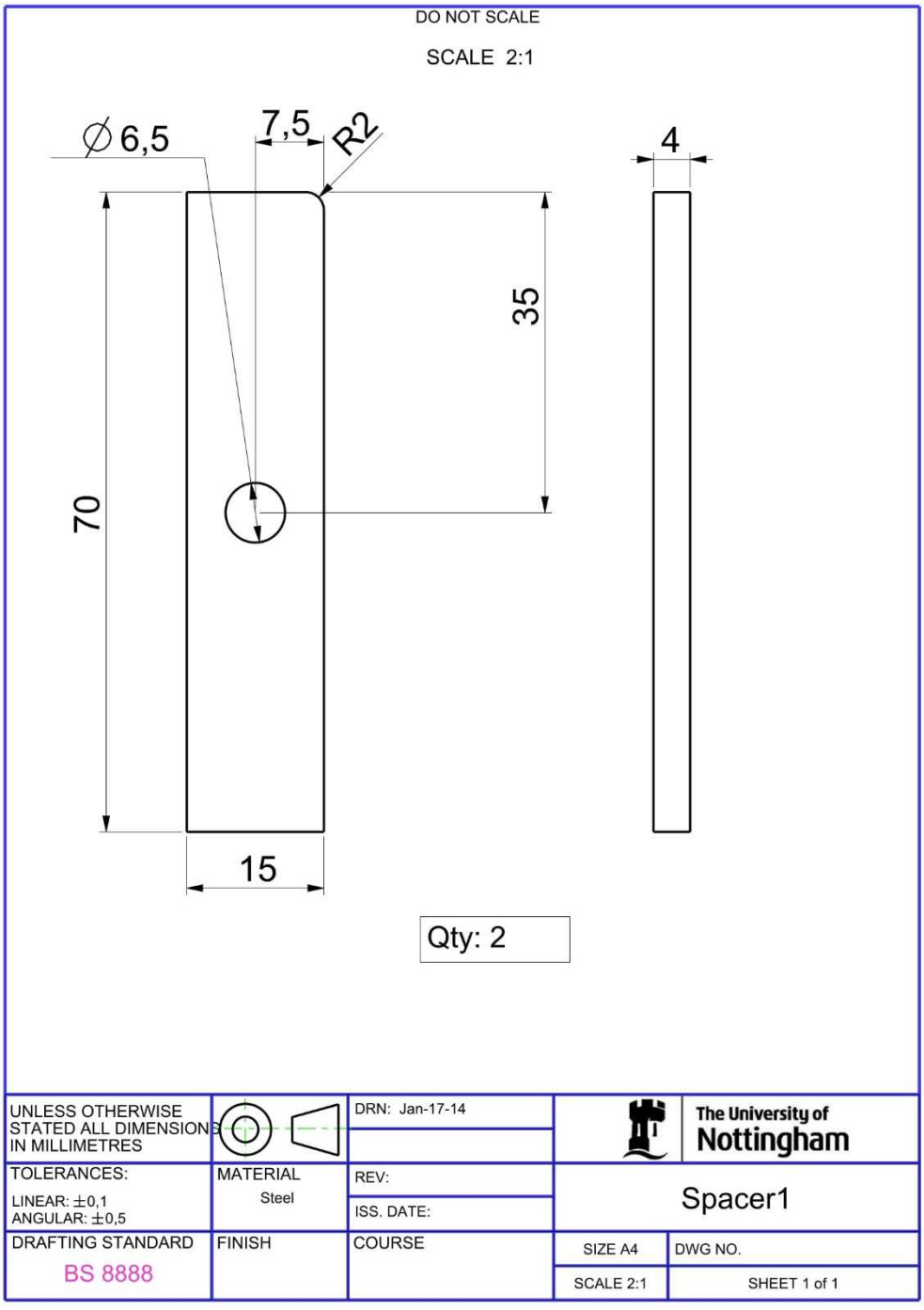


Figure A-4 2D drawing for the T-joint mould (spacer)

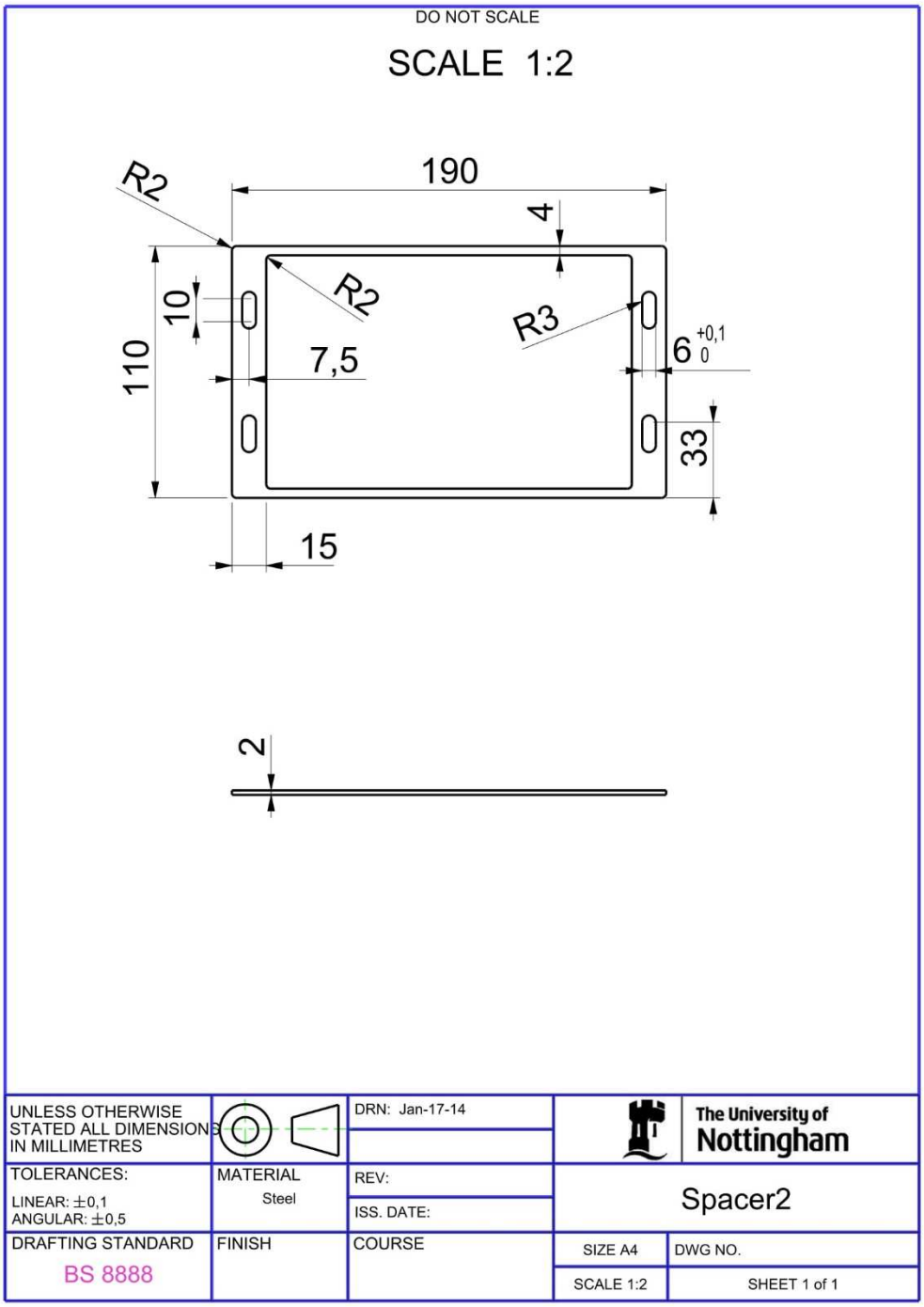
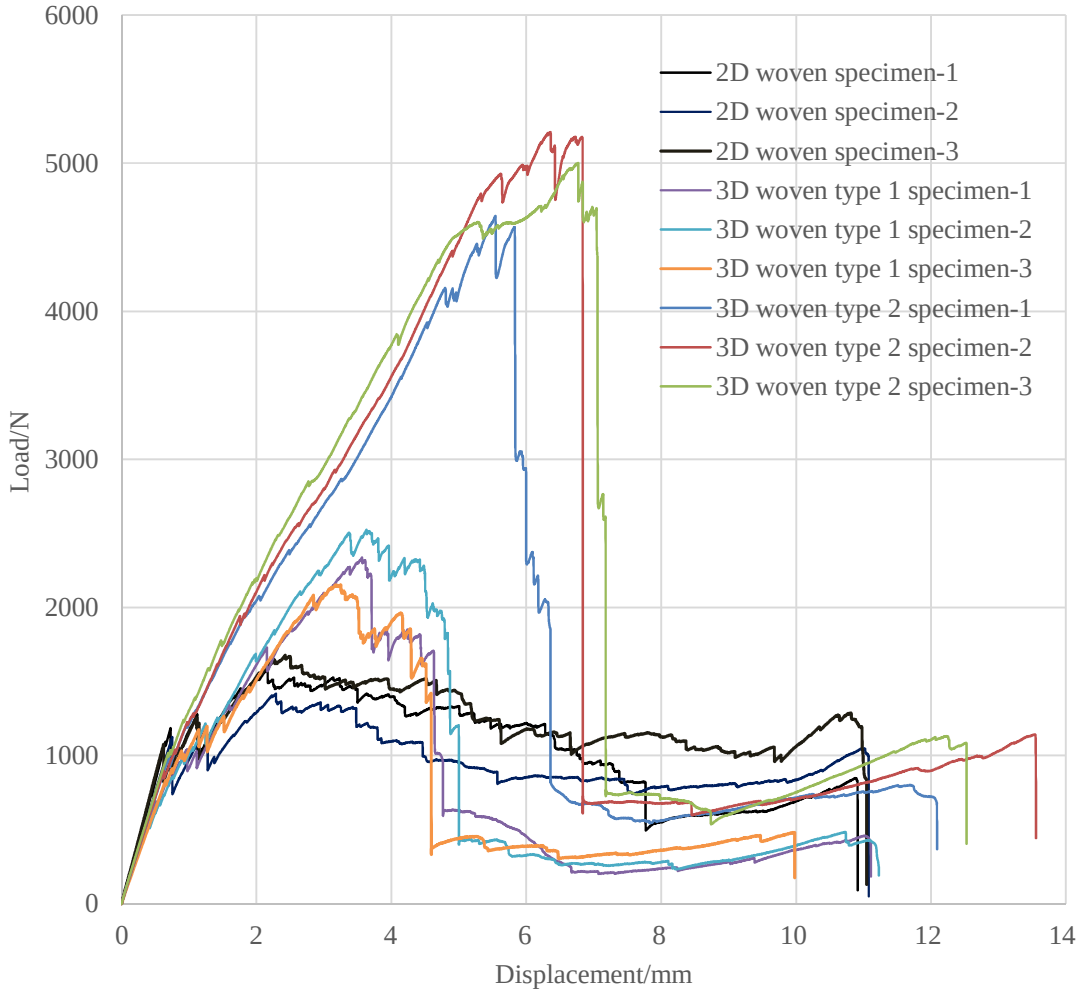


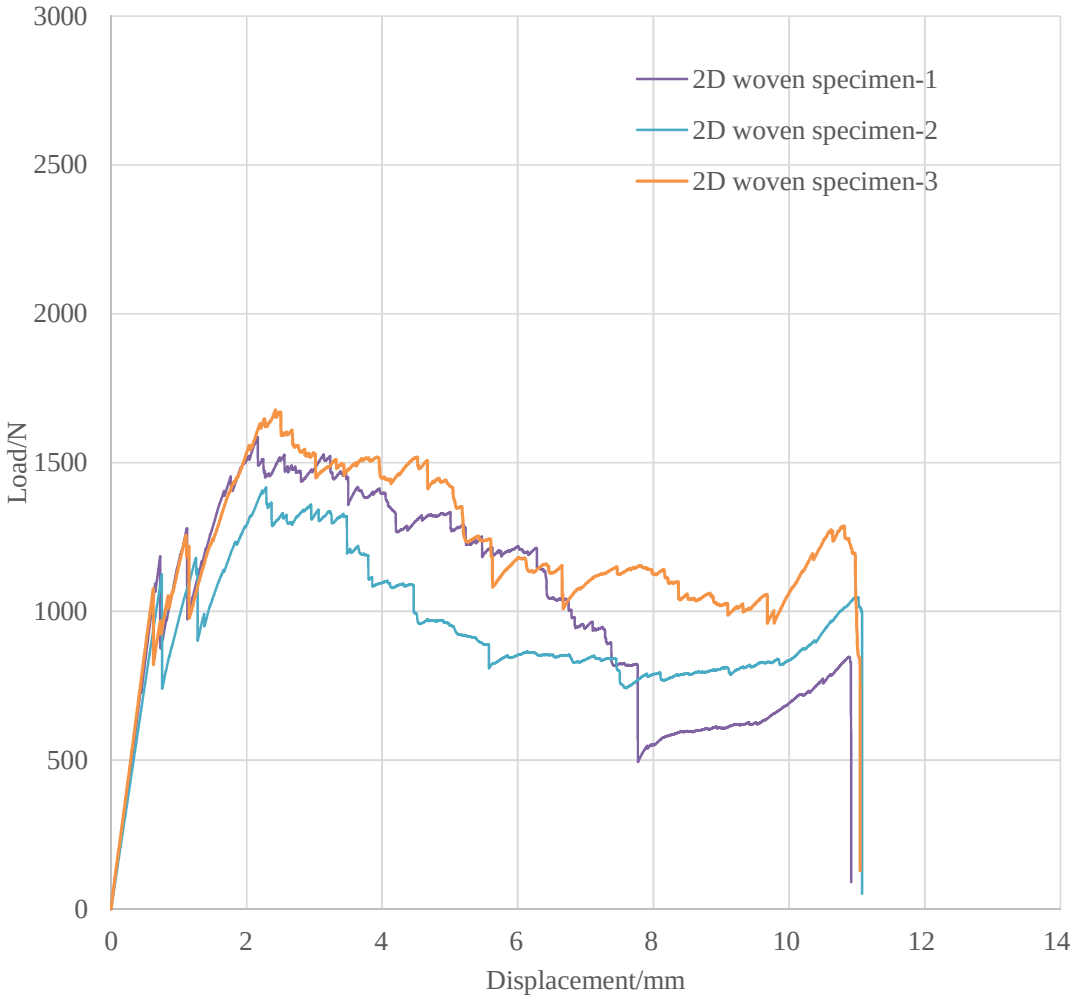
Figure A-5 2D drawing for the T-joint mould (picture frame)

Appendix B. Results of mechanical testing for T-joint specimens

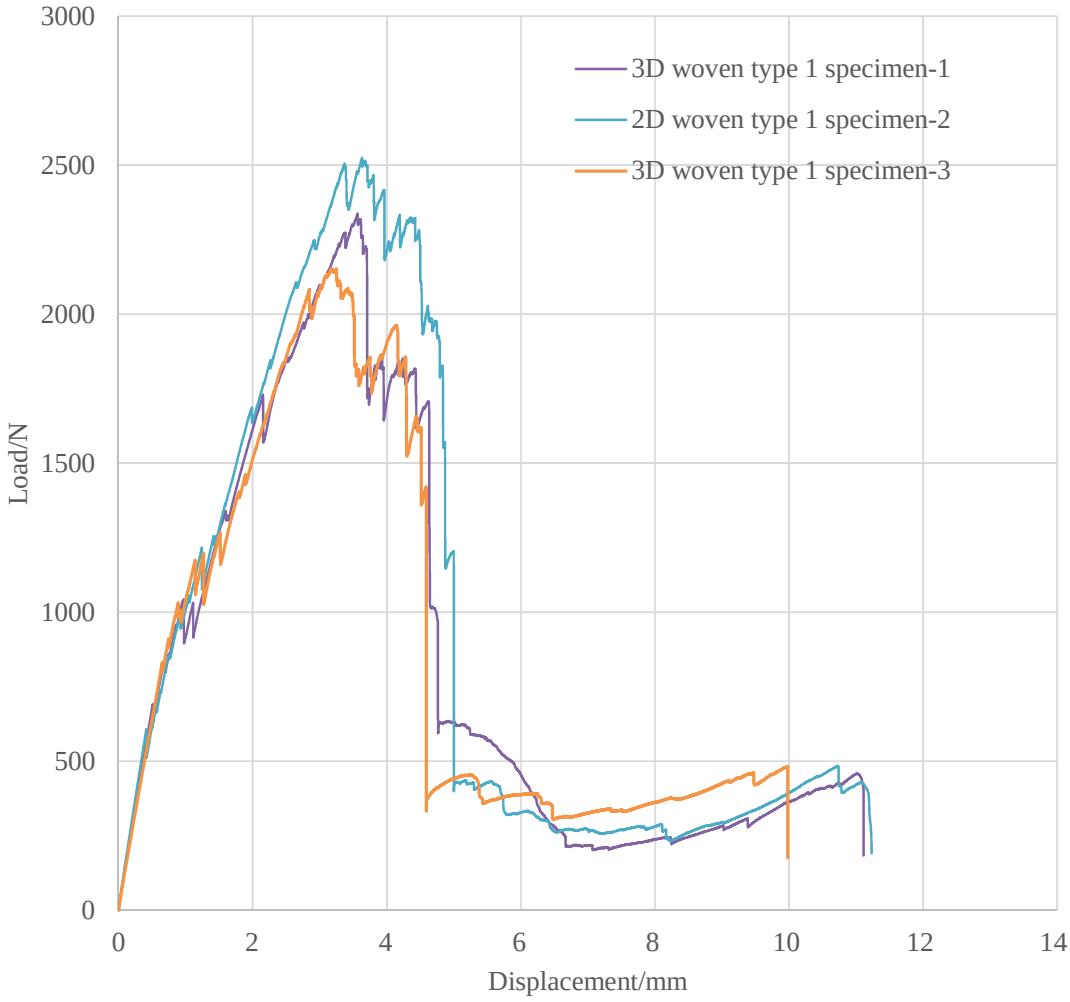
Results of all tested specimens:



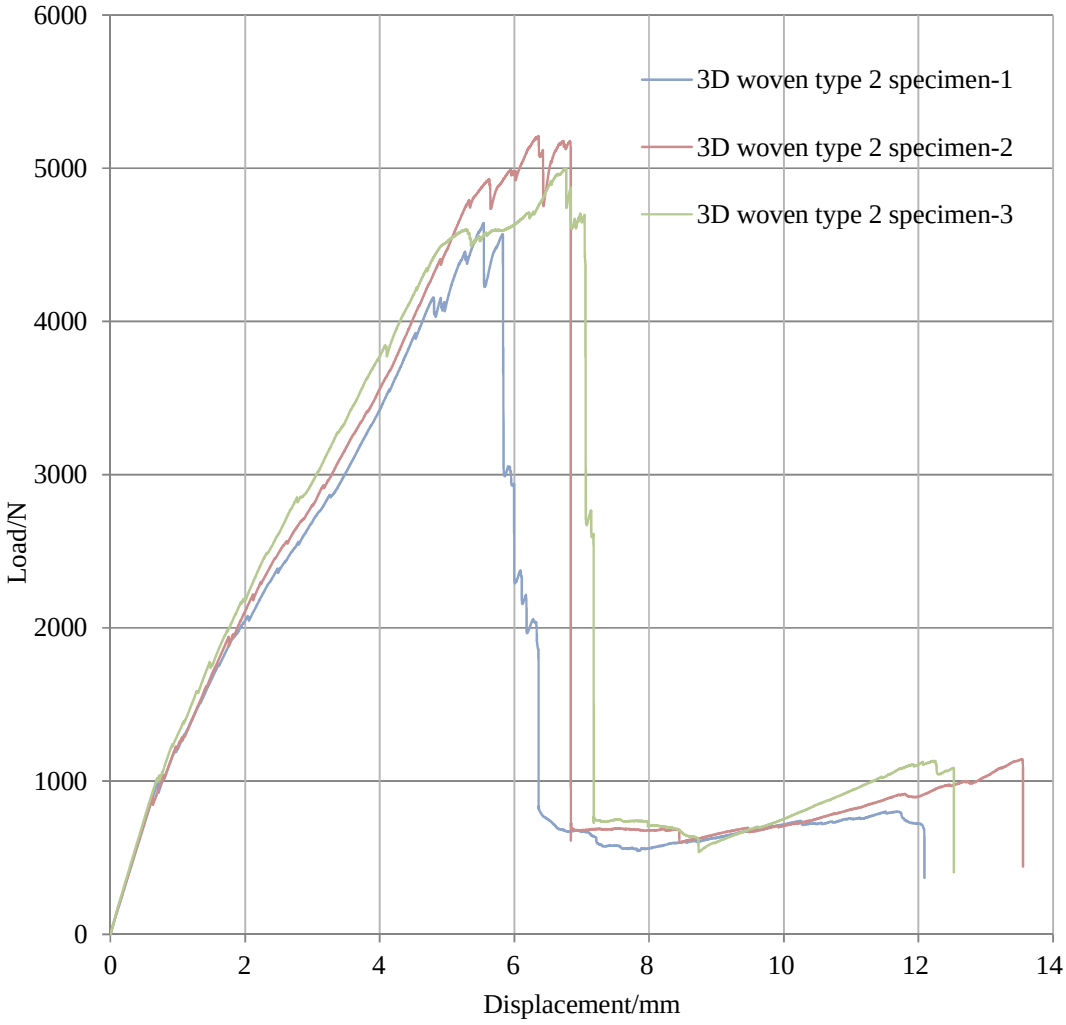
Results of 2D woven specimens:



Results of 3D woven type 1 specimens:



Results of 3D woven type 2 specimens:



Appendix C. Formulation for estimating the minimum interface stiffness in laminates

Turon et al. [75] proposed a closed-form expression for estimating the interface stiffness for a cohesive surface element under mode I delamination. As shown in Figure C-1, both the elastic properties of the sublaminates and the cohesive surface collectively determine the effective properties of the whole laminate. According to the equilibrium condition,

$$\sigma = E_3 \varepsilon = k\Delta \tag{C-1}$$

where σ is the traction at the interface, t is the thickness of a sub-laminate, ε is the strain in the through-the-thickness direction, k is the interface stiffness, Δ is the separation and E_3 is the Young's modulus in the through-the-thickness direction.

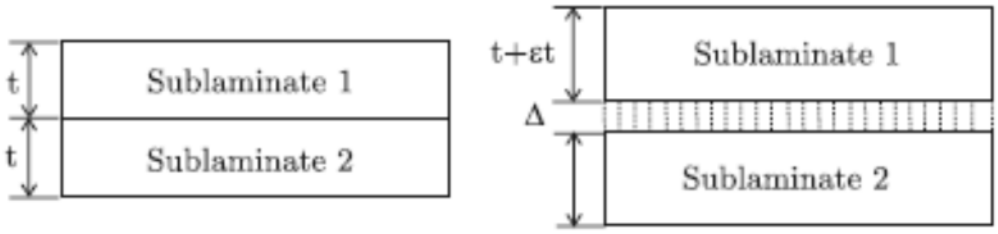


Figure C-1 Effects of the cohesive surface on deformation [75]

The effective strain of the whole laminate is

$$\varepsilon_{eff} = \frac{2\varepsilon t + \Delta}{2t} = \varepsilon + \frac{\Delta}{2t} \tag{C-2}$$

NB: the original authors [75] mistakenly used Δ/t instead of $\Delta/2t$ in the effective strain.

Since $\sigma = E_{eff}\varepsilon_{eff}$, the effective modulus of the whole laminate can be obtained as:

$$E_{eff} = E_3\left(\frac{1}{1+E_3/k2t}\right) \tag{C-3}$$

The effective modulus will not be affected by the interface if $E_3 \ll kt$, i.e.,

$$k = \frac{AE_3}{2t} \tag{C-4}$$

where A is a parameter much greater than 1. NB: the original authors [75] mistakenly used t instead of $2t$ in the above equations.

Appendix D. Generation of geometric models in TexGen

The following Python script is an illustration for implementing the proposed methodology for modelling of bent yarn cross-section shape (Section 3.4.2) in TexGen:

```
from TexGen.Core import *
from math import *

# Create a bent warp yarn
textile = CTextile()

# Spacing between weft yarns
sx = 3.35
yarn = CYarn()

#add nodes for the yarn
yarn.AddNode(CNode(XYZ(0, 0, 0)))
yarn.AddNode(CNode(XYZ(weftyarnwidth/2, 0, 0)))
yarn.AddNode(CNode(XYZ(sx/2, 0, 0)))
yarn.AddNode(CNode(XYZ(sx-weftyarnwidth/2, 0, 0)))
yarn.AddNode(CNode(XYZ(sx+weftyarnwidth/2, 0, 0)))
yarn.AddNode(CNode(XYZ(3*sx/2, 0, 0)))
yarn.AddNode(CNode(XYZ(2*sx-weftyarnwidth/2, 0, 0)))
yarn.AddNode(CNode(XYZ(2*sx, 0, 0)))

yarn.AssignInterpolation(CInterpolationLinear(0))
yarnsection = CYarnSectionInterpNode(1, 0,1)
section1=CSectionRotated(CSectionPowerEllipse(warpyarnwidth,
warpyarnheight, 1), 0.29)
section = CSectionRotated(CSectionPowerEllipse(warpyarnwidthc,
warpyarnwidthc, 1), 0.29)
```

```
yarnsection.AddSection(section)
yarnsection.AddSection(section)
yarnsection.AddSection(section1)
yarnsection.AddSection(section)
yarnsection.AddSection(section)
yarnsection.AddSection(section1)
yarnsection.AddSection(section)
yarnsection.AddSection(section)
yarn.AssignSection(yarnsection)

# Set up yarn position information
PositionInfo = YARN_POSITION_INFORMATION()
PositionInfo.iSection = 0
PositionInfo.dSectionPosition = 0;

SectionLengths = yarn.GetYarnSectionLengths()
for Length in SectionLengths:
    PositionInfo.SectionLengths.append(Length)

YarnSection2 = CYarnSectionInterpNode()
YarnSection2 = yarn.GetYarnSection()

# Position info is set to get the section at node 0
Points = YarnSection2.GetSection( PositionInfo, 40 )

# Following loop changes the points according to Eq.(3.7)
i = 0
for Point in Points:
    Points[i].y = radiusweft[3]*(1-math.cos(Point.x/radiusweft[3]))+ Point.y
    Points[i].x = radiusweft[3]*math.sin(Point.x/radiusweft[3])
    i += 1
# Create a polygon section using the adjusted points
section = CSectionPolygon(Points)

# Get the section at node 1
PositionInfo.iSection = 2
```

```
Points = YarnSection2.GetSection( PositionInfo, 40 )

# Following loop changes the points according to Eq.(3.7)
i = 0
for Point in Points:
    Points[i].y = radiusweft[3]*(1-math.cos(Point.x/radiusweft[3]))+ Point.y
    Points[i].x = radiusweft[3]*math.sin(Point.x/radiusweft[3])
    i += 1

# Create a polygon section using the adjusted points
section1 = CSectionPolygon(Points)

yarnsection = CYarnSectionInterpNode(1, 0,1)
yarnsection.AddSection(section)
yarnsection.AddSection(section)
yarnsection.AddSection(section1)
yarnsection.AddSection(section)
yarnsection.AddSection(section)
yarnsection.AddSection(section1)
yarnsection.AddSection(section)
yarnsection.AddSection(section)
yarn.AssignSection(yarnsection)
yarn.SetResolution(20)

# Add the yarn to our textile
textile.AddYarn(yarn)
```

The method used to extract geometric parameters (yarn path, cross-section dimension) at the junction of the 3D woven type 2 model, through sectioning of the preform, is illustrated below:

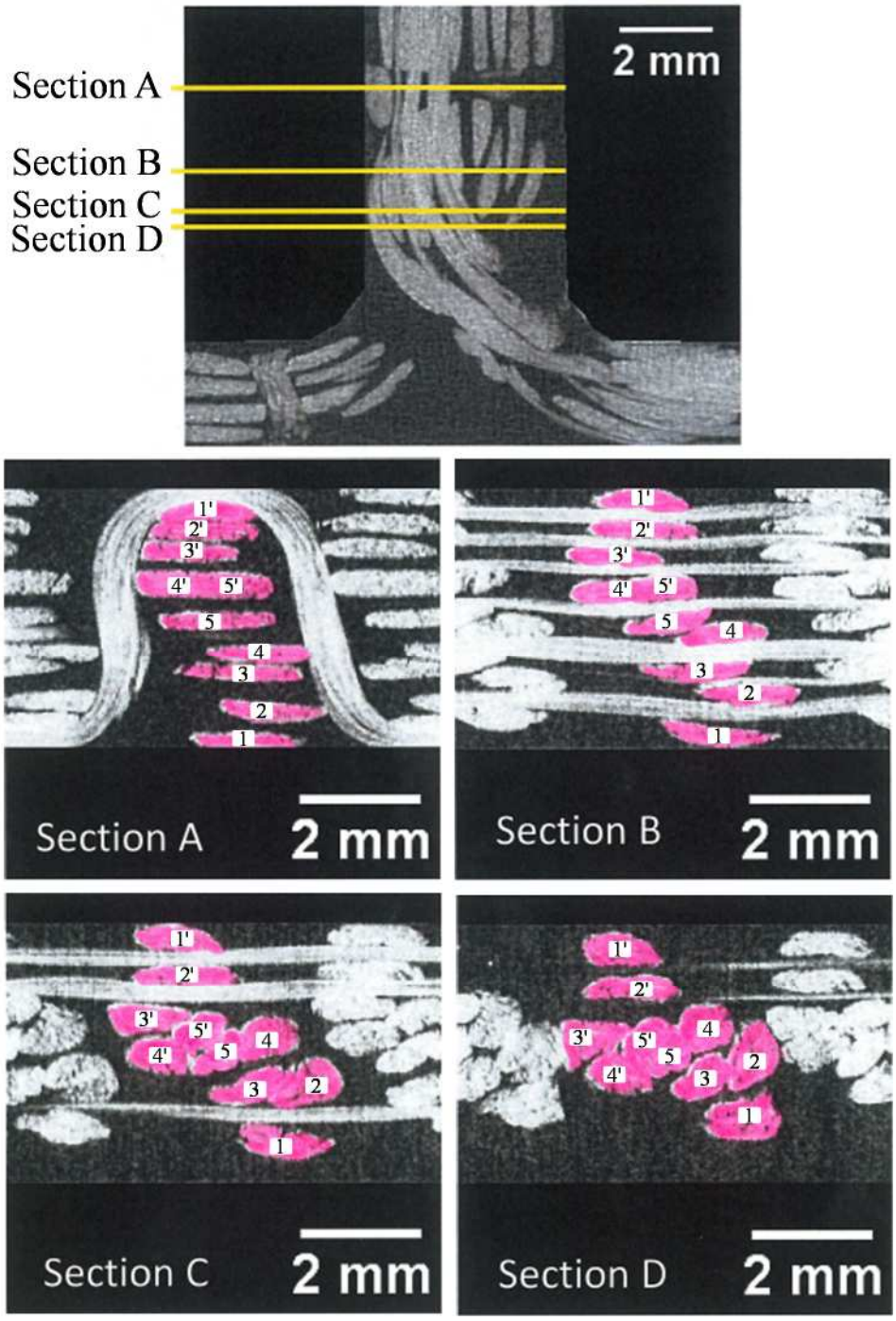
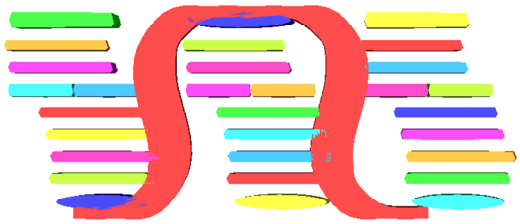
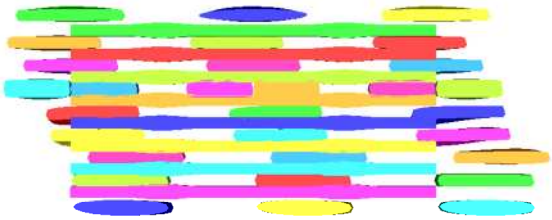


Figure D-1 Sectioning of 3D woven type 2 T-joint preform to extract geometric parameters

At each section of the preform, the locations of centres of yarn cross-sections, along with widths and heights of the yarn cross-sections were measured and then defined in the TexGen model using a Python script. It should be noted that the more sections it uses, the more accurate the TexGen model is but it would lead to a more complex script for the model.



Section A



Section B



Section C

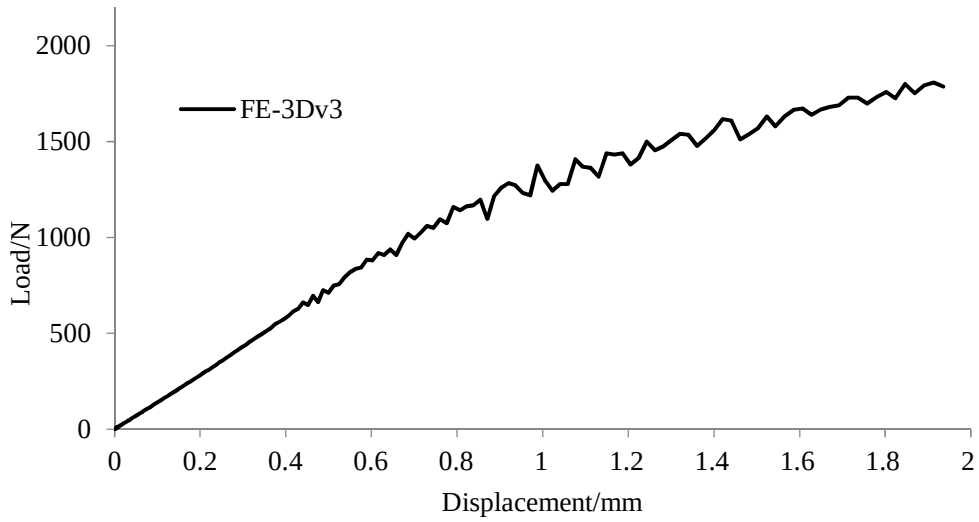


Section D

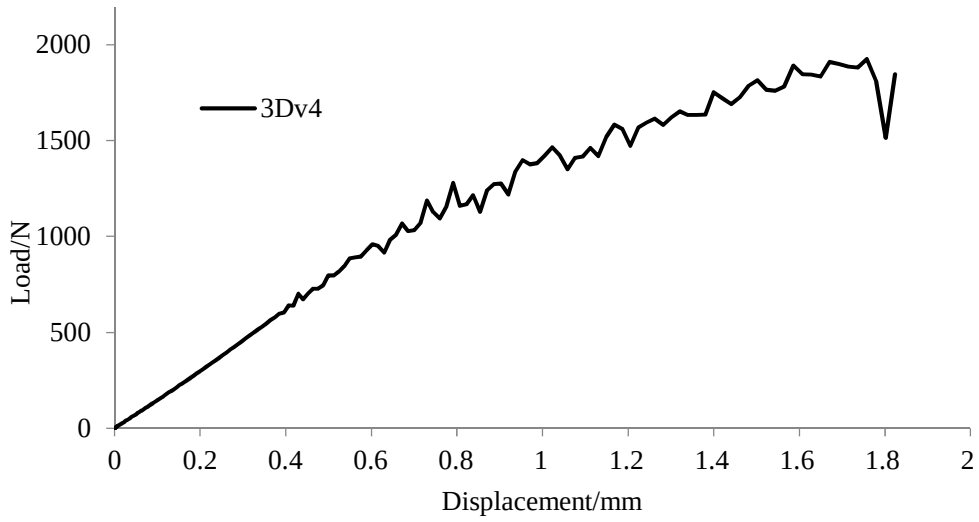
Figure D-2 Sectioning of 3D woven type 2 T-joint TexGen model in comparison with Figure D-1

Appendix E. Load-displacement responses for 3D woven T-joints based on newly designed weave patterns

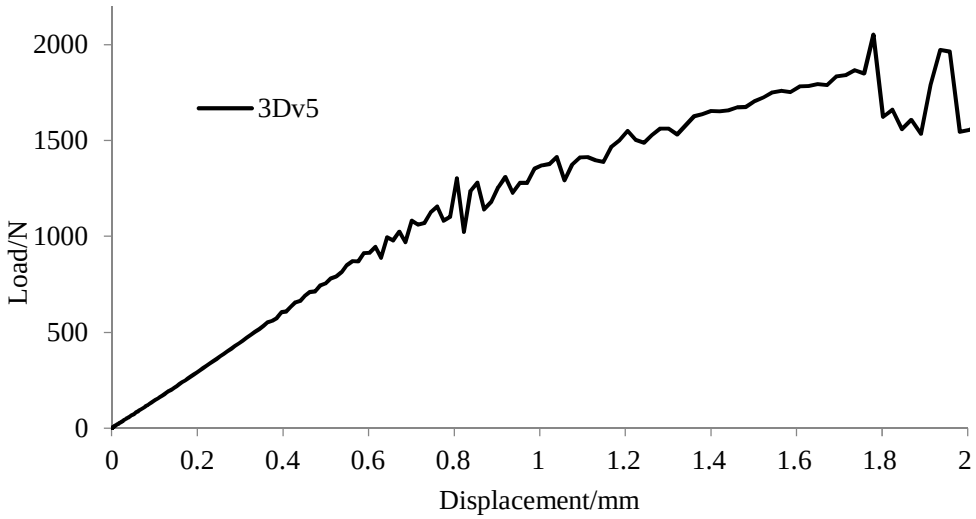
Load-displacement response for 3Dv3 model:



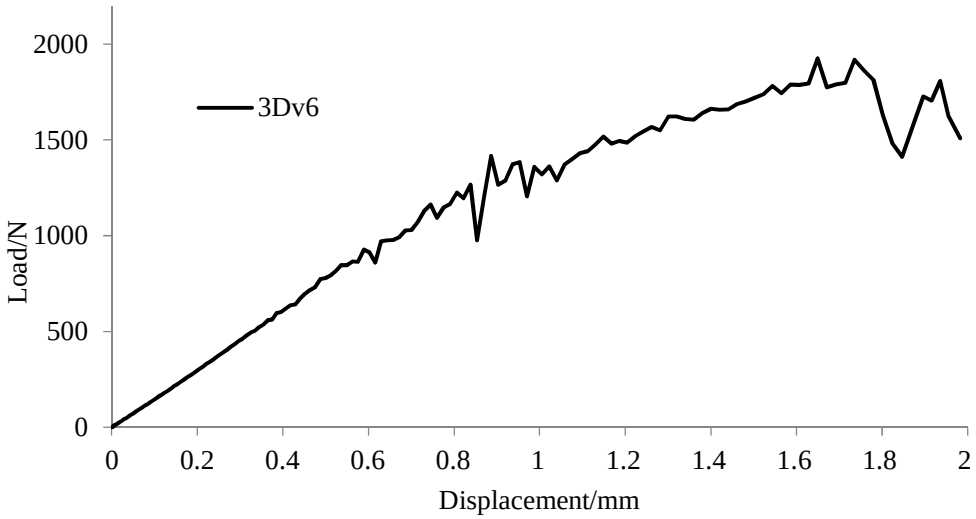
Load-displacement response for 3Dv4 model:



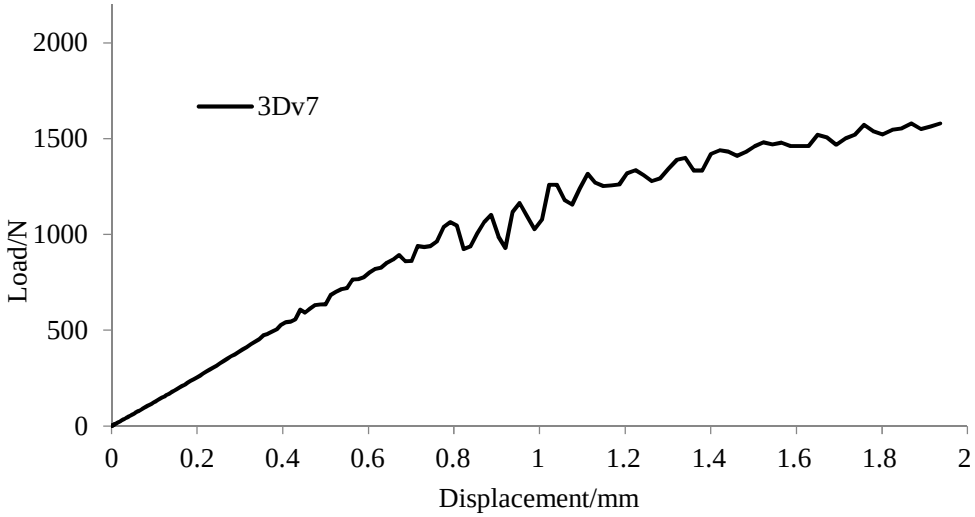
Load-displacement response for 3Dv5 model:



Load-displacement response for 3Dv6 model:



Load-displacement response for 3Dv7 model:



Load-displacement response for 3Dv8 model:

